Department of Precision and Microsystems Engineering

Bottom-up manufacturing of nanocrystalline diamond micro structures and components

Floyd Versluis

Report no : 2020.010
Coach : J.G. Buijnsters
Professor : J.G. Buijnsters
Specialisation : Micro and Nano Engineering (MNE)
Type of report : Thesis
Date : 11 February 2020

Challenge the future

Bottom-up manufacturing of nanocrystalline diamond micro structures and components

Floyd Versluis

Technische Universiteit Delft

50µm

Challenge the future

Bottom-up manufacturing of nanocrystalline diamond micro structures and components

by

Floyd Versluis

in partial fulfillment of the requirements for the degree of

Master of Science
in Mechanical Engineering

at the Delft University of Technology,
to be defended publicly on Tuesday February 11, 2020 at 3:30 PM.

Supervisor:	Dr. J. G. Buijnsters	
Thesis committee:	Prof. dr. U. Staufer,	TU Delft
	Dr. J. G. Buijnsters,	TU Delft
	Dr. R. A. Norte,	TU Delft

This thesis is confidential and cannot be made public until February 11, 2022.

An electronic version of this thesis is available at http://repository.tudelft.nl/.

Preface

For their help and training during experimental work I want to acknowledge A. Sartori, M. Mehrali, M. Ghatkesar, D. Fan and the technical support staff. Furthermore, I want to thank U. Staufer and R. Norte for being part of the committee at my defence. In particular, thanks to my supervisor Ivan Buijnsters for his enthusiastic support and critical feedback throughout the project.

Special thanks to my family and my girlfriend.

Floyd Versluis
Delft, January 2020

Contents

1 Introduction **1**

2 Writing nanodiamond ink through hollow AFM-cantilevers **3**
2.1 Introduction . . . 3
2.2 Experimental . . . 3
2.2.1 AFM-based setup . . . 3
2.2.2 Ink formulation . . . 4
2.2.3 Liquid writing . . . 5
2.2.4 Diamond growth and etching . . . 5
2.2.5 Characterisation . . . 5
2.3 Results and Discussion . . . 5
2.3.1 Wettability . . . 5
2.3.2 Manufacture of diamond dumbbell shaped micropatterns . . . 7
2.3.3 Structure suspension and frequency response . . . 8
2.4 Conclusion . . . 11

3 Maskless lithographic patterning of nanocrystalline diamond **13**
3.1 Introduction . . . 13
3.2 Experimental . . . 13
3.2.1 Stencil patterning . . . 13
3.2.2 Pattern transfer procedure . . . 14
3.2.3 Diamond growth and etching . . . 15
3.2.4 Characterization . . . 15
3.3 Results and Discussion . . . 16
3.3.1 Stencil writing . . . 16
3.3.2 Seeding . . . 16
3.3.3 Diamond patterns . . . 17
3.3.4 Stress analysis . . . 20
3.4 Conclusion . . . 22

4 Conclusion **23**

5 Outlook **25**

A Nanodiamond ink preparation **27**

B Contact angle measurements **29**

C Regrowth of written patterns **31**

D Suspended resonator structures **33**

E Laser Doppler vibrometry **37**

F Analytic work-out frequency formula **45**

G Maskless lithographic diamond patterns **47**
G.1 3D model and printing . . . 47
G.2 Developed photoresist patterns . . . 48
G.3 Nanodiamond seeding . . . 49
G.4 CVD grown NCD patterns . . . 50
G.5 Suspended diamond structures . . . 53

H Bending of diamond patterns **55**

I Buckling of diamond patterns **57**

J Protocol for maskless patterning of nanocrystalline diamond **61**

Bibliography **63**

1
Introduction

The exceptional properties of bulk diamond like high stiffness (Young's modulus $E \sim 1100$ GPa), high thermal conductivity ($k \sim 2000$ W/m·K), wide optical transparency, chemical inertness and biocompatibility make it the material of choice in many high-end applications [1–3]. Especially on the small scale diamond shows its true potential with examples ranging from compact biosensors [4] and localized drug delivery units (surface functionalisation and biocompatibility) to electromagnetic waveguides [5, 6] and high frequency mechanical resonators [7]. Apart from resonators, also its application in heat sinks or smooth, low wear moving parts make diamond a favourable material in the field of micro- and nano electro mechanical systems (MEMS and NEMS) [8].

The diamond used in most MEMS applications is polycrystalline and grown as thin film material by chemical vapour deposition (CVD). In the process, crystallites grow atom by atom from diamond nanoparticle seeds distributed on a (silicon) substrate until they coalesce and form a continuous polycrystalline layer. High seeding densities cause films to close rapidly and reduce the attainable layer thickness. The tuneable size of the individual diamond grains, and consequently the density of grain boundaries containing non-diamond sp^2 carbon, determines the proportion of bulk material properties that is preserved [9]. Based on their respective grain size four types of CVD diamond are distinguished; single crystalline diamond (SCD), microcrystalline diamond (MCD), nanocrystalline diamond (NCD) and ultrananocrystalline diamond (UNCD). Especially NCD films, with an average grain size below 100 nm, are gaining interest in this MEMS/NEMS field due their low friction coefficient and remarkable patterning capability.

Manufacturing functional diamond MEMS requires either top-down or bottom-up patterning. Most present-day diamond micro-devices are fabricated by costly and time-consuming top-down methods, such as focussed ion beam (FIB) milling [10] or reactive ion etching (RIE) [11, 12]. Hence, cheaper bottom-up methods that incorporate selective seeding before chemical vapour deposition are of interest. Some examples of bottom-up methods for selective area deposition of nanodiamond seeds are inkjet printing [13, 14], micro-contact printing [15], dispensing nanodiamond colloidal suspensions from microfluidic systems [16, 17] and methods involving polymers [18] or photoresists (either laden with seeds or as template) [19, 20]. A more comprehensive review of the scientific literature on diamond growth by CVD and the patterning of diamond is given elsewhere [21]. In this work, two novel methods for patterning are added to this list, namely hollow AFM cantilever dispension (microfluidic system) and selective seeding based on maskless lithography (photoresist based method).

The former method is worked out in detail in **Chapter 2** and displays all intermediate steps taken to create doubly-clamped diamond resonators. Various diamond micro resonators have been shaped to reach high frequencies before [22–24], most of them patterned using top-down methods. This work, however, explores the convenience of using bottom-up fabrication in resonator applications. It demonstrates the synthesis of nanocrystalline diamond doubly-clamped resonator structures that are patterned by precise liquid dosing of nanodiamond dispersions (NDD) through a hollow AFM cantilever. To enhance printability, reduce clogging and improve the writing conditions for individual droplets and lines, the fluidic properties of the aqueous NDD and the hydrophobicity of the substrate were system-

atically investigated and optimised. NCD dumbbell shapes were grown by hot-filament CVD and suspended by reactive ion etching of the silicon substrate. The resulting doubly-clamped resonator beams were piezo-electrically actuated and analysed by laser Doppler interferometry to retrieve resonance frequencies and visualizations of the corresponding modes. Finite element analysis on digitally replicated structures converged to similar mode shapes with resonance frequencies close to the measured values.

Optimal resonator performance requires cantilevers to be flat when no load is applied. Advanced stress engineering through delicate adjustments to the growth parameters has shown to minimize the residual stresses that cause bending or buckling [25]. Stress engineering can also be used to manipulate residual stress with deterministic bending as a result. This forms the basis of a rapidly developing research field that explores the use of bending and compressive buckling to assemble 3D architectures from patterned membranes, much like origami or kirigami at the micro- and nanoscale [26–29]. Numerous designs, ranging from simple spirals and toroids to complex pyramidal and scaffold structures, have been realized in a wide variety of materials (e.g. device-grade silicon, gold, polymers and metallic bilayers). Like the 3D structures found in nature (e.g. vascular networks, cytoskeletons) new functionalities become accessible with potential applications emergent in many research fields including photonics, electronics, MEMS, biomedicine and many more. Patterning diamond in 3D could have a huge impact, yet, so far no 3D fabrication technique is compatible with the harsh conditions of diamond CVD growth. As a start, diamond could be stress engineered to bend or buckle out of plane, similar to the method described above. The amount of research performed in this direction is limited, presumably only small deflections are expected due to the extreme hardness of diamond. Nevertheless, Tian et al. showed that ultrathin ($\sim$ 40 nm) NCD films bend severely and form rolled-up structures [30].

Reduced rigidity in thin diamond films is exploited in the work presented in **Chapter 3**. This chapter expands on the novel method for diamond patterning by selective seeding using maskless lithography. It illustrates how 2D and 2.5D nanocrystalline diamond structures with feature sizes down to the single digit micrometer range were produced. Maskless multiphoton lithography was used to create stencils for selective seeding of silicon substrates. Specific NCD pattern designs were CVD grown and suspended by RIE. Residual stresses caused out-of-plane deformation and were further analysed experimentally. An analytical model was used to translate the obtained deflections to stress, which was then compared to the values found in literature.

Chapter 4 summarises the most important findings in both projects and critically reflects on the steps taken towards them. The outlook, **Chapter 5**, addresses tactics for improvement of the currently used methods and poses several ideas for future work. This involves growing diamond on (complex) 3D printed structures and patterning conductive boron doped diamond (BDD) for active MEMS applications.

2

Writing nanodiamond ink through hollow AFM-cantilevers

2.1. Introduction

Using nanodiamond containing dispersions (NDD) for high density seeding of silicon substrates has become one the most effective nucleation methods for CVD growth of thin polycrystalline diamond films. Most of the seed distribution methods completely cover substrates and, for further use, require films to be patterned by top-down methods afterwards. Growing the diamond patterns directly from seeds that are selectively deposited from evaporating nanodiamond dispersion is an efficient alternative. Various microfluidic systems demonstrated localized deposition of ND-fluid, yet no AFM system equipped with a fluidic hollow cantilever has been utilised before. Its high level of precision and ability to dispense small quantities of liquid makes it an excellent method for micro-scale diamond patterning.
This work describes the AFM system used, the composition of the nanodiamond ink and the procedure for writing droplets and lines. Well separated dumbbell shaped patterns were created and characterised by Raman spectroscopy and optical profilometry. Finally the structures are suspended by reactive ion etching and analysed on their frequency response laser Doppler vibrometry.

2.2. Experimental

2.2.1. AFM-based setup

The platform used for hollow AFM-cantilever fluid dispensing is based on a TT-AFM system (*AFM Workshop*). Added features are a pressure controlled fluidic system (-0.8 – 5 bar) and two motorised linear stages that replace the customary manual X-Y substrate alignment. A detailed version of this setup is presented elsewhere [31]. Used components and connections are schematically shown in Figure 2.1a. The measurement system (i.e. laser and detector) and a submicron X-Y-Z piezo positioning stage are omitted in this work. A 3D printed microfluidic interface, depicted in Figure 2.1b, ensures the connection between the macrofluidic system (pressure controlled reservoir) and the microfluidic system (hollow cantilever chip). Fluid enters the fluidic interface via tubing inserted in the channel on the side, indicated with the orange arrow. From here it is directed to a reservoir. A microfluidic silicon-based hollow cantilever chip, fabricated using standard lithographic methods, is placed directly over this reservoir. A narrow duct, not shown in Figure 2.1b, allows flow from the fluidic interface towards an on-chip reservoir that is linked to the channel to the freestanding cantilever. At the far end of this 250 µm long hollow cantilever (height 5 µm, width 40 µm) a hollow pyramidal tip (height 7 µm) is present with edges of 10 µm at its base. Focussed ion beam milling was used to open up the pyramidal tip (see Figure 2.1 c and d), creating orifices with diameters of 2 µm, 1 µm and 0.5 µm, respectively. The opened cantilevers are placed in an environment of evaporating trichloro(dodecyl)silane to cover their exterior with a hydrophobic monolayer to reduce tip wetting [32].

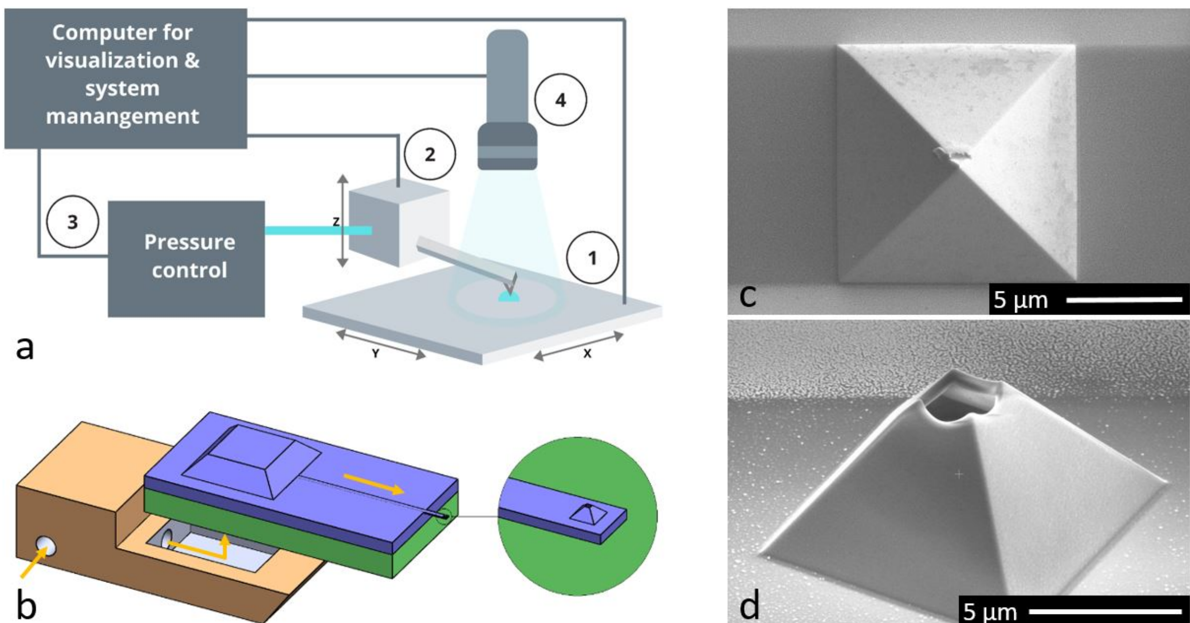

Figure 2.1: a) Schematic representation of the AFM-based fluid dispensing system showing the translation in X-Y plane (1), the uncoupled motorised z-stage carrying the microfluidic AFM- cantilever chip (2) and the external pressure controlled fluid reservoir (3). A high resolution video microscope (4) captures the cantilever and dispensed droplets. A computer manages all four subsystems with corresponding software. b) Models of the 3D printed fluidic interface (bottom) and the microfluidic chip (top) that contains the hollow cantilever presented in the zoom-in. The arrows indicate fluid flow throughout the system. SEM images show the pyramidal hollow cantilever tip before (c) and after (d) focussed ion beam milling an 2 µm orifice.

2.2.2. Ink formulation

Depositing diamond seeds by means of evaporating diamond nanoparticle containing liquids is a well-known seeding method. For initial experiments, an aqueous nanodiamond (ND) ink was prepared analogous to the work reported by Stehlik et al [33]. Now, a commercial 50 mg/mL nanodiamond dispersion (i.e. *NanoAmando*) was diluted with deionised water (DW) to 2.5 mg/mL and subsequentially ultrasonicated for 15 minutes (Appendix A). The small size (∼4 nm) and reciprocal electrostatic repulsion (i.e. positive zeta-potential) of the hydrogen terminated particles both contribute to the stability of this colloidal dispersion. Printing this aqueous ink, however, caused the hollow cantilevers to clog rapidly which led to insufficient seeding for (long) continuous lines. To enhance printability and reduce clogging, the fluidic properties of the aqueous NDD are optimised by adding ethylene glycol (EG). Ethylene glycol is fully miscible with water and introduces viscosity to the colloid as pure EG is more viscous than water at 293 K, see Table 2.1 [34]. Furthermore, it decreases the surface tension, which facilitates droplet formation. The lower vapour pressure of EG hampers evaporation and gives nanodiamond particles time to distribute and settle on the substrate. Experiments showed controlled droplet formation and sporadic clogging for a ratio of 40:60 (DW:EG). Uniform continuous lines were drawn as will be expanded on in section 2.3.1. Fluidic properties of the liquid are obtained by interpolation of present data sets and given in Table 2.1.

Table 2.1: Properties of water, ethylene glycol and a water-EG mixture (40:60) at 293 K determined by measurement (i.e. density) and interpolation (i.e. viscosity and surface tension [34]).

Properties @ 293 K	Density [g/cm^3]	Viscosity [mPa·s]	Surface tension [mN/m]
Water	0.98	1.00	72.58
Ethylene Glycol	1.11	20.81	49.15
Water-EG (40%-60%)	1.08	7.88	54.05

2.2.3. Liquid writing

A cleaved silicon sample (1 x 1 cm^2) is placed on the sample holder and moved in position by the motorised X-Y stage. The motorised z-stage carrying the microfluidic chip (inverted w.r.t. Figure 2.1b) is lowered stepwise until fringes appear on the cantilever. This indicates bending and hence contact. From this position, the stage is moved up until the fringes disappear. Pressure is then applied and a liquid droplet grows until it touches the substrate and forms a stable meniscus. Dots of dispensed liquid are created on the silicon sample by repetitively cutting the pressure and moving up the stage until surface tension fails to stabilise the meniscus. Lines of dispensed liquid are drawn by keeping the cantilever at a constant height above the surface and moving the substrate underneath. Dumbbell shaped patterns with varying core beam lengths in the range 600 to 1000 µm were designed to demonstrate the applicability of this method in bottom-up synthesis of diamond micro resonator structures. These structures were created by writing the core beams and dispensing big droplets on both endpoints afterwards.

2.2.4. Diamond growth and etching

Seeded silicon substrates were subjected to a CVD diamond growth process in a home-built HFCVD reactor. A substrate temperature of 725°C and gas composition of 2% CH_4 in a surplus of H_2 (total gas flow of 306 sccm) at 10 mbar resulted in the growth of a thin NCD layer on the patterned areas. Diamond structures were suspended by isotropic reactive ion etching for 9 minutes in an *Adixen AMS-100* setup (operating power: 2000 W, SF_6 gasflow: 500 sccm, pressure: 100 µbar, stage temperature: −10 °C).

2.2.5. Characterisation

Material characterisation Wettability of the substrate surface is determined with a *Theta Lite Optical Tensiometer*. It measures the static contact angles of DI-water and diiodomethane on acid-treated and gradient silicon substrates. Based on this data, built-in *OneAttension* software determined surface free energy of the substrate according to OWRK/Fowkes theorem. High magnification images of the diamond structures were created with a *Jeol JSM-6010LA* scanning electron microscope, operating at electron acceleration voltages of 5–20 keV. A *Horiba LabRAM HR* setup (Argon ion laser 514 nm, spectral resolution ∼0.3 cm^{-1}) was used to characterise the grown diamond material using Raman spectroscopy in backscattering mode. White light interferometry measurements, performed with a *Bruker Contour GT-K* 3D optical microscope (20-100x magnification, VXI mode), gave topographic information (i.e. height and roughness) of the grown structures. The 3D-data was analysed using *Gwyddion Version 2.53* software.

Mechanical characterisation and modelling A *Polytec MSA-400-PM2-D* Laser Doppler Vibrometer was used for identification of the frequency response of the suspended NCD microstructures. A home-built piezo-electric actuator setup, operating in air, was fed with pseudo-random noise (0.5 V) to excite all frequencies in the range of 1 to 2000 kHz. Interferometry measurements on the Doppler shift were used to establish a frequency spectrum that is divided in 102400 FFT-lines. Corresponding software was used to analyse and visualise vibrations as 3D animations. The 3D modelling software *SolidWorks 2018-2019* was used for the digital replication of the NCD suspended beam structures and silicon supports. The SolidWorks add-in frequency simulation, based on finite element methods (high quality meshing), gave the resonance frequencies and mode shapes.

2.3. Results and Discussion

2.3.1. Wettability

Preliminary tests of writing on bare silicon wafer were unsuccessful as the substrate surface proved too hydrophobic and showed the necessity for surface treatment. The naturally hydrophilic siliceous surface is covered with a variety of functional groups that give rise to a slightly hydrophobic character. Although it was possible to place droplets, no lines could be drawn as the meniscus was dragged along without leaving a fluid trail.

To increase wettability, described in terms of surface free energy γ [mN/m], samples were hydroxylated with an acid treatment. Samples were cleaned in a boiling mixture of HCl (38%), H_2SO_4 (95%), and HNO_3 (70%) (1:1:1 volume ratio) and rinsed in deionised water afterwards. Acid treatment replaces the

functional groups for –OH (hydroxyl) groups which interact with water by means of hydrogen bonding. A surface energy of 64.0 [mN/m] was found for the acid treated samples. Contact angles of 34° and 55° were determined for DI-water and diiodomethane, respectively (Appendix B.1).
This hydrophilic character induces substantial spreading of droplets and lines, which contrasts the aim of narrowing down linewidth. Therefore, samples with gradient wettability, ranging from hydrophobic to hydrophilic, were created to find the optimal surface free energy for writing. These gradient samples were created by placing a rolled-up cloth, soaked with trichloro(dodecyl)silane, parallel to an acid treated sample inside a closed petri dish (Appendix B.2). Upon evaporation, hydroxyl groups make place for hydrophobic silane groups with inverse correlation as function of lateral distance from the silane cloth. Contact angle measurements showed that for an exposure of 7 minutes gradients in surface energy appear ranging from 18.1 to 29.9 [mN/m] (Appendix B.1). Figure 2.2a shows diamond patterns obtained after 1 hour of CVD growth from droplets on an acid treated substrate (1) and on various locations on a substrate with gradient surface energy (2-5). The peripheral particles in 3-5 are probably the result of nanodiamond seeds that attached to the surface prior to contact line retraction as the cantilever is pulled from the droplet. Lines drawn on gradient substrates are depicted in Figure 2.2c and show a diminishing line quality of writing towards the hydrophobic regime. The line is very uniform in width (~60 μm) in the hydrophilic region, but becomes less continuous when moving towards the more hydrophobic domain.

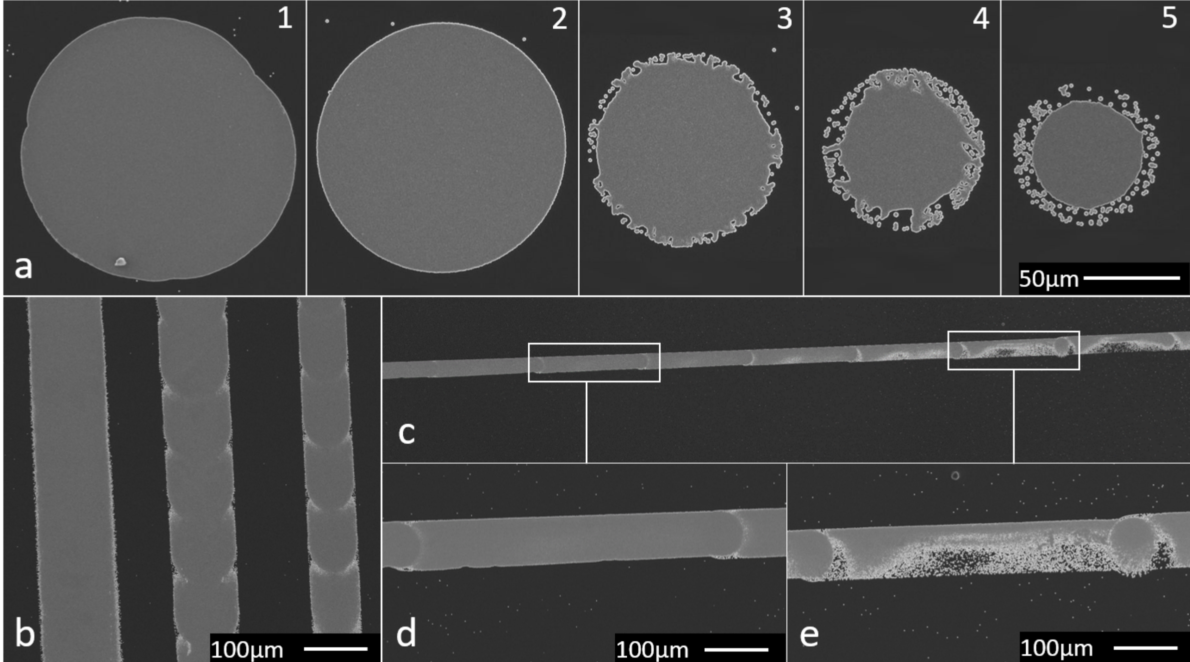

Figure 2.2: a) SEM images of CVD diamond micropatterns grown from droplets written on a hydrophilic substrate (1) and substrate with gradient wettability (2-5), where the gradient goes from hydrophilic (CA 80° for DI water) in 2 to hydrophobic (CA 107° for DI water) in 5. b) Vertical lines written perpendicular to the gradient in wettability range comparable to zoom-in d. c) Diamond line parallel to the gradient (hydrophilic to hydrophobic from left to right). Zoom-ins d) and e) show the line quality in corresponding wettability regime.

The lines in Figure 2.2b show a narrowing down in width towards more hydrophobic surface regions. Unfortunately, no lines could be drawn closer to the hydrophobic silanised region for reasons similar to those noted for bare silicon. This means a threshold exists resulting in a minimal line width. This could mean that the gradient is really a gradient for the μL droplets used in CA measurements, but the femto/pico liter droplets dispensed by the hollow AFM cantilever meet/feel local patches of hydrophobic silanes and hydrophilic hydroxyls causing discontinuity of line writing. Although the regions of reduced hydrophobicity, as in Figure 2.2a-2 , showed highest quality of writing, later experiments were performed on acid treated substrates. This due to the fact that a specific hydrophobicity is hard to prepare and maintain reproducibly.

2.3.2. Manufacture of diamond dumbbell shaped micropatterns

With the intention of creating functional structures, dumbbell shaped patterns were written and subsequently processed by CVD to function as full-diamond micro-resonators after suspension by RIE. Dumbbell shapes arise from drawing lines and dispensing big droplets on both the endpoints. Three rows each containing 5 dumbbells of, respectively, 600 μm, 800 μm and 1000 μm long lines were printed. Big droplets were created by applying a constant pressure of 1 bar for an extended period of time. As the droplet volume increased, the liquid contact line shifted outward abruptly in random direction creating the bulgy shapes in a stepwise manner, shown in Figure 2.3a. This is similar to what is observed in contact angle hysteresis measurements and depends on the chemical and topographical heterogeneity of the substrate [35]. As the volume of a droplet with pinned line of contact increases, the contact angle increases. When this contact angle surpasses the dynamic advancing contact angle, new area is wetted to balance the acting forces again.

Profilometry measurements on the CVD grown structures showed smooth continuous lines of 60 μm in width having a uniform layer thickness of ∼650 nm. A layer thickness of ∼500 nm was found for the central parts of the endpoints, peripheral areas (wetted later) showed discontinuities and declined in height (Appendix C). Reduced seeding density as a result of the coffee stain effect is the presumed cause. Figure C.3 shows the height profile of the endpoint after the first CVD cycle and validates the presumption. This difference in seeding density faded as the sample was regrown to a thickness of 1 μm for stability reasons after etching.

Raman spectroscopy was used to determine the quality of the nanocrystalline diamond film material shown in Figure 2.3a. The well-known diamond peak (1332 cm^{-1}), highlighted in the single point spectrum of Figure 2.3b, is scanned over a raster of data points placed over the same beams depicted in Figure 2.3c. The intensity (green) mapping, Figure 2.3d, indicates the presence of diamond and shows close overlap with the SEM image.

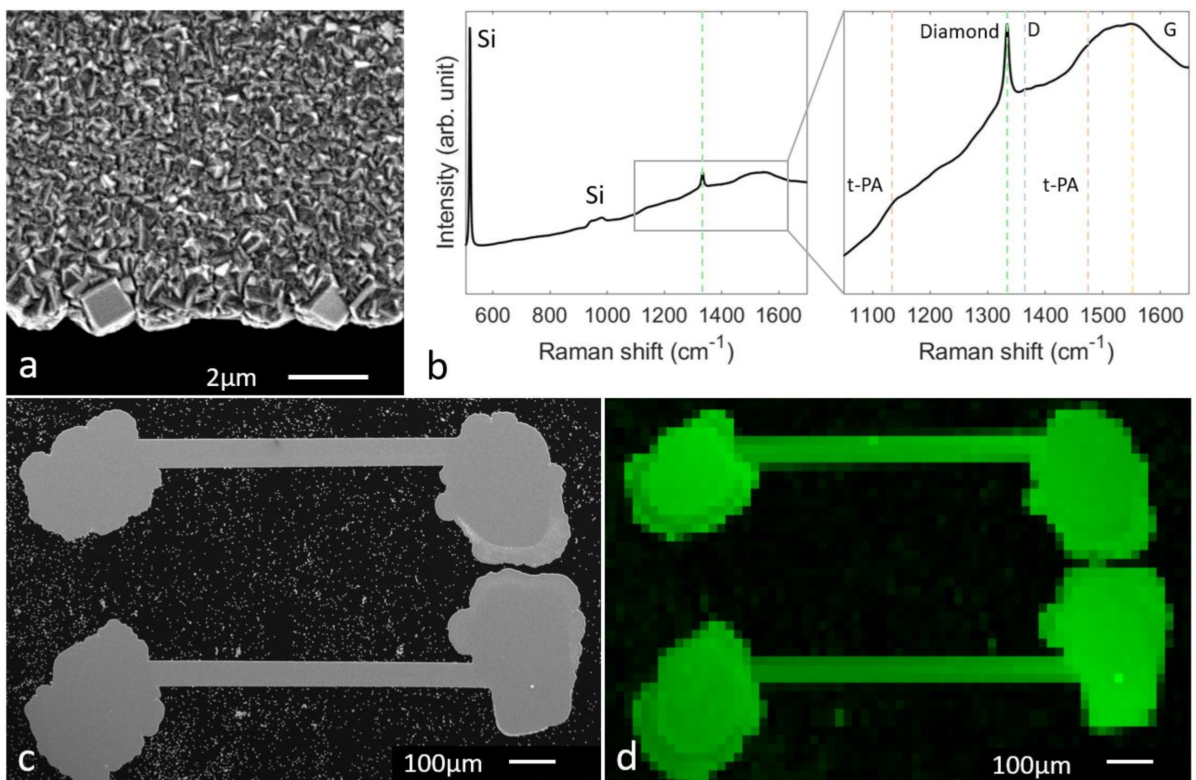

Figure 2.3: a) SEM image depicting the grains of the NCD film. The lack of competition at the edge allows crystallites to grow bigger. b) Single point Raman spectrum depicting silicon peaks, the diamond peak (green) and the standard locations of sp^2 related peaks; G-band (yellow), D-band (blue) and t-PA peaks (orange). c) SEM image of two 1000 μm long diamond dumbbell shapes of 1 μm thickness. d) Raman intensity mapping of the same two dumbbells indicating the diamond containing areas.

Besides the diamond peak, the single point spectrum shows silicon peaks around 520 and 940-980 cm^{-1} both originating from the substrate. The big bulge between 1500-1600 cm^{-1} is presumably a combination of the transpolyacetylene peak (t-PA) at 1480 cm^{-1} and the C-band (centered around 1555 cm^{-1}). This C-band is indicative for the presence of sp^2 bonded carbon, known to be predominantly present on grain boundaries in NCD [36]. Along with the aforementioned t-PA peak a complementary second t-PA peak is found around 1150 cm^{-1}, here present as slight bulge [37]. The D-band, normally present around 1380 cm^{-1}, is not observed in this spectrum.

2.3.3. Structure suspension and frequency response

Reactive ion etching with a sulphur hexafluoride (SF_6) plasma eroded the silicon substrate underneath the diamond patterns (Appendix D). Nine minutes of isotropic etching lead to an etch depth of ~100 µm and fully suspended the diamond beams. The bulgy endpoints were underetched in lateral direction to a depth of ~60 µm. The areas of bright contrast in Figure 2.4a show the areas of contact between the NCD film and the silicon stems. Figure 2.4b shows the thin (1 µm) suspended diamond film with the smooth nucleation side exposed on the bottom half of the image. The nanogranular microstructure and surface facets of the NCD material is apparent. In Figure 2.4c, the suspended NCD beam is shown to remain virtually straight despite its high aspect ratio of about 1:800.

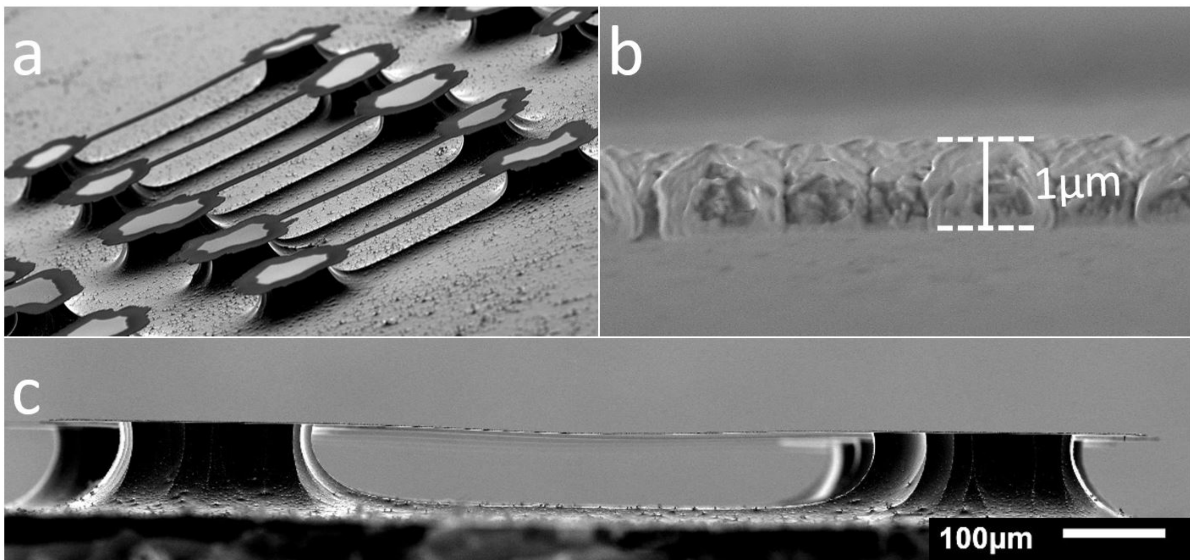

Figure 2.4: a) SEM image depicting a row of medium-sized (800 µm) suspended beam structures. Brighter structure areas indicate connection to the silicon supports. b) SEM image of the suspended diamond thin-film beam accentuation the thickness of 1 µm. The bottom half of the image shows the nucleation side of the film. c) Side view SEM image showing the high aspect ratio (1:800) between length and thickness of the suspended NCD beam.

The suspended structures, now shaped as simple doubly-clamped resonators, are analysed on their resonating properties. Laser Doppler vibrometry was used to determine the frequency response to piezo-electric actuation in air. Single point data showing the frequency spectra in the range 1 to 2000 kHz are presented in Appendix E.

Measured spectra diverged from the anticipated spectra of having few well-defined resonance peaks corresponding to the torsional and sinusoidal flexural modes predicted from Bernoulli-Euler beam theory. Instead, many 'extra' peaks arose which complicated the analysis and demanded visualisation of the vibrations at any frequency. *PVD Software* was used to construct 3D animations of the vibrating structures from rasters of datapoints, see Figure 2.5a. These animations were used to link resonance peaks to 'clean' modes. Higher order torsional modes and flexural modes up to the 7th order could be distinguished. In the higher frequency regime circular modes were observed in the overhanging NCD film around the silicon supports. The 'extra' peaks originated either from superpositions of resonance modes or noise from external vibrations (e.g. air, system). Some modes however, were not observed at all. This includes the fundamental mode.

Measured resonance frequencies are compared to FEM frequency simulations. For modelling purposes only flexural modes (2nd, 3rd, 4th and 5th) were investigated as the irregular shapes of the bulgy endpoints are hard to model and have a more prominent effect on torsional and circular modes. From each dumbbell group, i.e. with small (600 µm), medium (800 µm) and large (1000 µm) total beam lengths, one structure was selected for FEM analysis. Smallest free beam lengths (i.e. beam lengths between the inner endpoints of the dumbbell shapes) were measured from the corresponding SEM images as depicted in Figure 2.5b. The small, medium and large lengths measure up to 375 µm, 472 µm and 617 µm, respectively.

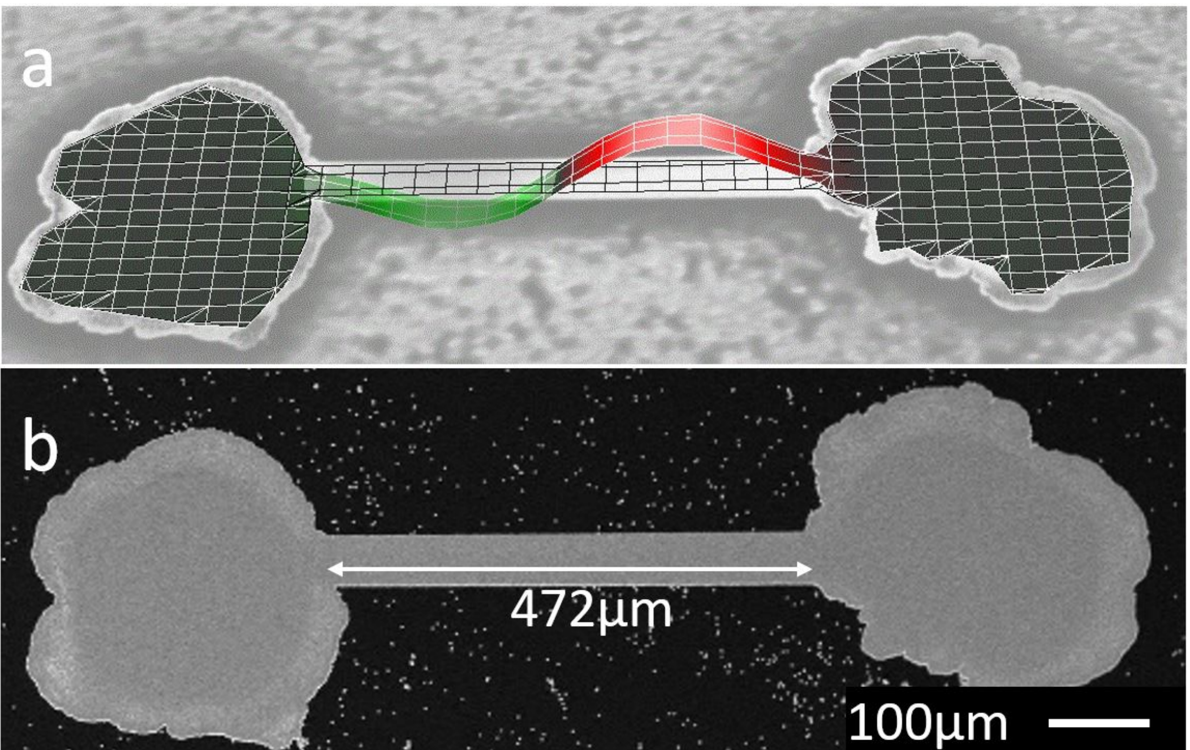

Figure 2.5: a) 3D animation of a medium-length beam vibrating in 2nd resonance mode created by *PVD Software* combining single point measurement data of all data points in the raster. b) Measurement method to determine shortest free beam length from the corresponding SEM image.

Resonator structures were modelled using the built-in material properties of silicon for the supporting pillars. A custom material was assigned to the nanocrystalline diamond part, see Table 2.2. NCD material properties (density ρ, Young's modulus E) were adopted from the work by Sartori et al.[13], as identical growth parameters were used.

Table 2.2: Material properties of NCD and silicon used in the finite element simulation.

	Nanocrystalline diamond	Silicon
Young's modulus E [GPa]	600	112
Density ρ [kg/m^3]	3310	2330
Poisson ratio	0.07	0.28

In the model, the irregular shaped endpoints were simplified as circles. The silicon pillars were drafted from the bottom up ending up 60 µm inwards from the edge of the diamond circles. During the simulation the bottom of both silicon pillars was set anchored. A high meshing resolution was used to find the resonance frequencies presented in Table 2.3. The values are compared to the measured resonance frequencies and provided with the respective error given in percentages. For completeness, also the quality factors of the measured peaks are provided. Like classical mechanical theory states, frequencies increase for decreasing beam length. Resonance frequencies for the shortest and longest beams reach

from 193 kHz and 79 kHz for the 2nd mode respectively, to 999 kHz and 428 kHz for the 5th mode. In terms of resonance frequencies the medium sized beam lies in between, with its 2nd resonance mode at 139 kHz, its 3rd at 330 kHz and its 5th at 734 kHz. The errors, most within 10%, indicate reasonable agreement between measurement and simulation. Deviations result from simplifications in the FEM model.These were necessary as accurate replication of such asymmetrical shapes in close detail is impossible. Assumed material properties deviating from the actual (but unknown) properties may have also contributed to the error.

Table 2.3: Flexural mode shapes created in FEM simulation are depicted in the first column. The other columns (2-6) show values of FEM frequencies, measured frequencies, respective errors, Q-factor and Young's moduli for resonating beams with free beam lengths of 375 µm (S), 472 µm (M), and 617 µm (L), respectively.

Mode shape	FEM freq. [Hz]	Meas. freq. [Hz]	Error [%]	Q-factor	Stiffness E* [GPa]
	S: 79857 M: 56580 L: 32682	S: - M: - L: -	- - -	S: - M: - L: -	- - -
	S: 214810 M: 153850 L: 88684	S: 193243 M: 139082 L: 79648	11.16 9.04 11.34	S: 169.7 M: 160.2 L: 60.5	321 389 379
	S: 410290 M: 297910 L:171590	S: - M: 330391 L: -	- 10.90 -	S: - M: 309.0 L: -	- 512 -
	S: 668770 M: 487970 L: 280470	S: 684336 M: - L: 319063	2.32 - 13.76	S: 237.0 M: - L: 265.1	383 - 579
	S: 978820 M: 718660 L: 414940	S: 999512 M: 733713 L: 428222	2.11 2.09 3.20	S: 214.3 M: 36.7 L: 66.7	366 462 467

To validate the used Young's modulus Euler-Bernoulli beam theory is consulted. It gives an analytic approach to finding resonance frequencies of (doubly-clamped) homogenous cantilever beams. Various steps, worked out in Appendix F, result in the following formula:

$$f_n = \frac{1}{2\pi}\frac{{\beta_n}^2}{L^2}\sqrt{\frac{EI}{\rho}} \tag{2.1}$$

This formula gives the resonance frequencies as a function of β_n which is a constant that varies with mode n, effective beam length L, Young's modulus E, inertia I and mass density ρ per unit length. With the resonance frequencies, and other variables known, this formula can be rewritten to solve for E. Calculated moduli E^* are presented in the last column of Table 2.3.

The reason that these values come out relatively low compared to the 600 GPa used in FEM analysis is due to the participation of the underetched disk. As described by Gavan et al. [38] this contribution increases the effective length of the beam. Implications of parts of the disk contributing can be observed in Figure 2.5 and the mode shapes in Table 2.3. The areas contributing to the vibration increase with frequency. Addition of an averaged 58 µm, 43 µm, 37 µm to the free lengths of S, M and L, respectively, makes the Young's moduli reach a value of ~600 GPa. These values seem reasonable as the total underetched distance is 120 µm (i.e. 60 µm for each disk) and imply a valid choice of the E-modulus for FEM simulation.

2.4. Conclusion

In this work, a novel method of selective area deposition of nanodiamond seeds is presented using a hollow AFM cantilever based dispension method. Advanced ink formulation, specific substrate modifications and subsequent diamond thin-film growth by HFCVD enabled the bottom-up microfabrication of nanocrystalline diamond structures composed of dots and continuous lines of 1 µm thickness and 60 µm in width. Functionality was added by underetching dumbbell shaped diamond structures to turn them into mechanical micro resonators. Frequency response of doubly-clamped beam resonators was determined with laser Doppler vibrometry and compared to data obtained with FEM simulations. Correspondence between these two methods is shown to be reasonable as deviations, originating from model simplifications, remain below or close to 10%. Although further research is required to reduce linewidth and improve repeatability, this work shows the potential of localised liquid dispensing for bottom-up microfabrication of NCD devices.

3

Maskless lithographic patterning of nanocrystalline diamond

3.1. Introduction

High definition patterning of polycrystalline diamond thin films with (sub)micrometer resolution is currently reserved for top-down manufacturing methods like FIB and RIE. Most bottom-up techniques lack resolution, consistency or flexibility for real competition on this scale. In a pursuit to close this gap, photolithography proves as one of the most promising methods to tackle these shortcomings. This advanced technology proves its functionality as it is extensively used in the semiconductor industry for fabrication of polymeric 2D structures that fulfill masking purposes.
In this work maskless photolithography is used to fabricate photoresist patterns that serve as stencils for selective nanodiamond seeding. A lift-off step removes the photoresist before a CVD process grows a NCD thin film on the seeded areas. The fabrication process is outlined in the first section. This includes a summation of all consecutive fabrication steps, the diamond growth parameters and a description of the method for localised exposure of photoresist. Analysis on the stencils, seeding quality and grown patterns then addresses the limitations of the method. In an attempt to add a third dimension to the 2D diamond structures, residual stress induced bending and buckling is addressed. Specific 2D designs are grown and suspended by reactive ion etching of the silicon substrate. Based on the out-of-plane behaviour a stress evaluation is made and compared to literature.

3.2. Experimental

3.2.1. Stencil patterning

The 2D stencils for selective diamond seeding were created with maskless multiphoton lithography, a specific type of photolithography. Standard (UV) photolithographic processes illuminate photo-sensitive photoresists through pattern-defining photomasks and by this process alter the chemical compositions of the exposed areas. In positive tone resists, altered regions are dissolved and washed away in developer solution, whereas negative tone resists solidify upon exposure.
The technique used in this work avoids the need for expensive photomasks and allows for rapid prototyping as patterns are transferred onto silicon samples by two-photon (de)polymerisation (also known as direct laser writing) of positive tone photoresist. The working principle of two-photon polymerisation (2PP) relies on the nonlinear absorption of pulsed (120 fs) near infrared (NIR) laser light, which has a wavelength (780 nm) the photoresist is normally transparent to. Only in the vicinity of the focal point, intensity is sufficiently high to exceed the polymerisation threshold via two-photon absorption. This small ellipsoidal volume of localized polymerisation, called a voxel, is depicted in red in Figure 3.1. Three dimensional designs are written by scanning this voxel through the photoresist at adequate slicing and hatching distances, ensuring the necessary overlap for full exposure. Exposed patterns undergo chemical alteration which cause them to dissolve in the subsequent development step describe in the next section 3.2.2.

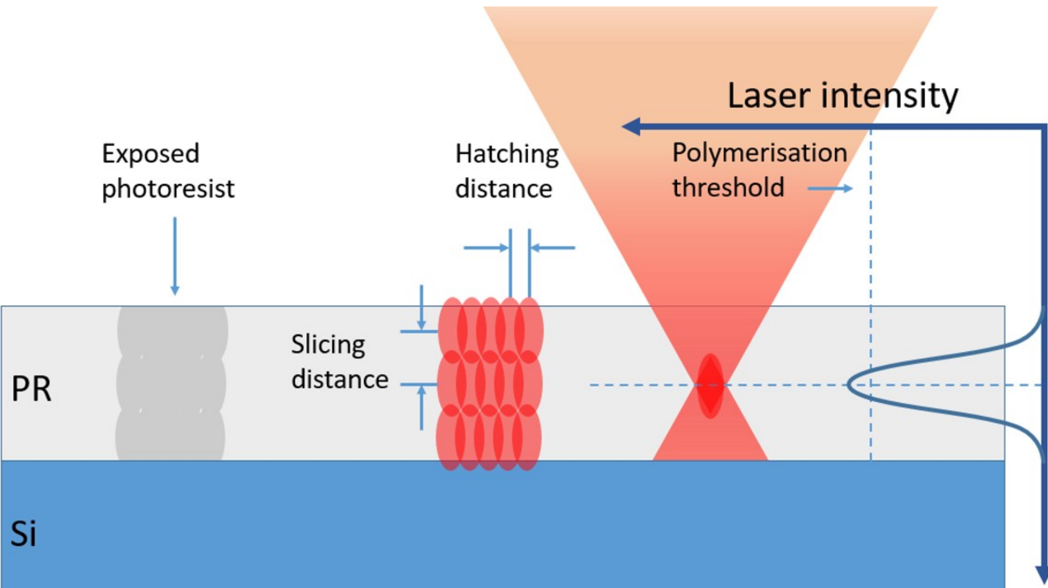

Figure 3.1: Schematic representation of the working principle of two-photon polymerisation in positive tone photoresist (PR) on a silicon (Si) substrate. A converging pulsed laserbeam illuminates the photoresist with NIR light, a wavelength the resist is transparent to. Near the focal point however, laser intensity overcomes the (de)polymerisation threshold by nonlinear absorption and forms a voxel (red). Scanning this small ellipsoidal volume through the resist enables writing three dimensional depolymerised patterns (gray). Contrary to unexposed resist, these chemically altered patterns dissolve in a subsequent bath of developer solution.

3.2.2. Pattern transfer procedure

The developed method used for the bottom-up synthesis of diamond patterns is presented in Figure 3.2. Detailed descriptions of the individual steps are summed up below and in Appendix J.

1. Cleaved silicon samples (2.5 x 2.5 cm^2) are cleaned with acetone, isopropanol, deionized (DI) water (18.2 MΩ·cm) and subsequently blow-dried in a stream of nitrogen gas.

2. The cleaned sample is coated with the viscous positive tone photoresist *AZ4562*, obtained from *MicroChemicals GmbH*. A two-step spincoat process in a *Laurell spincoater (WS-400E-6NPP-LITE)*, operated at 500 rpm for 5 seconds + 2300 rpm for 20 seconds, results in a uniform layer with a thickness of ~10 µm. Immediately after spin coating, samples are placed on a hotplate at 110°C for 5 minutes to evaporate excessive solvent and stabilize the photoresist film. After this softbake process, the sample cools down and is left to rehydrate for at least 5 minutes.

3. Patterns are transferred to the photoresist by means of multi-photon lithography, section 3.2.1, using the x20 air objective of a *NanoScribe Photonic Professional (GT)* operating at a laser power of 80 (in % of 50 mW) and a scan speed of 2000 µm/s. (Appendix G.1)

4. Development in a 1:4 dilution of KOH-based *AZ400K* developer in DI water dissolves the exposed areas at a rate of 2 µm/min. A process of 5-7 minutes, enhanced with delicate magnetic stirring, erodes the full layer and unveils the silicon substrate in the patterned areas. Developed samples are rinsed with DI water and blow-dried to finalize the polymeric stencil. (Appendix G.2)

5. A *NanoAmando* nanodiamond (i.e. hydrogen-terminated) dispersion (50 mg/mL), obtained from the *NanoCarbon Research Institute Co. (Japan)*, is diluted with DI water to a concentration of 2 mg/mL and ultrasonicated for 10 minutes. Then samples are seeded by submersion in this solution for 1 hour. Afterwards, these samples are briefly exposed to developer solution (15 s) to detach possibly adhered nanodiamonds before being extensively rinsed with DI water.

6. To strip the photoresist from the rinsed samples, acetone is sprayed on during 1500 rpm rotation in a *Polos spincoater (spin150i)*. During spinning, acetone is changed for isopropanol to flush away the residue left behind by acetone. Before spin drying, the sample is supplied with a final flush of DI water. (Appendix G.3)

7. A nanocrystalline diamond thin film was grown from the patterned nanodiamond seeds by hot-filament assisted CVD. (Appendix G.4)

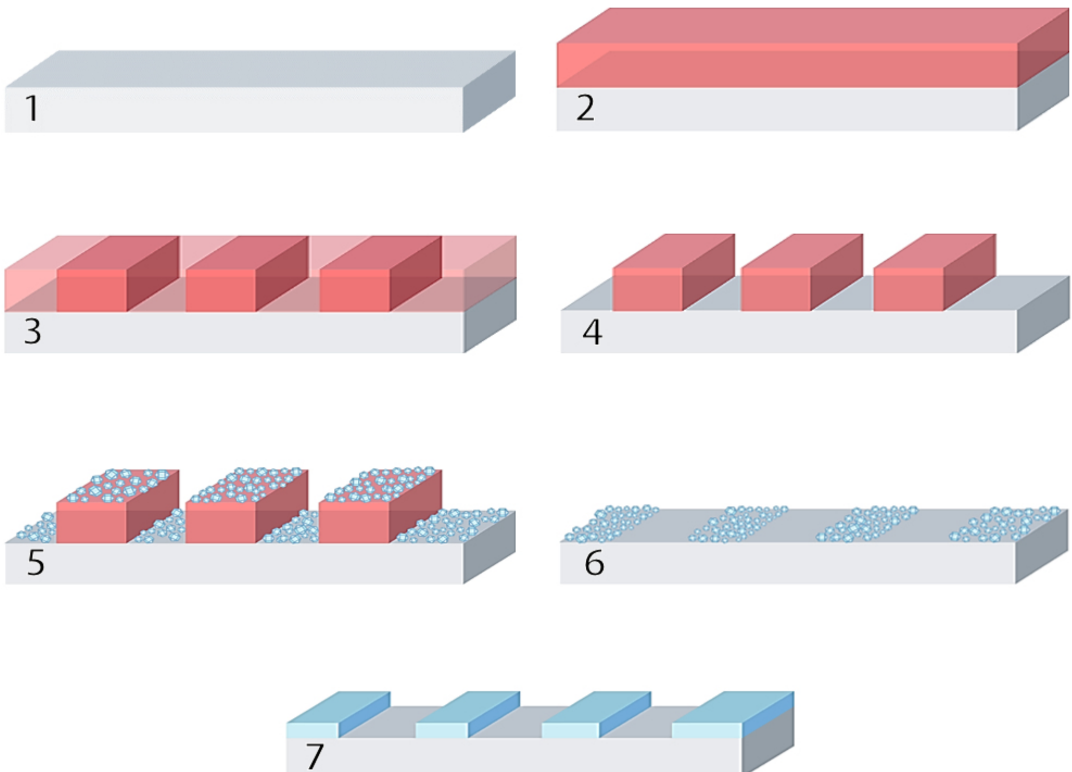

Figure 3.2: Schematic representation of the fabrication steps (1-7) starting from the bare silicon sample, via lithographic patterning to patterned diamond films. In this image the photoresist layer is depicted in red.

3.2.3. Diamond growth and etching

Seeded silicon substrates were subjected to a CVD diamond growth process in a home-built HFCVD reactor equipped with a tantalum filament. Nanocrystalline diamond layers with varying thickness in the range of 150 to 500 nm were grown on the seeded areas at a substrate temperature of 725°C and with a gas composition of 2% CH_4 in a H_2 surplus at 10 mbar. Diamond structures were suspended by 3-4 minutes of isotropic reactive ion etching in an *Adixen AMS-100* setup (operating power: 2000 W, SF_6 gasflow: 500 sccm, pressure: 100 µbar, stage temperature: −10 °C).

3.2.4. Characterization

High magnification images of the diamond thin-film structures were created with a *Jeol JSM-6010LA* scanning electron microscope, operating at electron accelerations of 5–20 keV. Distributed diamond seeds were imaged using a high resolution field-emission *FEI Nova NanoSEM 450* setup operating at 15 keV. A *Horiba LabRAM HR* setup (argon ion laser 514 nm, spectral resolution ~ 0.3 cm^{-1}) was used to characterize the material with Raman spectroscopy. White light interferometry measurements, performed with a *Bruker Contour GT-K 3D* optical microscope (20-100x magnification, VXI mode), gave topographic information (i.e. height and roughness) of the grown structures. The 3D-data were analysed using *Gwyddion* Version 2.53 software.

3.3. Results and Discussion

3.3.1. Stencil writing

With the focus on scaling down the size of bottom-up diamond structures, stencil limits are described in terms of minimal feature size which means smallest area exposing the silicon substrate. This feature size depends both on actual voxel dimensions and to a lesser degree on the development process. Voxel dimensions are affected by laser power and resist-related properties (e.g. index of refraction, reactivity), hence no exact voxel dimensions are known. An array of lines with decreasing linewidth, ranging from 1 to 5 µm, was designed to identify the resolution. NanoScribe software (*DeScribe*) translated the 1 µm line to one individual voxel line, wider lines consist of multiple overlapping voxel lines.

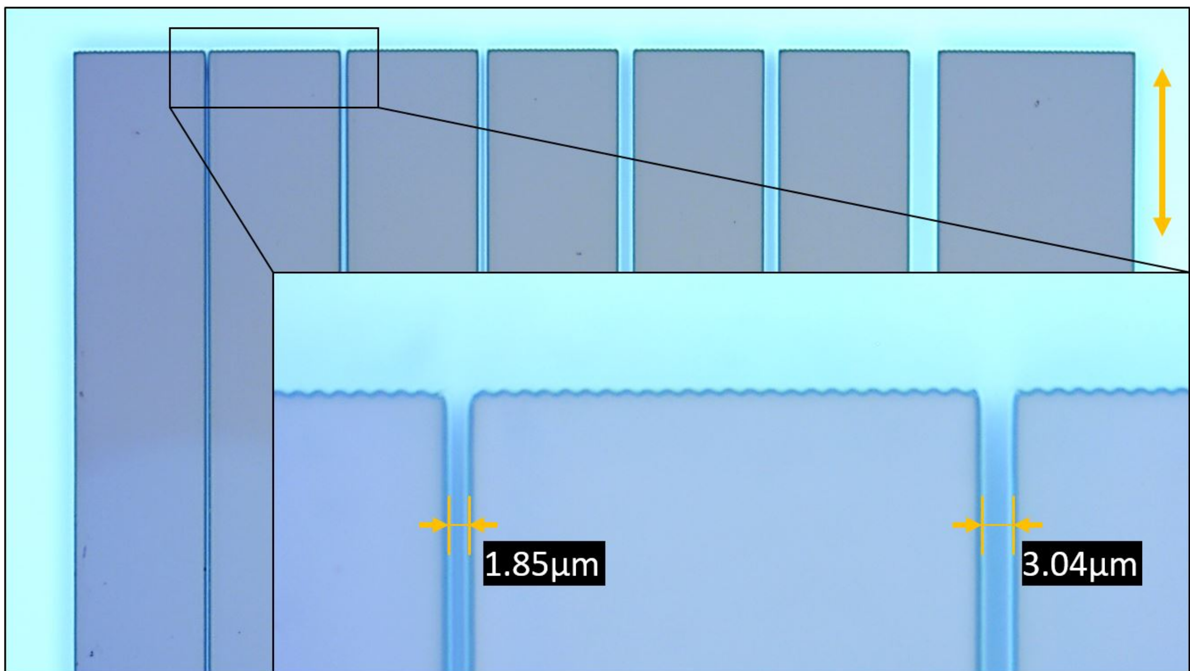

Figure 3.3: Optical image of the photoresist pattern used for limit evaluation. The light contrast areas are exposed silicon wafer, while the dark contrast regions indicate photoresist. The inset shows the rugged edge perpendicular to the writing direction (arrow) and thinnest line width measuring 1.85 µm.

Besides laser power, the development process plays a role in this feature size as well. Etch rate and selectivity vary significantly as AZ photoresists are highly sensitive towards changing environmental conditions like humidity and temperature [39]. Such variations may increase lateral 'erosion' and with that enlarge the area of unveiled silicon. From the inset in Figure 3.3 one can observe a single voxel line of 1.85 µm in width, this represents the minimal feature size a diamond line can be produced from. The 3.04 µm width of the second line can be attributed to two of these voxel lines spaced at a 1 µm hatching distance. To fully expose the 9.8 µm thick photoresist layer with a voxel of ∼6 µm axial length, patterns were printed in stacks of partly overlapping slices.
The inset in Figure 3.3 shows a wiggly horizontal edge on the photoresist. This feature results from voxel lines being drawn in perpendicular direction (here vertical). A higher edge quality can be acquired by triggering the contour function (Appendix G.1), which is used in more complex patterns that will be discussed in section 3.3.3.

3.3.2. Seeding

Patterned samples were seeded by submersion in an aqueous detonation nanodiamond dispersion (NDD). Hydrogen terminated diamond nanoparticles possess positive surface charge and mutually exert electrostatic repulsion which keeps them from agglomerating [40]. This positive zeta-potential and small particle size (∼4 nm) ensures long term stability of the dispersion as Brownian motion dominates sedimentation. The silicon oxide layer present on top of native silicon attracts the NDs electrostatically

due to its negative surface charge [41]. This strong adhesion endures the aforementioned rinsing and spin coating procedures and yields high resolution selective seeding as shown in Figure 3.4 and Appendix G.3. On the substrate surface, nanoparticles electrostatically self-assemble as evenly spaced clusters (<100 nm) instead of individual particles, a phenomenon which Yoshikawa et al.[42] attribute to long range repulsion.
The diamond particles did not adhere to the photoresist and got flushed away during rinsing with DI water. A brief rinse with developer solution removes a thin layer of photoresist due to nonzero selectivity and with that the spare particles that possibly did adhere. Subsequent intensive flushing with DI water removed most of the superfluous particles from the trenches. A final spin coating step with acetone, IPA and DI water was utilized to dissolve the resist.
The high resolution SEM images in Figure 3.4 show the dense and uniform seed coverage on patterned areas. The sharp contrast between seeded and unseeded area indicates the quality of patterning. In comparison with other in-house seeding methods (i.e. inkjet printing [13] and spin seeding [43]) equivalent seeding densities were found, i.e. 10^{10} cm^{-2}. Striations forming as a result of the coffee-stain effect were not observed. Some samples, however, showed small pieces of photoresist residue still being fixed to the substrate. Increasing the volume of acetone used during rinsing solved this problem.

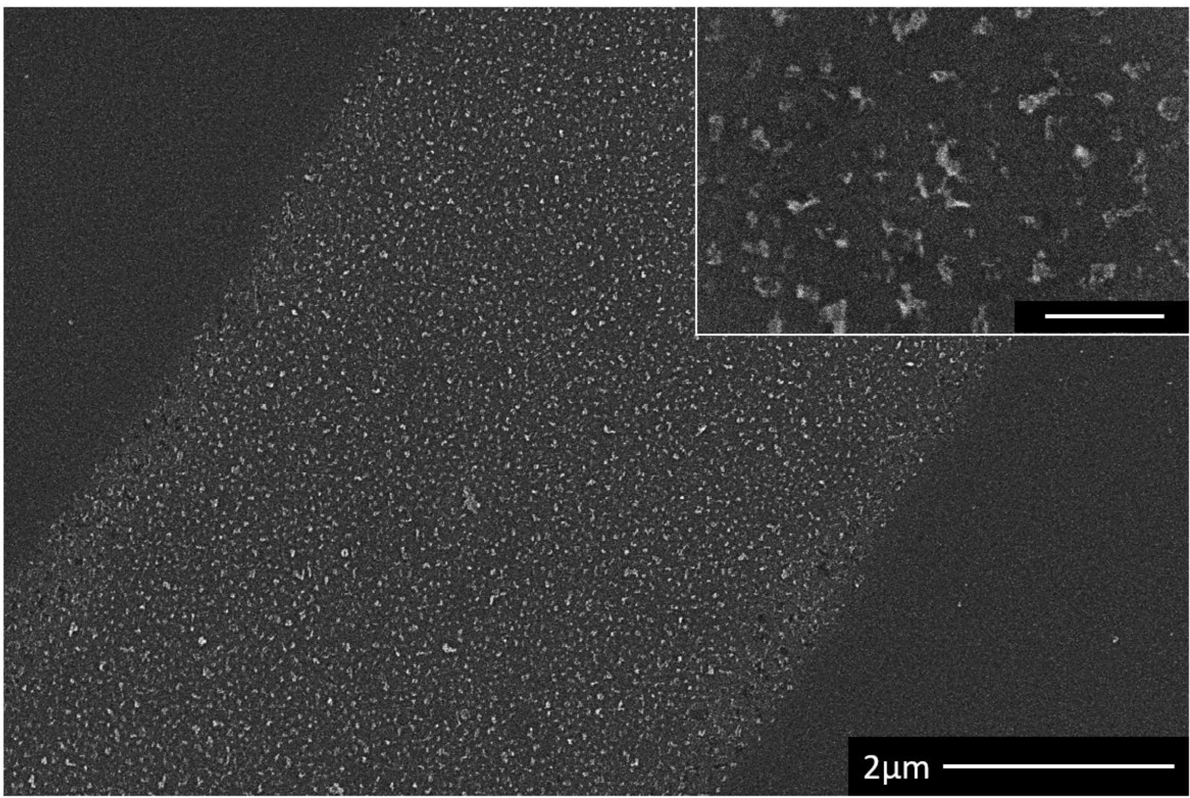

Figure 3.4: HR-SEM image depicting the sharp contrast between seeded and unseeded areas. The inset (scale bar 200 nm) shows a zoom-in of the individual clusters of diamond nanoparticle seeds.

3.3.3. Diamond patterns

Basic patterns Minimal diamond linewidth was determined by seeding the stencil, discussed in section 3.3.1, and subjecting it to HFCVD to grow a nanocrystalline diamond thin film on the patterned areas. Optical microscopy images (see Figure 3.5b) revealed a closed uniform film after 15 minutes of growth using the CVD process parameters mentioned in section 3.2.3. White light interferometry measurements indicated a diamond layer thickness of ~150 nm. For comparison, Figure 3.5c shows an underetched version of the same pattern together with a zoom-in of the narrowest line.
Crystallites grown from stray seeds can be observed close to the diamond lines (Figure 3.5b), this is the result of secondary seeding. Smeared out streaks of diamond particles appearing after CVD

growth indicate a surplus of seeds in the patterned trenches, supposedly stacked at the boundaries between silicon substrate and the steep walls of photoresist. During spin coating with acetone these walls dissolved and the particles were redistributed by the centrifugal force. Nonetheless, due to the brief CVD process most of the stray crystallites are well separated and removed during etching of the substrate (Figure 3.5c). The increased linewidth can be deduced from lateral diamond growth. Growth rate in standard conditions is known to be around 1 μm/h. For 15 minutes of growth this adds ~250 nm on both sides of each line, the measured value of ~2.28 μm (Figure 3.5d) thus closely matching the expected value.

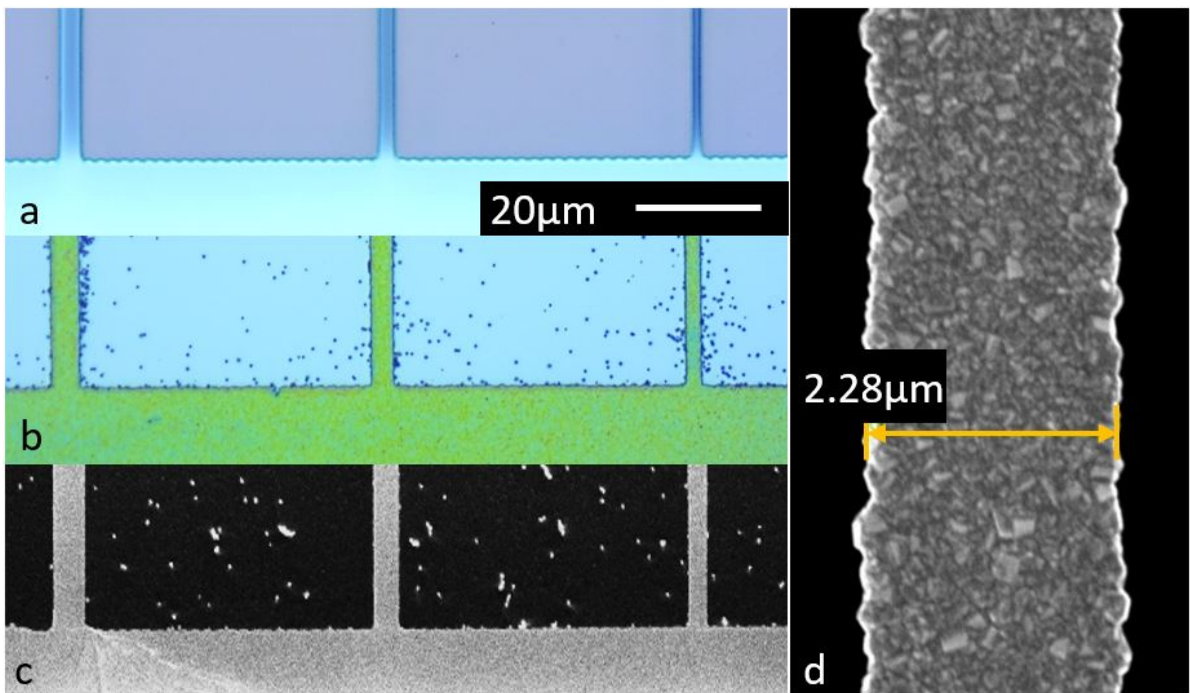

Figure 3.5: a) Optical microscope images of the patterned a) photoresist (pink/purple) and b) diamond (green). c) SEM image of the suspended diamond beams (light contrast), with (d) a zoom-in on the beam of smallest width.

Raman spectroscopy (Figure 3.6) was used to characterise the bonding structure of the film grown under conditions posed in section 3.2.3. The well-known diamond peak, specified by the green dashed line, can be found at 1332 cm^{-1} and indicates the presence of sp^3 bonded carbon. The sharp peak measured at 520 cm^{-1} together with a broader band at 940-980 cm^{-1} both originate from the silicon substrate.

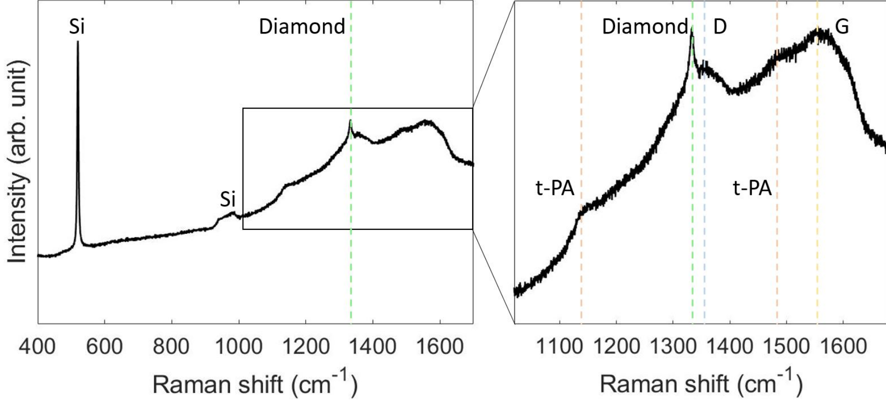

Figure 3.6: Raman spectrum for diamond grown for 15 minutes at the conditions posed in section 3.2.3. The spectrum displays two silicon peaks and highlights the characteristic diamond peak (green). Besides diamond four additional carbon signals are pointed out in the zoom-in; D-band (blue), G-band (yellow) and 2 peaks for transpolyacetylene (orange)

From the zoom-in four additional carbon-related features can be distinguished. Around 1150 cm^{-1} resides the peak for transpolyacetylene (t-PA) which is accompanied by a peak at 1480 cm^{-1}, both indicated by orange dashed lines [37]. Two peaks indicative for sp^2 bonded graphitic material present at the grain boundaries in NCD [36] are the D-band (1360 cm^{-1}) and the G-band (1555 cm^{-1}), indicated by the blue and yellow dashed lines respectively.

Advanced patterns The 2D freedom of maskless lithography provides the opportunity of rapid prototyping any (2D) pattern imaginable, some examples are shown in Appendix G.4. Specific patterns, Figure 3.7a and b, were created in an attempt to approach the ultimate goal of producing out-of-plane diamond thin film microarchitectures. Under influence of residual stresses, similar designs in other materials (e.g. polycrystalline silicon and gold) were shown to bend out-of-plane after etching or FIB [44–46]. This 2.5D approach, using stress engineering, is described in detail in Section 3.3.4.

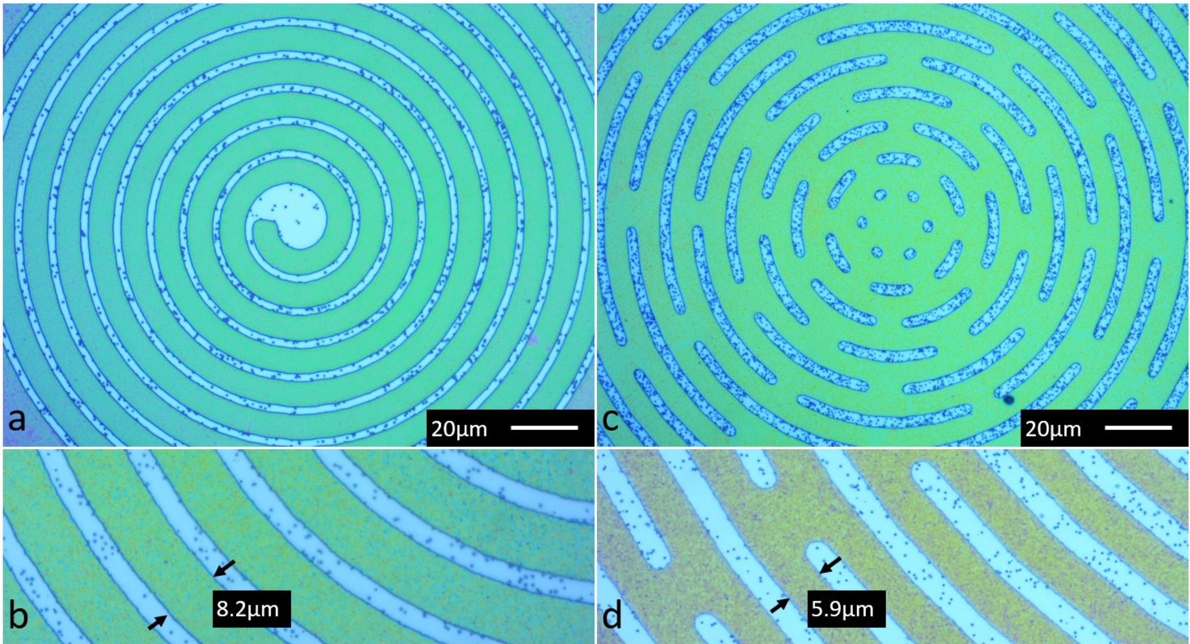

Figure 3.7: Optical microscope images showing patterned NCD films (green/yellow colour): a) spiral and c) flower (kirigami) pattern. Images b) and d) are zoom-ins of identical designs on other samples indicating the width of the NCD lines.

In both patterns shown in Figure 3.7a and b, spiral and flower (kirigami) shape, continuity and uniformity of the NCD film is evident. The green/yellow colour of the diamond sharply contrasts the white/blue colour of the silicon wafer. Unlike the rugged horizontal edges highlighted on the photoresist (see Figure 3.3), these NCD patterns display fluent contours all around. During exposure the contour function in the NanoScribe tool was enabled; this feature draws the outlines of the pattern before the interior is filled with parallel lines. The line widths of the spiral and the flower (kirigami) pattern are 8.2 µm and 5.9 µm, respectively. The photoresist structures that mask the silicon from getting seeded were designed with a certain minimal aspect ratio of ~3 (height to width) to preserve stencil stability, as thinner structures tend to let loose during development or rinsing. Similar to the simple pattern, stray diamond nanoparticles are distributed on these unpatterned regions, although not dense enough to coalesce and disrupt the intended diamond patterns.

3.3.4. Stress analysis

The diamond patterns depicted in Figure 3.7 were suspended by reactive ion etching so that only the thick outer rim remains fixed to the silicon substrate (Appendix G.5). Residual stresses in the diamond film were expected to deform the structures out-of-plane, either by bending or buckling. Each type of deflection respectively generated by intrinsic vertical gradient stress or planar thermal stress.

Gradient stress Upward bending was observed in 1 μm thick NCD cantilevers (1000 μm length) created in previous work. Herein cantilevers were patterned by localized dispension of a nanodiamond dispersion via a hollow AFM cantilever. Subsequent growth and etching steps were analogous to the ones used in this work. Figures of these suspended structures are present in Appendix D.4 and D.5. Based on this result, spiral patterns (3100 μm path length) were grown at various substrate temperatures (625, 675, 725 and 740 °C) to analyse the respective effect on bending. Samples were only briefly grown to a thickness of 150-200 nm to enhance deflection by exploiting the fact that flexural rigidity scales with the cube of film thickness. Unfortunately, all spirals were found bent down so severely that the central part laid flat on the etched substrate as shown in Figure 3.8a and b.

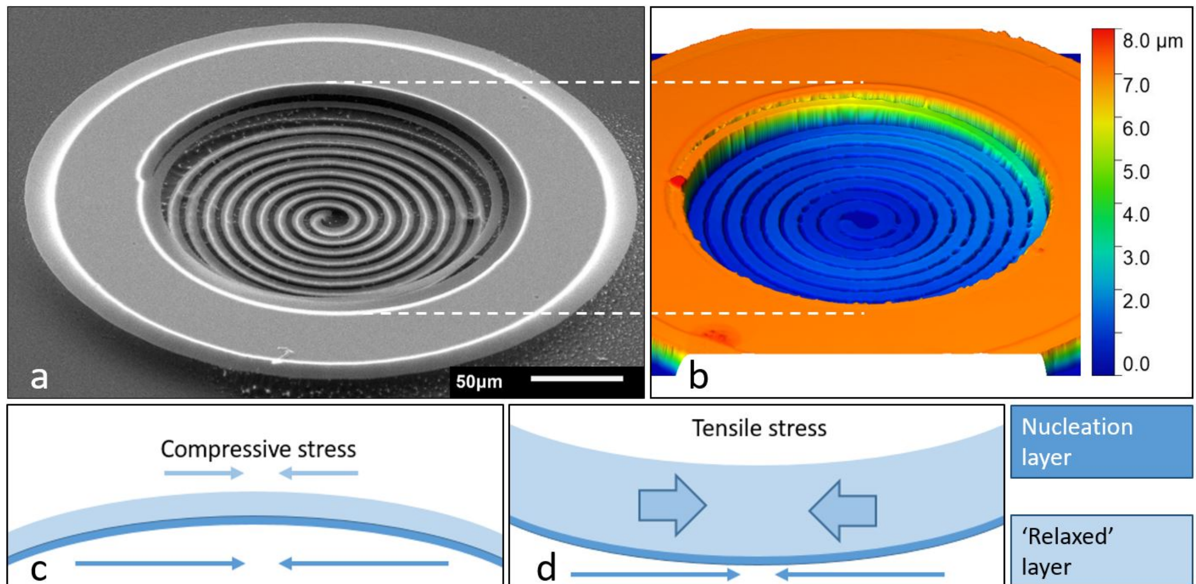

Figure 3.8: a) SEM image of the underetched spiral-shaped pattern. Fixation to the silicon substrate is depicted by the darker ring enclosed by rings of bright contrast. The actual spiral, starting left from the centre, is completely suspended and bends down until it lies flat at the etched substrate. b) Optical profilometry image adding height information to the underetched structure. c) Graphical representation of the presumed stress distribution. In a thin film the tensile nucleation layer exerts compressive stress on the less tensile 'relaxed' layer. By convention such a bi-layered film is defined compressive and causes downward bending. d) In thicker films the thicker 'relaxed' layer overpowers the tensile stress present in the nucleation layer which results in upward bending.

This effect can be attributed to an intrinsic gradient stress that arises during the early stages of diamond growth. As isolated diamond seeds grow, they coalesce and form a closed diamond film. During coalescence, crystallites have the tendency to mutually pull each other in. This results in infinitesimal strains localized in the nucleation zone and manifests as a thin film with built-in tensile stress [47]. This tensile thin film exerts compressive stress on a thicker 'relaxed' layer grown on top. By convention such a double-layered system is labelled compressive overall and causes beams to bend downwards, assigning stress as negative (Figure 3.8c). The upward bending of the aforementioned cantilever implies that this 'relaxed' layer is also slightly tensile and overpowers the thin tensile film at a certain thickness (Figure 3.8d). One proposal for further research thus involves the growth of similar NCD spirals for an increased growth duration. Growing samples for 15, 30, 45 and 60 minutes might show the tipping point from where downward bending turns the spiral into an upward helical structure (Appendix H).

In case the spirals are fully suspended (i.e. not in contact with the silicon substrate due to bending) gradient stress can be determined from the deflection Z' of the central part of the spiral structure by means of the adjusted Stoney equation shown in formula 3.1 [48].

$$\sigma = \frac{1}{3}\frac{E_r}{(1-\nu_r)}\frac{{t_r}^2}{(t_n L^2)}Z' \tag{3.1}$$

Herein E_s is the Young's modulus, v_s the Poisson ratio, L the length of the spiral and t_r and t_n the thickness of the relaxed and nucleation layer respectively. The original radius of curvature in this equation is replaced by the approximation $R \approx L^2/2Z'$. The work of Tian et al. determined a tensile nucleation layer thickness of 2 nm and a Poisson ratio of 0.069 for thin NCD films [30].

Thermal stress The kirigami structure is designed to deform under influence of the compressive stress that originates from the mismatch in thermal expansion coefficient. The respective difference between the diamond film ($\alpha_{NCD} \sim 2.0 \cdot 10^{-6}K^{-1}$ at 298 °C [49]) and the silicon substrate ($\alpha_{Si} \sim 2.5 \cdot 10^{-6}K^{-1}$ at 298 °C [49]) imposes stress as the sample cools down from the high temperatures during CVD growth. Once suspended, a doubly-clamped diamond film releases compressive stress by buckling up or down as observed for the thin beams shown in Figure 3.3. A optical profilometry image of these beams is present in Appendix I. Similar NCD beam buckling is demonstrated in the work of Guillén [25]. In the present circular configuration, stress acts radially inward and gets redirected along a network of doubly-clamped beams that buckle in series, such that each individual deflection adds to the total deflection. In case all beams buckle in the same direction, a valley or dome-shaped structure is formed, a modelled version showing this mode is presented in Appendix I.
The SEM image in Figure 3.9a shows the underetched diamond kirigami structure. The bright outer ring represents the diamond film that is laterally underetched and freestanding, the inner adjacent dark ring (width ~30 µm) shows the fixation of the diamond film to the silicon substrate and the 'perforated' diamond membrane is fully suspended.

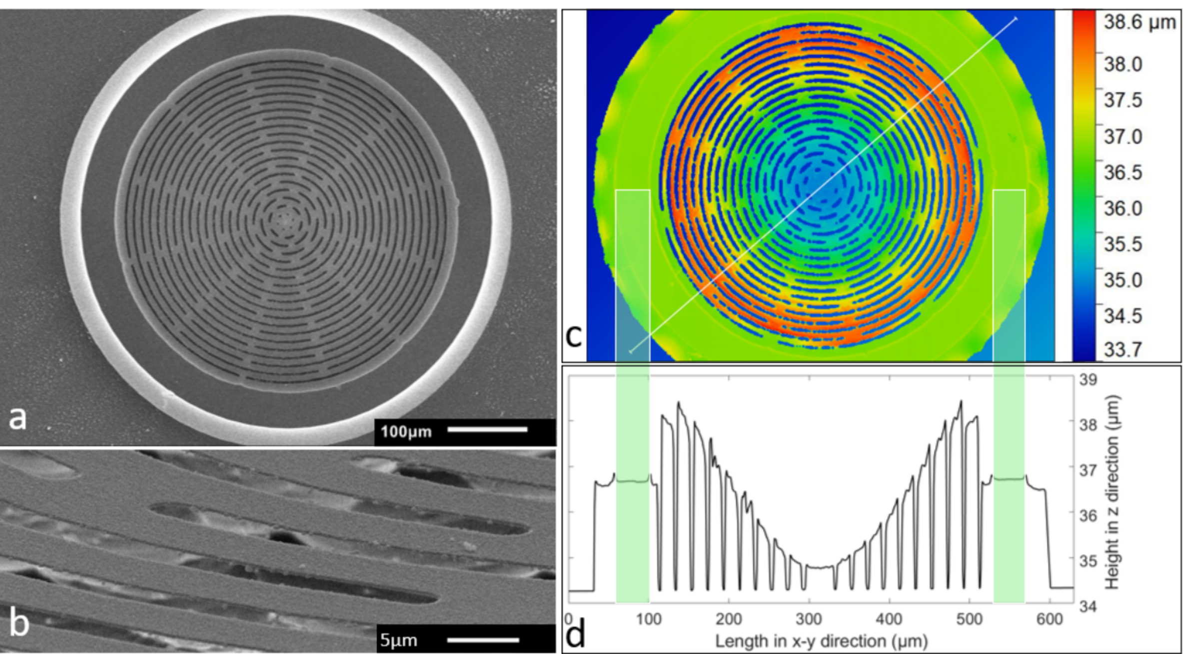

Figure 3.9: a) A SEM image of the suspended diamond flower (kirigami) membrane. b) A zoom-in showing the high resolution of the patterning and NCD growth. c) A height profile of the suspended structure obtained by 3D profilometry. Compressive stresses in the film act radially inward and get redirected via the alternating beams. Close to the fixed rim these beams buckle upwards, shown by the abrupt change in color (green to red). Further inward the color changes gradually (i.e. red to blue) indicating downward bending. Around the perimeter the film forms bulges (yellow) to reduce stress. The white line marks the measured line profile. d) Line profile showing relative height and orientation of the NCD membrane. The rim where the NCD film is still attached to the silicon substrate is highlighted by the green bars.

A side-view zoom in on the suspended thin film membrane and its granular structure is shown in Figure 3.9b. A high definition patterning is discerned along with an effective removal of stray particles found after CVD growth (Figures 3.7b and d). Height profiles of the structures were provided by white light interferometry as depicted in Figure 3.9c. The outer, suspended ring deforms in the form of alternating bulges around the perimeter to minimise the compressive stress. The suspended circular membrane shows similarities to both anticipated shapes (i.e. valley and dome). As expected, the longer beams closest to the fixed ring buckled upward with the highest amplitude as critical buckling stress scales with squared reciprocal beam length (eq. 3.2). Upward buckling is also observed in the second and even third row of beams although less pronounced. Due to this stacked buckling a maximum relative membrane height of 2.4 μm is reached at about 20 μm from the inner edge of the fixed ring. From this point inward, elevation decreases to a minimal value of -3.2 μm in the centre of the membrane. These relatively subtle deformations were anticipated regarding the high stiffness of the material. Form the graph shown in Figure 3.9d it is evident that the beams are turned (i.e. torsion) slightly towards the centre. This implicates that the beams (partially) release their compressive stress in lateral torsional buckling. The corresponding rotated orientation of the beams is transferred down to the centre and may be assigned as main contributor to the downward deflection of the centre. The rotation is presumably caused during the etching process as all beams are suspended before the relatively big centre is released. Beams with the tendency to buckle upwards are forced down by the anchoring effect of the fixed centre. This induced preference for bending down remains intact after the centre part is released. A suggestion for future work is to pattern a hole in the middle of the pattern so that the structure gets underetched from the inside radially outward. An indicative measurement of the compressive stress is based on the amplitude of the longest beam in the flower pattern (closest to the fixed rim) and the thin beams depicted in Figure 3.5 using the following equation (obtained from [50]).

$$\sigma = \frac{E\pi^2}{L_{eff}^2}(\frac{A^2}{4} + \frac{t^2}{3}) \tag{3.2}$$

Herein E resembles the Young's modulus, A the amplitude of buckling, L_{eff} the effective beam length and t the thickness of the NCD film. Both structures are grown to a thickness of 150 nm under identical standard CVD conditions. Deflection in the curved beams is translated to a compressive stress of 67 MPa based on an effective beam length of 195 μm and a buckling amplitude of 1.3 μm. A compressive stress of 95 MPa was found for the straight beams with effective length 400 μm and 3.2 μm deflection, see Appendix I. This discrepancy between the curved and straight beams validates the aforementioned notion of stress release by lateral torsional buckling. Obtained stress values correspond to values found in literature as they lie within the range of 0-390 MPa determined in a study on HFCVD grown NCD [25].

3.4. Conclusion

A high resolution patterning method for bottom-up diamond growth is presented in this work. It enables rapid prototyping by the maskless lithographic method that is used to create the photoresist stencils on a silicon substrate. These stencils ensure selective seeding prior to HFCVD growth process. Thin (150 nm) NCD films grew on seeded areas, reaching a minimal linewidth of about 2.3 μm. Particular patterns were designed for the investigation of two distinct components of residual stress present in the diamond film, i.e. gradient stress and compressive planar stress. The structures were underetched and subsequentially analysed on their out-of-plane behaviour.

Excessive downward bending of singly supported structures made a qualitative evaluation of the gradient stress impossible. Compressive stress was determined form buckled beams in a doubly clamped configuration and yield 67 MPa. This is in accordance with stresses found in literature for HFCVD grown NCD (i.e. 0-320 MPa). For diamond structures to bend in a controlled manner, more experiments are required. Analysis on identical structures grown under varying CVD conditions will provide a better understanding of the stress distribution in the film. Furthermore the designs need some minor adaptations to ensure that the various parts of the patterns are suspended in the correct order, in this case inside out.

4

Conclusion

Patterning diamond for high performance MEMS and NEMS applications has long been reserved for top-down methods like FIB milling and RIE. Although still inferior, cheaper bottom-up methods are closing the gap. The presented work contributes to this catch-up by reporting two novel patterning techniques. The first method, worked out in **Chapter 2**, demonstrated the applicability of a microfluidic AFM-based system for the synthesis of freestanding nanocrystalline diamond doubly clamped resonators. A hollow AFM-cantilever with an opened pyramidal tip was used as a micro-scale fountain pen writing with nanodiamond ink. Thin (~1 µm) dumbbell shaped patterns composed of lines (~60 µm width, 600-1000 µm length) and droplets were grown and suspended by RIE. Laser Doppler vibrometry determined resonance properties of piezoelectrically actuated 375 µm, 472 µm and 617 µm long beams in air and reached a maximum quality factor of 309. The second project, **Chapter 3**, reduced the minimum linewidth by a factor ~20 using lithographic stencils for selective seeding. High resolution diamond patterns (150 nm thick) with a minimal feature size of 2.3 µm were grown during a 15 minute CVD cycle. In an attempt to reach some level of 3D structuring, specifically designed patterns were grown and suspended. Under influence of residual stresses these structures bent and buckled out-of-plane. Based on the amplitude of buckling 1.3 µm in a 195 µm long beam, an estimated compressive planar stress of 67 MPa was calculated. Unfortunately no vertical gradient stress could be determined.

Hollow AFM-cantilever based diamond patterning demonstrated its excellent use for writing smooth lines. Downscaling the current linewidth to dimensions matching the orifice requires further optimization though. Thinner lines would then allow resonator structures to shrink and consequently raise their resonance frequencies. To raise corresponding Q-factors simultaneously, alternatives must be found for the beams endpoints. The irregular shapes of the currently used droplets affect the vibrational properties of the beams and make it impossible to adequately simulate the structures with FEM methods.
The pioneering work of combining maskless lithography with bottom-up diamond growth shows huge potential. Besides the unprecedented 2D patterning freedom that was acquired, it provides a foundation for rapid prototyping of CVD diamond patterns. Possibly, this technique may contribute to a more frequent use of diamond as practical material in microscale applications. A preliminary attempt was made to introduce thin film diamond as a viable material for deterministic bending or buckling to create self-assembled 3D geometries (i.e. origami or kirigami). This technique has proven its relevance throughout a multitude of material classes on various length scales. Partially suspended structures used in this work displayed bending and buckling, yet more experiments are required for knowledge and control over the stress distribution in the film.

Adding a third dimension to CVD diamond patterning is currently out of reach, yet some preliminary ideas for future work are proposed in the outlook, **Chapter 5**.

5

Outlook

The promising results in this pioneering work advertise for follow-up studies to further investigate the combination of NanoScribe and CVD diamond growth. Research could, for example, aim at improving the currently used method to be faster and cleaner (i.e. less stray particles). Another option could be the development of a whole new concept that incorporates NanoScribe's 3D microfabrication capabilities. Recommendations and global ideas for future work are summed up below.

- A standardized in-house procedure was used to coat silicon samples with a 10 µm layer of AZ4562 photoresist. Thickness may be reduced (e.g. higher angular spin-coat speed, changing to less viscous photoresist) as it does not affect selective seeding. This reduces the exposure time in the NanoScribe tool as only one slice is required to fully expose the layer. It may also improve the effectiveness of the rinsing process as superfluous seeds are flushed more easily from shallower trenches.
- The working principle of two photon polymerization was described in detail on purpose, as preliminary ideas for 3D patterning of diamond exist that incorporate the 3D functionalities NanoScribe has to offer. So far, it has been difficult to combine 3D printed polymeric structures with the harsh conditions of CVD diamond growth. Two ideas bypassing this problem are posed below.
  - Bauer et al. [51] showed the possibility to pyrolyse IP-Dip, a standard NanoScribe negative photoresist. Heating such 3D structures in a vacuum causes the material to shrink (~80%) and turn into glassy carbon [52]. Glassy carbon withstands the extreme conditions during CVD and could therefore be used as 3D template in diamond growth. Adequate surface treatments may accommodate the problematic seeding of glassy carbon with nanodiamond particles. If sufficiently seeded, CVD will provide the 3D structure with a conformal nanocrystalline diamond coating.
  - Another potential 3D method involves the use of nanodiamond laden photoresist. In 2D, this method already showed to be successful for appropriate concentrations (i.e. 0.45 wt.%) [19]. Printing 3D structures with the NanoScribe tool operating in conventional mode (i.e. the objective immersed in oil focused into the photoresist on the top-side of a transparent coverslip) prevents the seeds from scratching the objective. Exposing such structures to CVD may cause nanodiamond seeds on the exterior to coalesce rapidly and form a stable framework from which a uniform diamond layer can grow.
- Boron doped nanocrystalline diamond can be grown from seeded patterns as soon as the new CVD reactor is operative. This creates possibilities for the bottom-up fabrication of conductive diamond circuits with strong potential in MEMS and microelectrode technologies, among others.
- A final objective is the creation of a functional device comprising the diamond micro component along with peripheral parts (e.g. piezo actuator, ohmic contact points etc.) for high performance sensor applications like masssensors, biosensors or microelectrodes for detection.

Nanodiamond ink preparation

The nanodiamond ink dispensed from the hollow AFM cantilever consists of 3 components; a *NanoAmando* nanodiamond dispersion of 50 mg/mL concentration, deionised water and ehylene glycol (EG). As only little volume is required the following composition was used.

- 25 µL Nanodiamond dispersion
- 175 µL DI water
- 300 µL EG

Before use the mixture is ultrasonicated for 15 minutes.

Figure A.1: Optical image showing two containers, one holding the nanodiamond dispersion (right) and one holding to plain water (left) for comparison.

Contact angle measurements

This appendix shows the images corresponding to the contact angle measurements performed with the *Thetalite Tensionmeter*. Contact angles and surface free energies are added in caption. The method used to create a gradient is shown in Figure B.2.

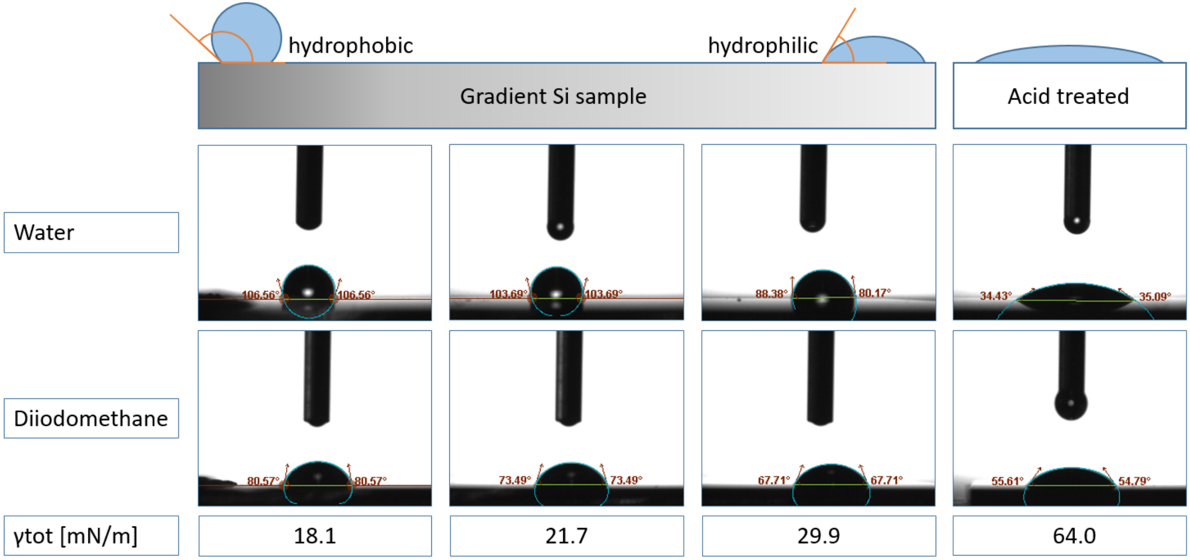

Figure B.1: Figure showing the contact angle measurements on the gradient samples and on acid treated samples. Contact angles for water are (fltr) 106°, 103°, 80°. Contact angles for diiodomethane 80°, 73°, 67°. Based on this data built-in software found corresponding surface free energies of 18.1 [mN/m], 21.7 [mN/m] and 29.9 [mN/m] for the gradient sample. A surface free energy of 64.0 [mN/m] was found for the acid treated sample with contact angles being 34° (Water) and 55° (Diiodomethane).

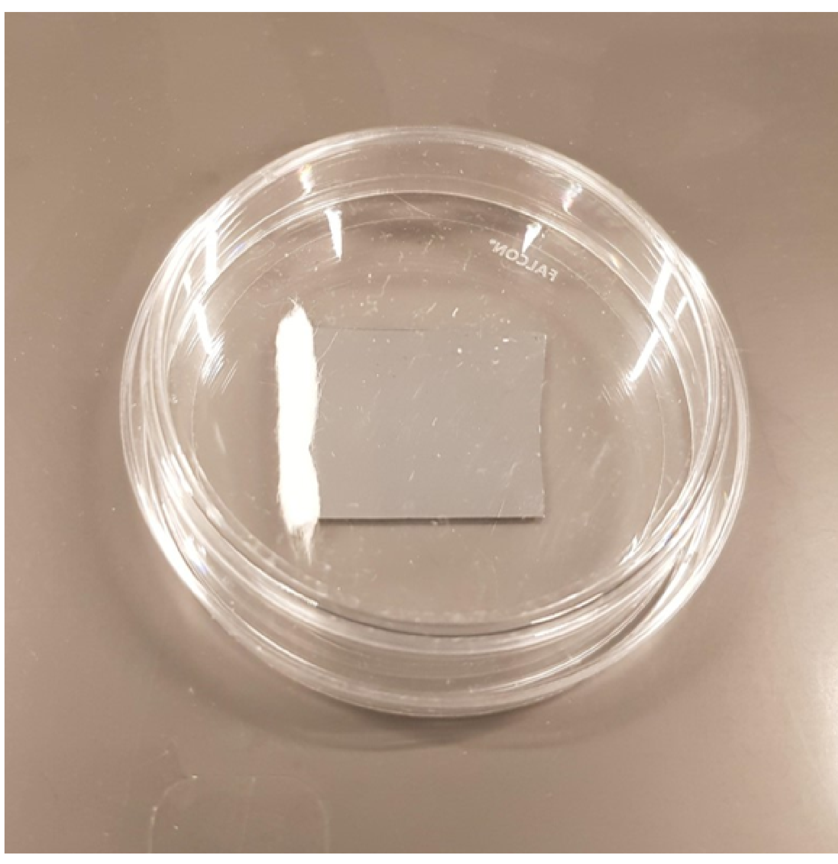

Figure B.2: Optical image showing the configuration to create a silicon sample with gradient in wettability. The cloth (positioned left) is soaked in trichloro(dodecyl)silane and slowly evaporates, gradually covering the surface with hydrophobic silanes. During the process the petridish is sealed from the outside with parafilm.

Regrowth of written patterns

After an initial CVD growth cycle diamond structures formed with partially discontinuous features, as is shown in Figure C.1. From the height profile depicted in Figure C.3 some distinct features can be observed. The central part of the droplet, the area that is wetted directly as the droplet touches the substrate forms a uniform film of ~ 500 nm. This area is encircled by a rim of increased thickness which implies a locally higher seed density, possibly induced by the coffee stain effect. The peripheral areas are wetted later, i.e. after the line of contact shifts outward in a stepwise manner. These areas lacked the required seed density to from a continuous film. Around the outer edge of the droplet though, another rim of increased seed density is present. Figures C.2 and C.4 show that after a second CVD cycle these features are flattened out and form a uniform layer of about 1 μm thickness.

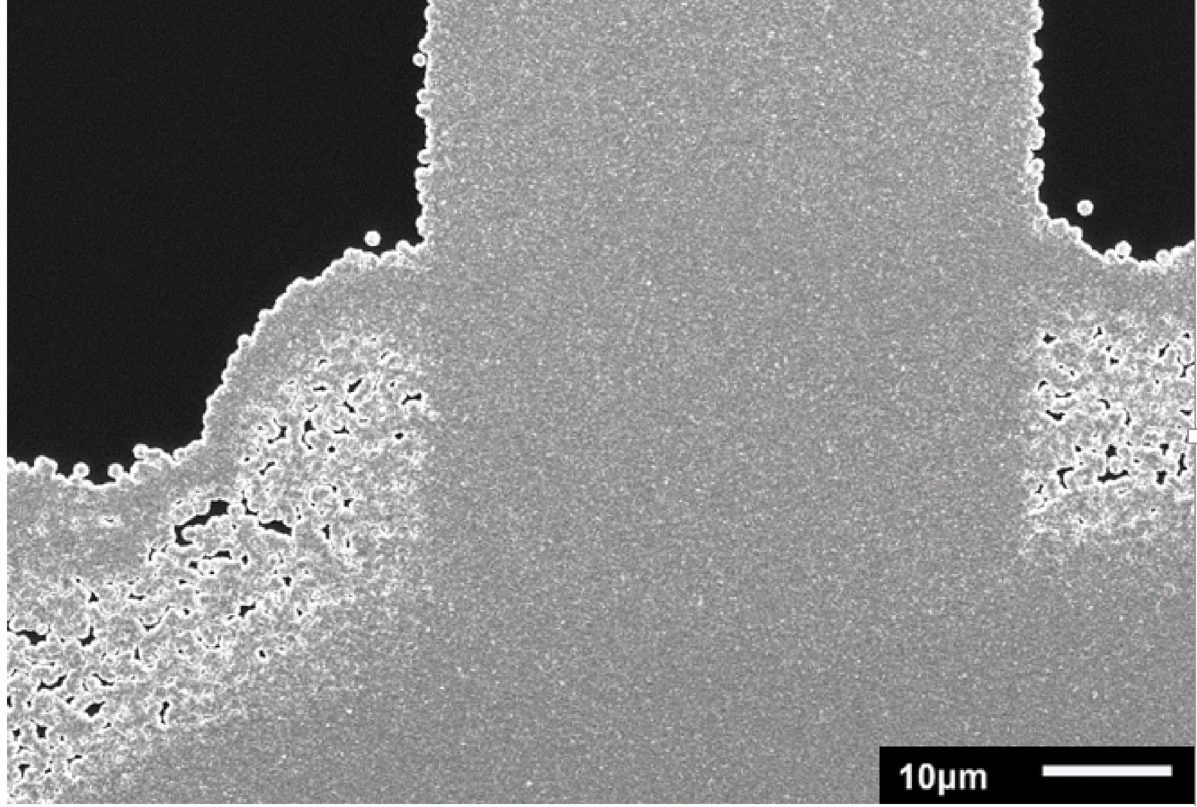

Figure C.1: SEM image depicting the discontinuities present in the diamond film after first CVD growth cycle. In contrast to the line and central part of the droplet, the outer rim of droplet is not fully closed.

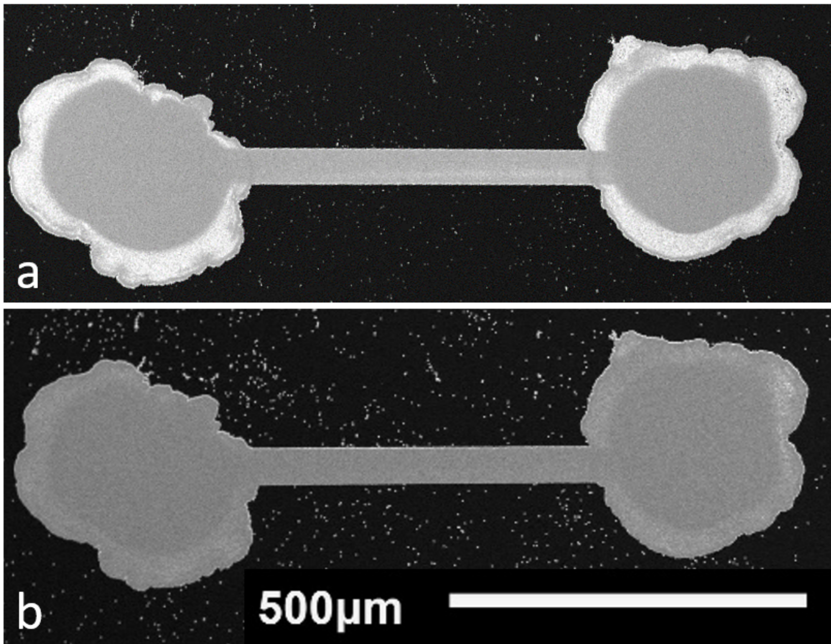

Figure C.2: SEM image depicting the dumbbell shaped structures before (a) and after (b) regrowth. The discontinuous areas of bright contrast turn darker as the film fully closes .

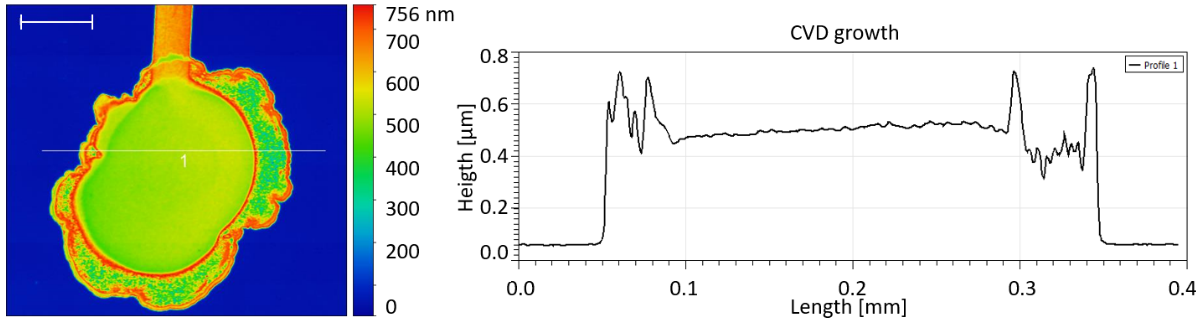

Figure C.3: Height profile of the droplet before CVD regrowth. The scale bar resembles 100 µm.

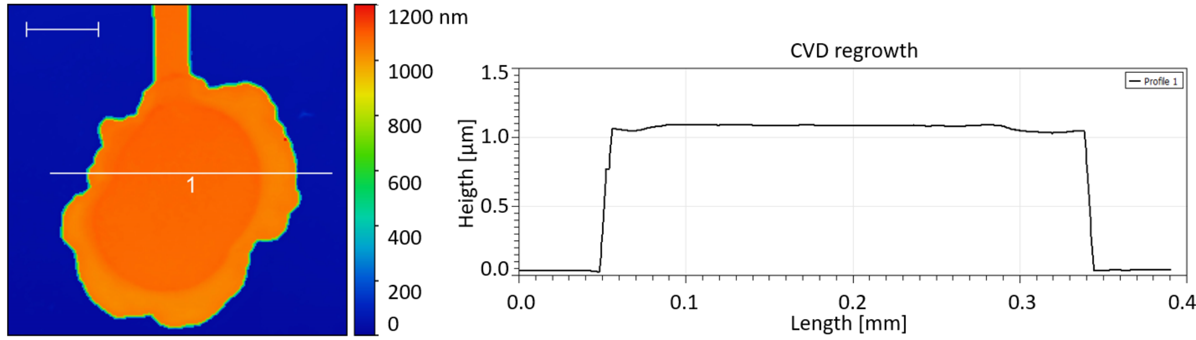

Figure C.4: Height profile of the droplet after CVD regrowth. The scale bar resembles 100 µm.

Suspended resonator structures

Reactive ion etching of the silicon substrate suspended the diamond dumbbell structures and turned them into doubly clamped resonators. The arrangement of structures on the silicon sample is depicted in Figure D.1. On a separate sample, another type of doubly clamped cantilevers was suspended. In this configuration all parallel beams are connected by two big transversal beams, see Figures D.2 and D.3. No frequency studies were performed on this sample due to excessive underetching.

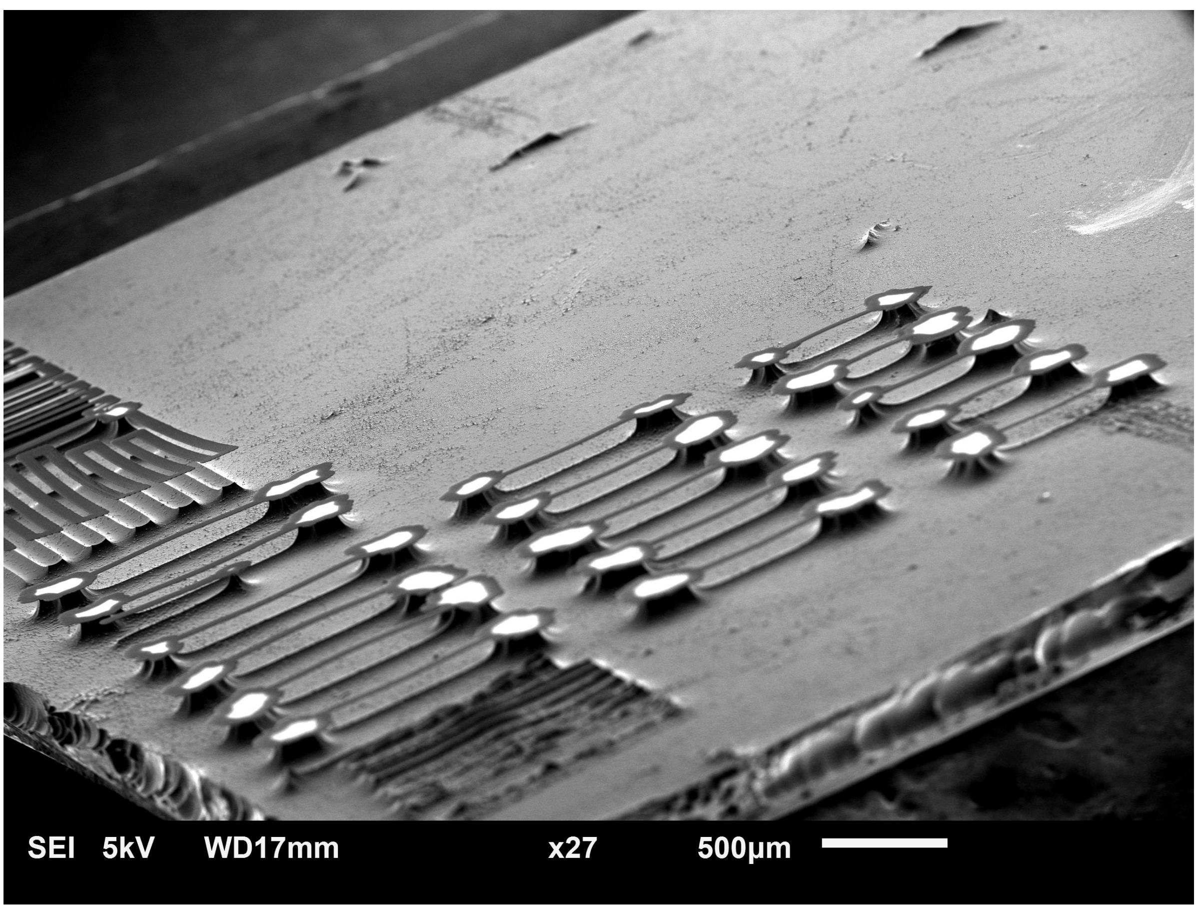

Figure D.1: SEM image depicting the arrangement of the suspended diamond structures on the silicon substrate.

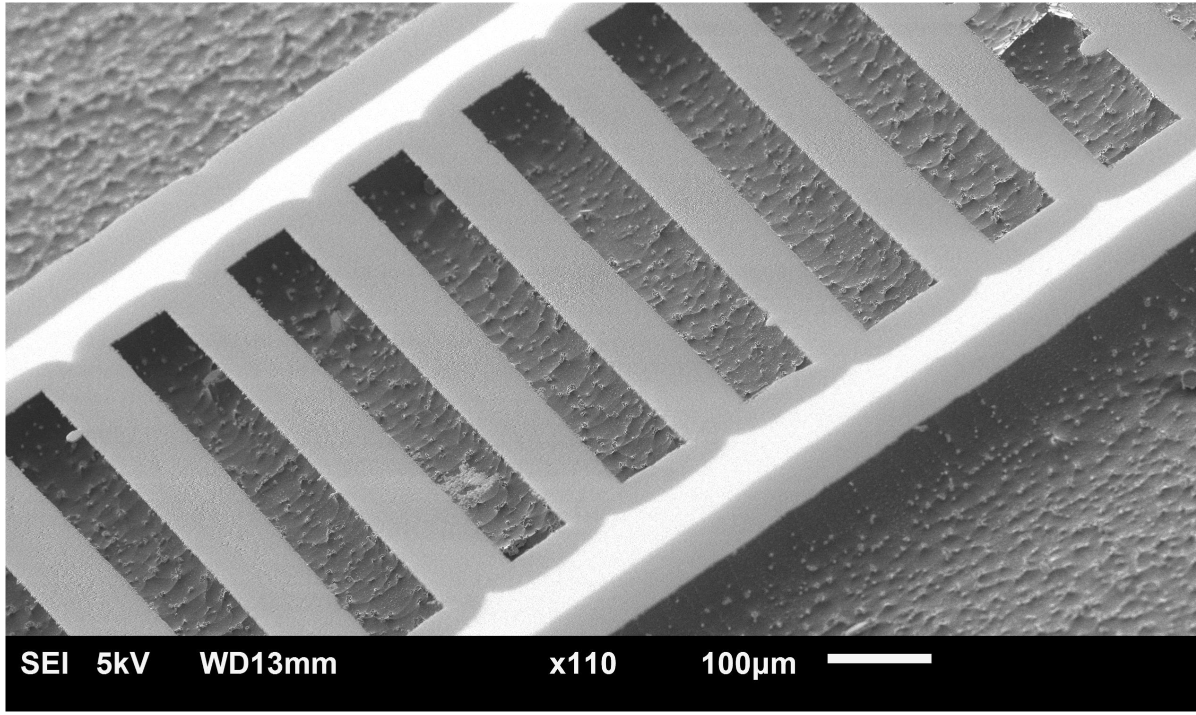

Figure D.2: SEM image depicting an alternative pattern of suspended doubly clamped beams. In this case parallel beams connected by two wider transversal beams.

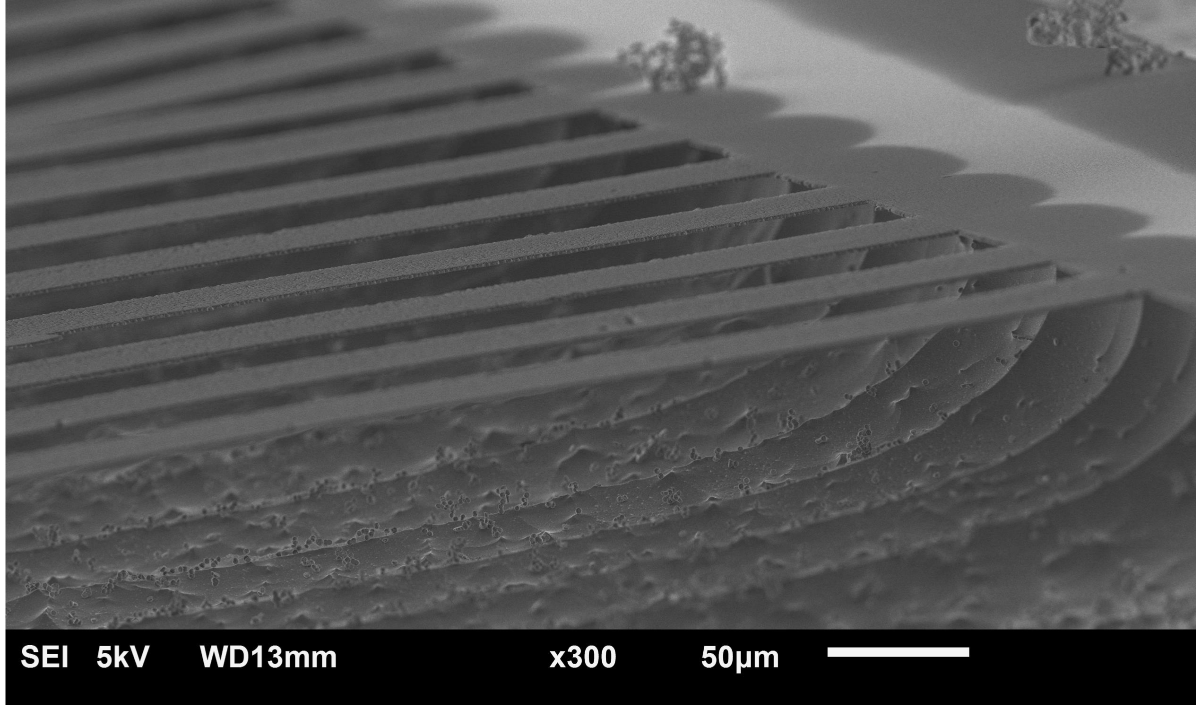

Figure D.3: SEM side view of the suspended parallel beams connected by a wider transversal beams.

Besides the doubly clamped structures also singly clamped cantilever structures were created and showed upward bending, Figures D.4 and D.5.

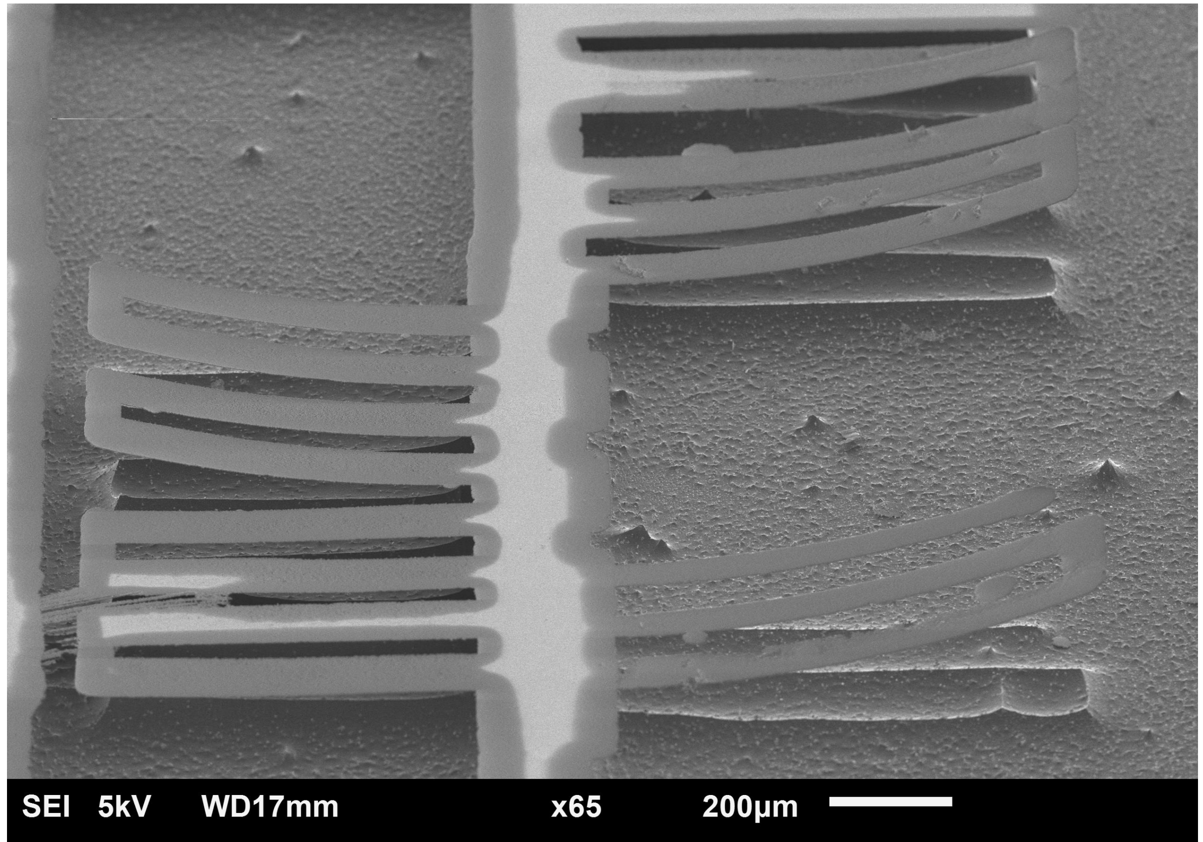

Figure D.4: SEM image of 'singly' clamped cantilevers bending up.

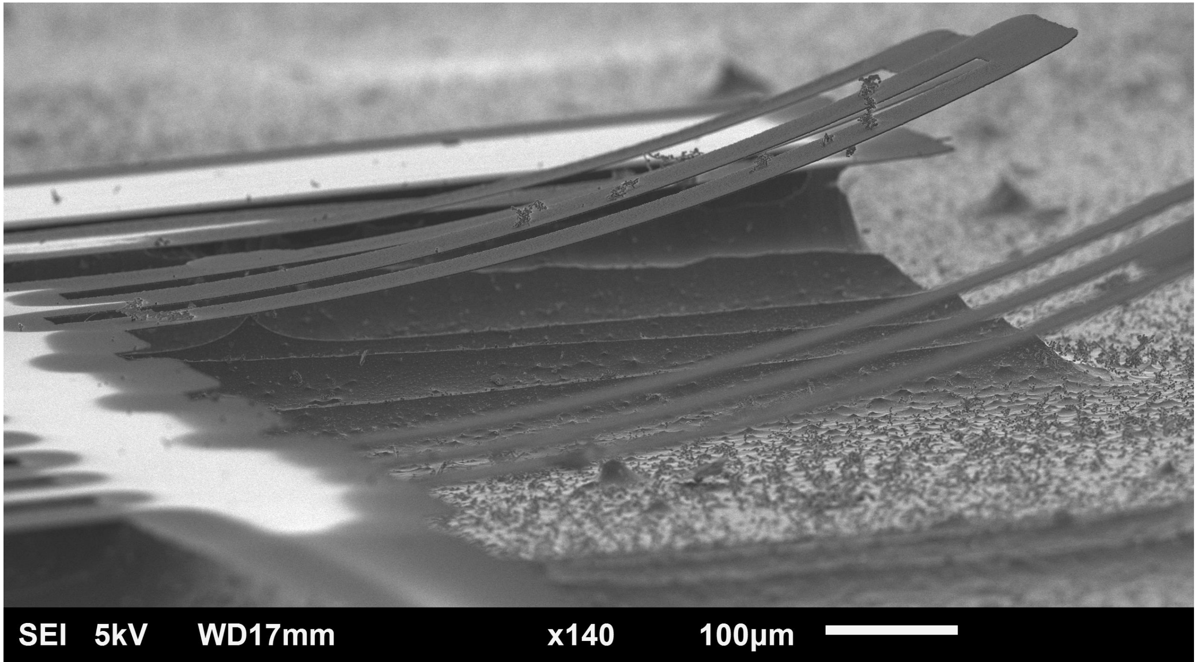

Figure D.5: SEM side view of 'singly' clamped cantilevers bending up.

Laser Doppler vibrometry

Small sized beam

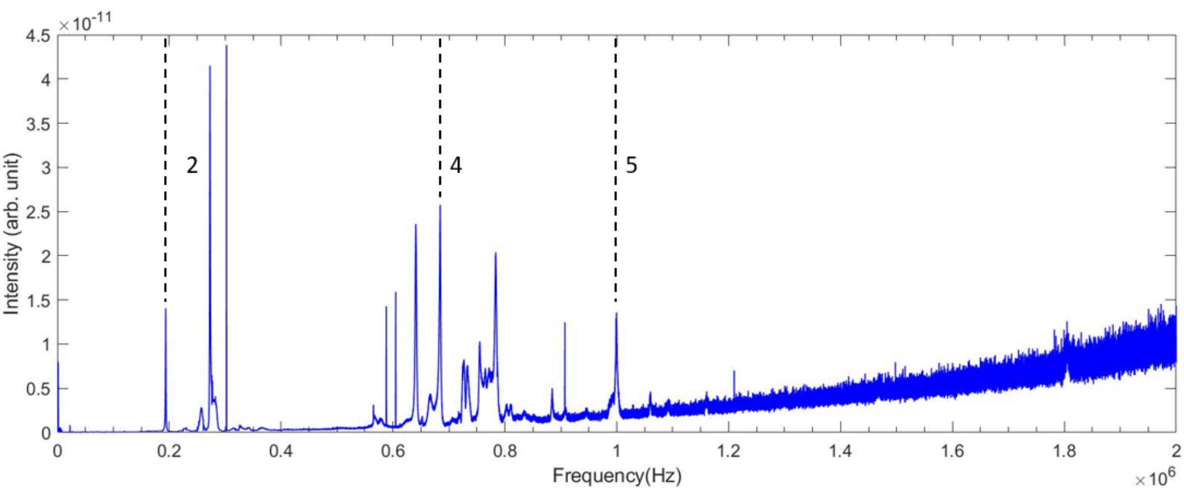

Figure E.1: Frequency spectrum of the small sized beam. Resonance frequencies are indicated dotted lines.

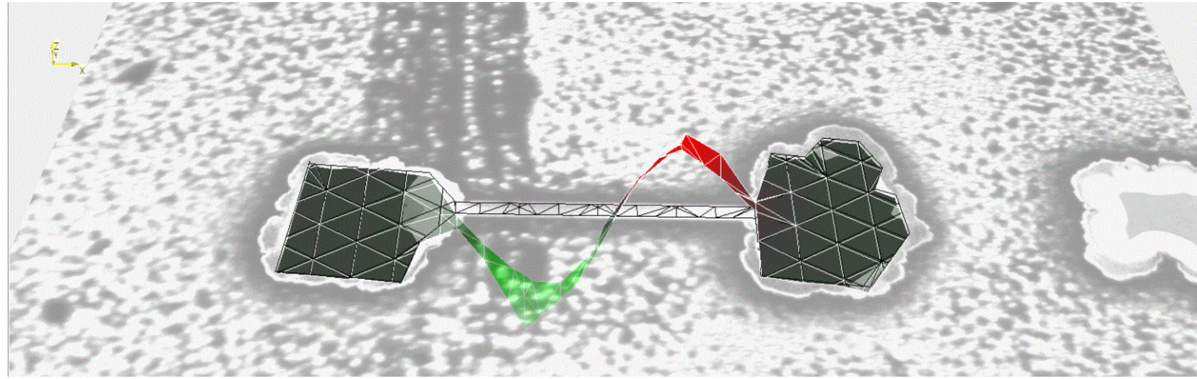

Figure E.2: Animated representation of the second resonance mode at Hz.

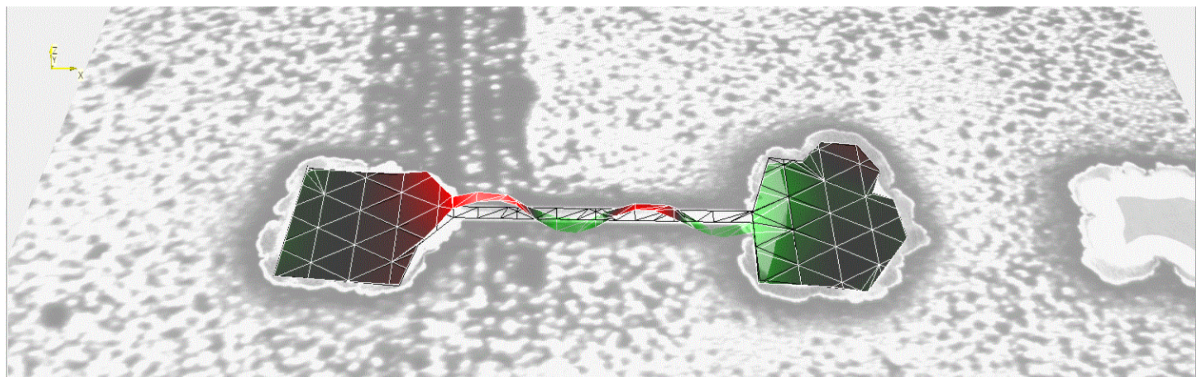

Figure E.3: Animated representation of the fourth resonance mode at Hz.

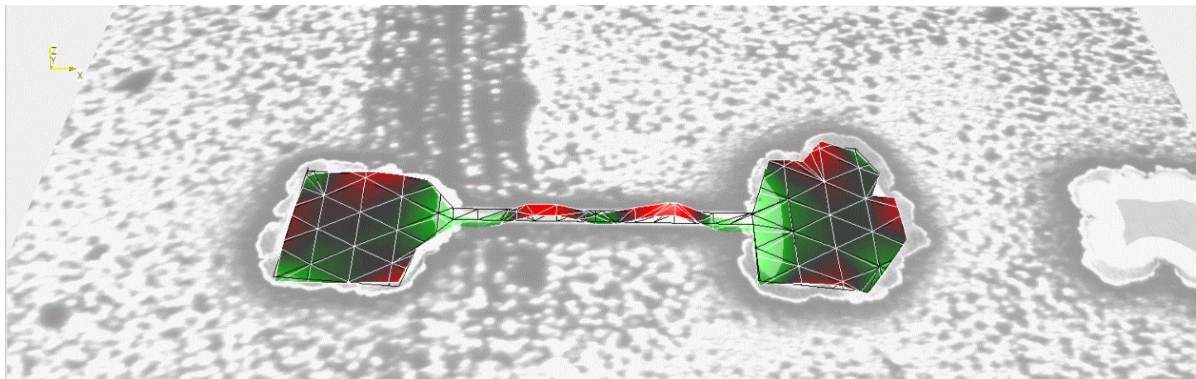

Figure E.4: Animated representation of the fifth resonance mode at Hz.

Medium sized beam

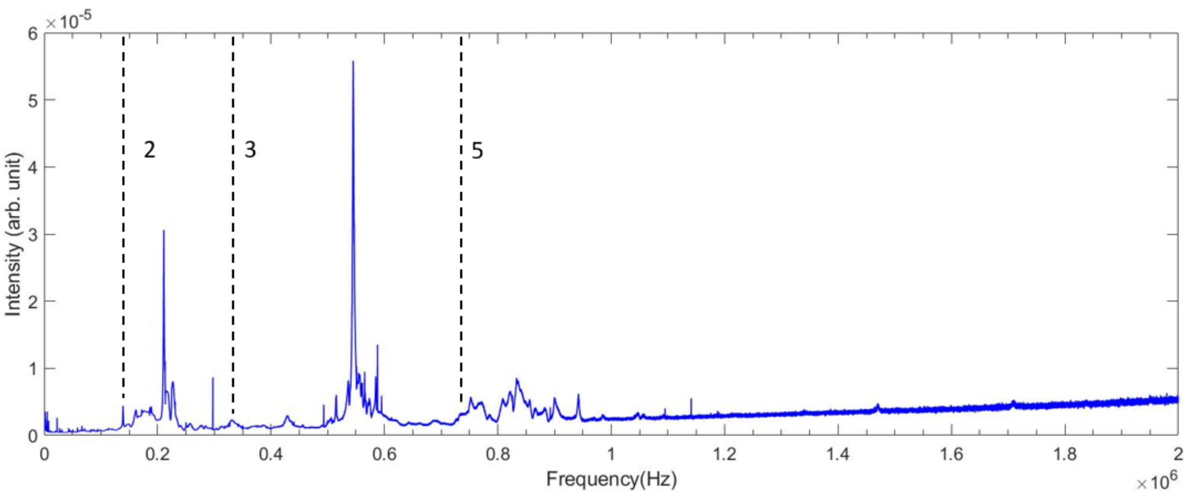

Figure E.5: Frequency spectrum of the medium sized beam. Resonance frequencies are indicated dotted lines.

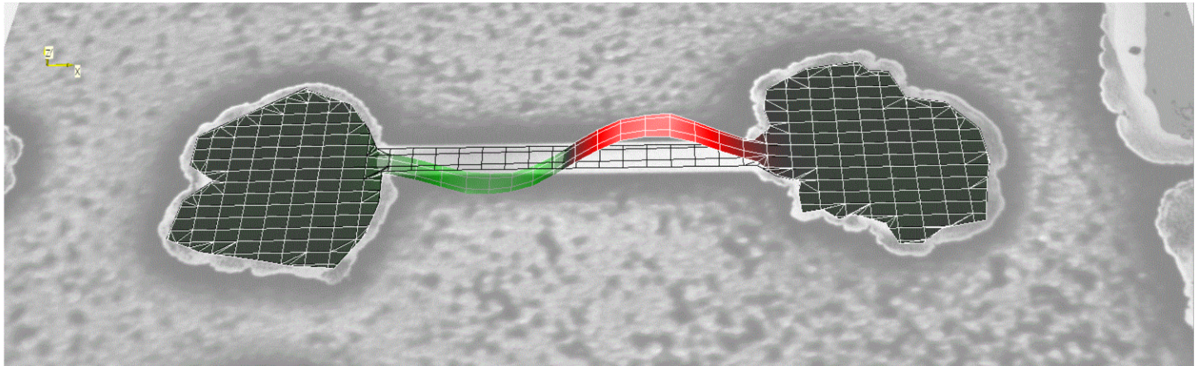

Figure E.6: Animated representation of the second resonance mode at Hz.

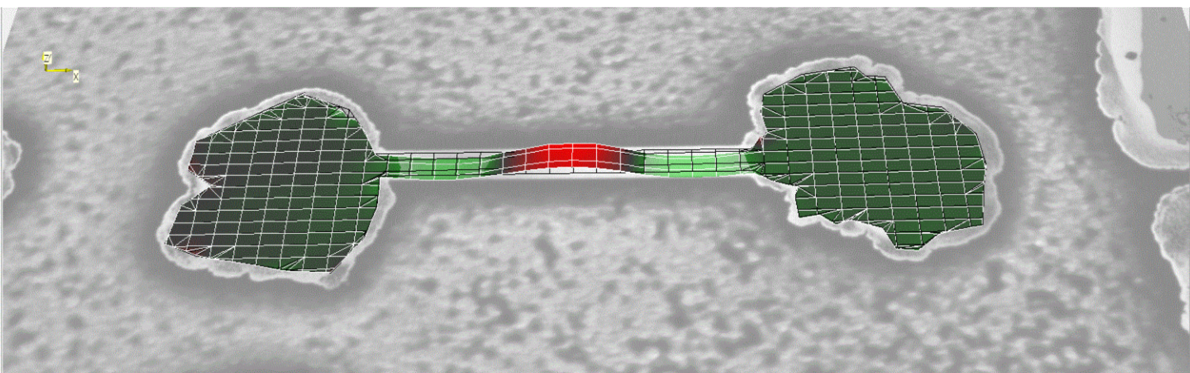

Figure E.7: Animated representation of the third resonance mode at Hz.

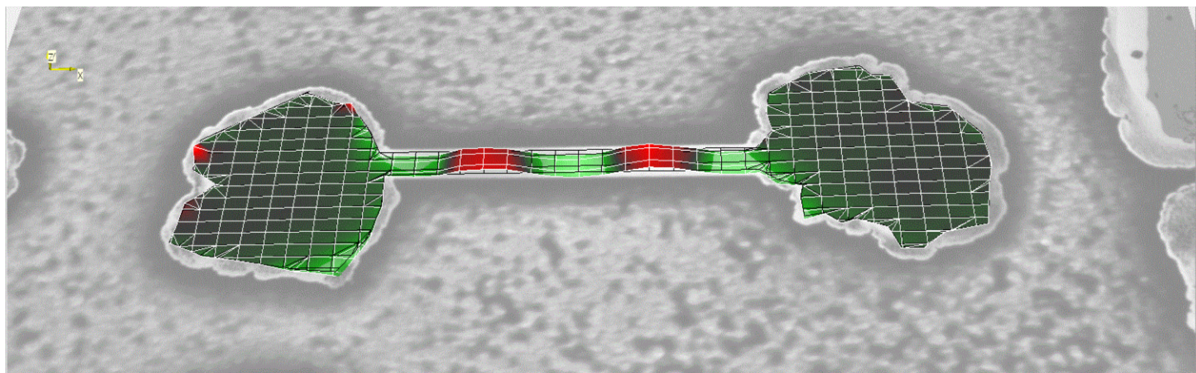

Figure E.8: Animated representation of the fifth resonance mode at Hz.

Long sized beam

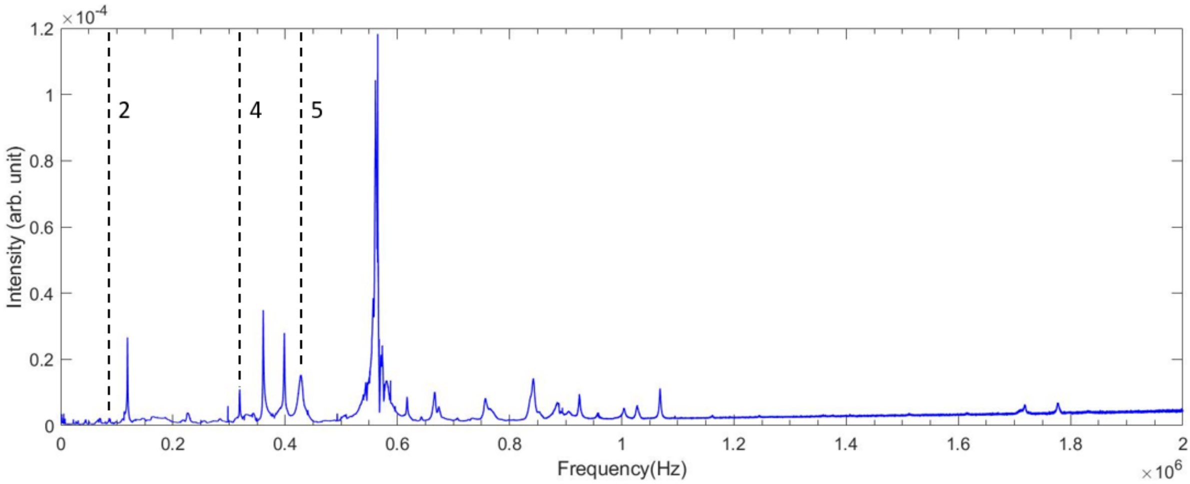

Figure E.9: Frequency spectrum of the long beam. Resonance frequencies are indicated dotted lines.

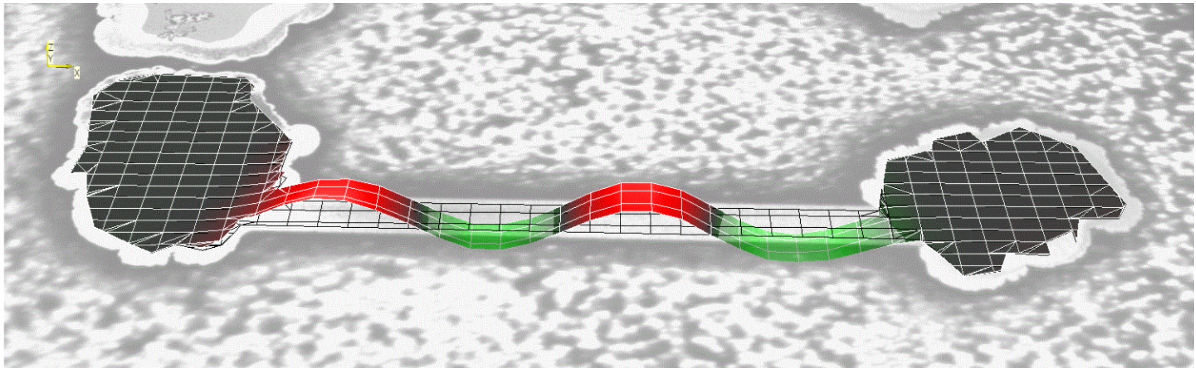

Figure E.10: Animated representation of the fourth resonance mode at Hz.

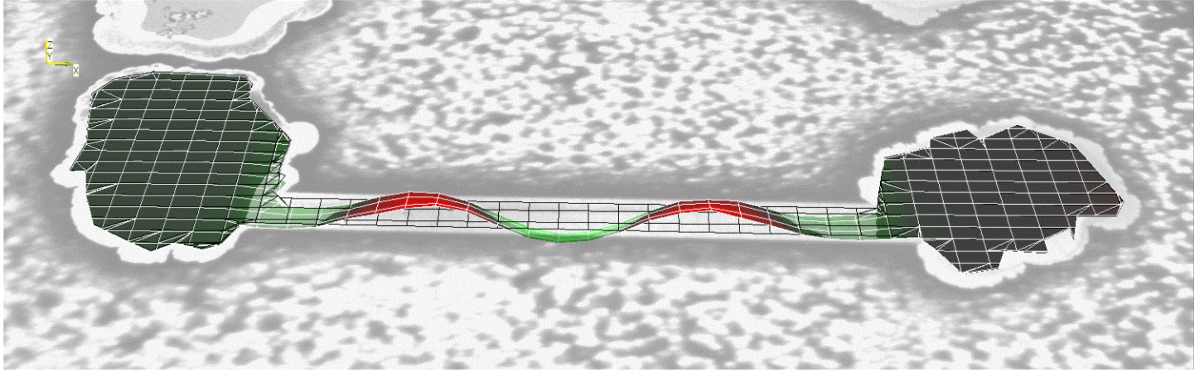

Figure E.11: Animated representation of the fifth resonance mode at Hz.

Extra

More higher order resonance modes were detected in other cantilever beams. A selection is depicted in Figures E.12 to E.15.

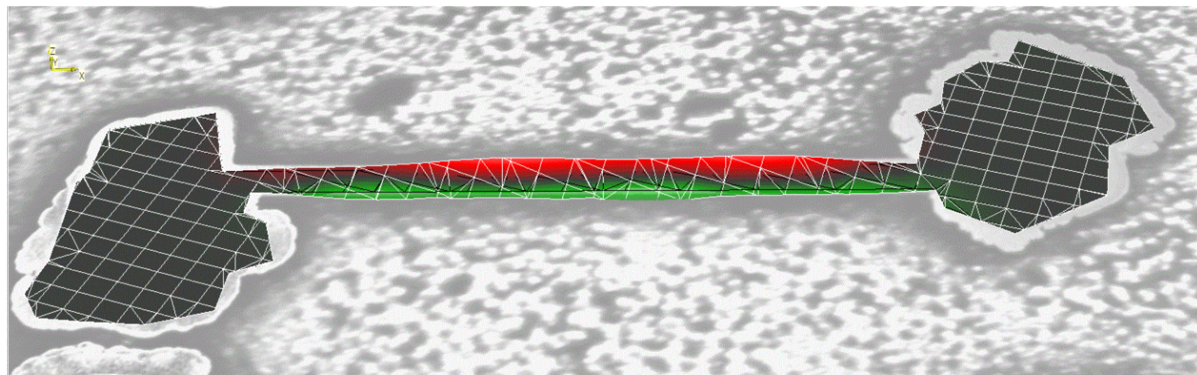

Figure E.12: Animated representation of a first torsional resonance mode.

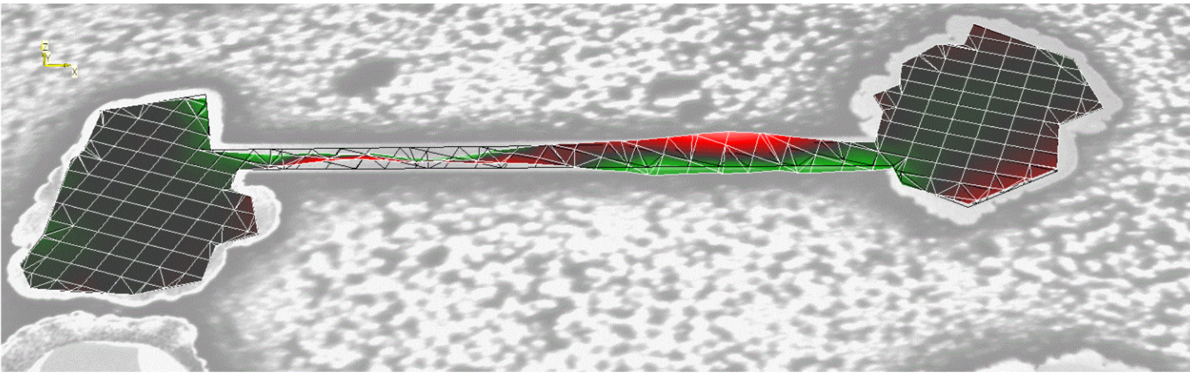

Figure E.13: Animated representation of a second torsional resonance mode.

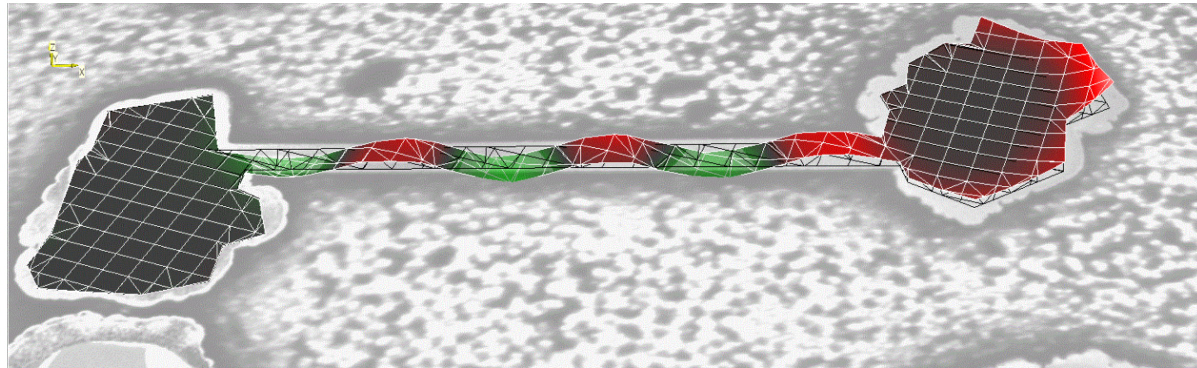

Figure E.14: Animated representation of a sixth resonance mode.

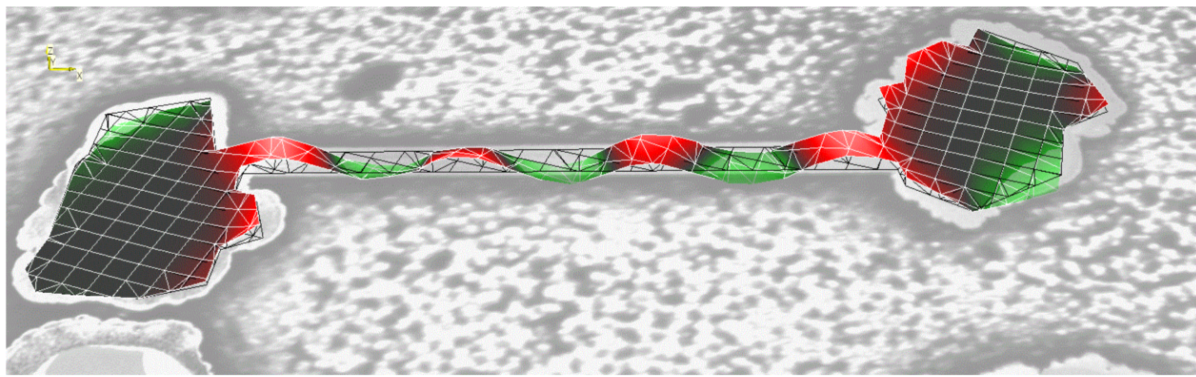

Figure E.15: Animated representation of a seventh resonance mode.

Analytic work-out frequency formula

Euler-Bernoulli beam equation:

$$-EI\frac{\partial^4 y}{\partial x^4} = \rho\frac{\partial^2 y}{\partial t^2} \tag{F.1}$$

Separation of variables F.2 provides two separate formula's; A spatial equation F.3 and a temporal equation F.4.

$$y(x,t) = Y(x)\cdot T(t) \tag{F.2}$$

$$\frac{d^4Y(x)}{dx^4} - c^2(\frac{EI}{\rho})Y(x) = 0 \tag{F.3}$$

$$\frac{d^2T(t)}{dt^2} + c^2T(t) = 0 \tag{F.4}$$

A solution for the spatial equation F.3 is:

$$Y(x) = a_1 sinh(\beta x) + a_2 cosh(\beta x) + a_3 sin(\beta x) + a_4 cos(\beta x) \tag{F.5}$$

Substitute equation F.5 and its 4th derivative in equation F.3. Then the equation satisfies for:

$$\beta^4 = c^2\left(\frac{EI}{\rho}\right) \tag{F.6}$$

Doubly clamped cantilever boundary conditions are zero displacement and zero slope at $x = 0$ and $x = L$.

$$Y(0) = 0, \left.\frac{dY(x)}{dt}\right|_{x=0} = 0$$

$$Y(L) = 0, \left.\frac{dY(x)}{dt}\right|_{x=L} = 0$$

A non-trivial solution is obtained by using the boundary conditions mentioned above. More roots satisfy equation F.7 therefore an integer index n is added.

$$cos(\beta_n L)cosh(\beta_n L) - 1 = 0 \tag{F.7}$$

Numerical method are used to calculate the values for $\beta_n L$, the first value being:

$$\beta_n L = 4.73004 \tag{F.8}$$

By writing the temporal equation F.4 (formula for simple harmonic motion) in terms of β_n (using equation F.6) the following formula for angular frequency [rad/s] is obtained:

$$\omega_n = {\beta_n}^2 \sqrt{\frac{EI}{\rho}} \tag{F.9}$$

In terms of frequency [Hz] the formula for the fundamental mode is:

$$f_n = \frac{1}{2\pi} \frac{4.73004^2}{L^2} \sqrt{\frac{EI}{\rho}} \tag{F.10}$$

The first 5 values for $\beta_n L$ are:

1. 4.73004
2. 7.85321
3. 10.9956
4. 14.13717
5. 17.27876

Maskless lithographic diamond patterns

G.1. 3D model and printing

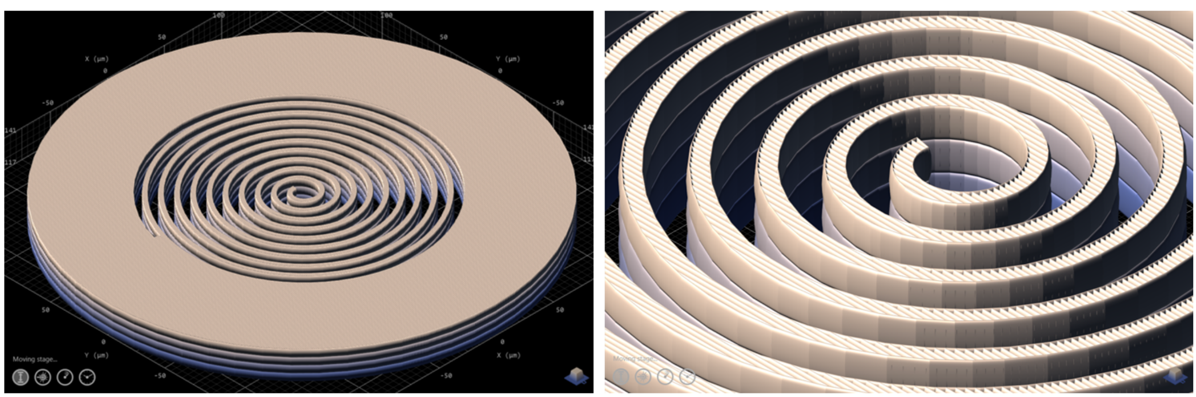

Figure G.1: A *DeScribe* model showing the stacked layers required to fully expose the 10 μm photoresist film. A zoom in illustrates the contours of the pattern and the way these are filled, namely with parallel voxel lines.

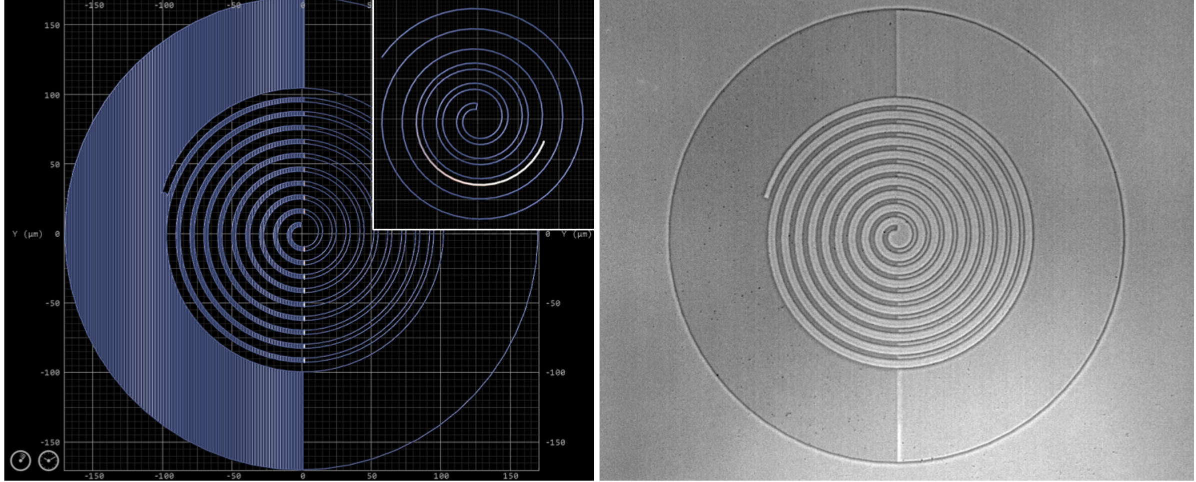

Figure G.2: Snapshot of the printing animation, the inset shows the creation of the contour. The figure on the right is a snapshot of the actual printing process.

G.2. Developed photoresist patterns

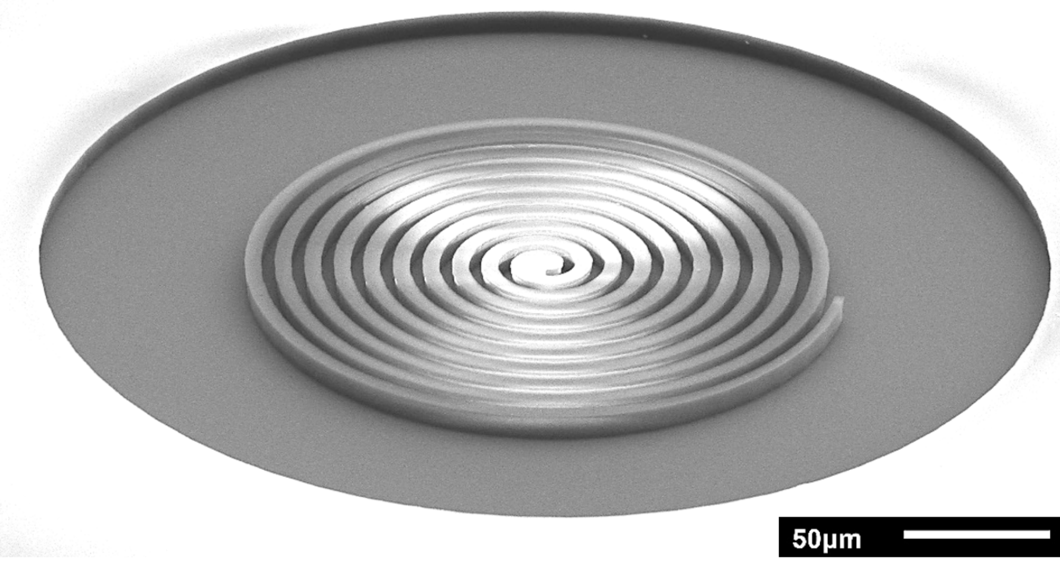

Figure G.3: A SEM image depicting the photoresist pattern that is used as stencil for selective nanodiamond seeding. Brighter areas indicate photoresist, the dark ring represents the exposed silicon substrate.

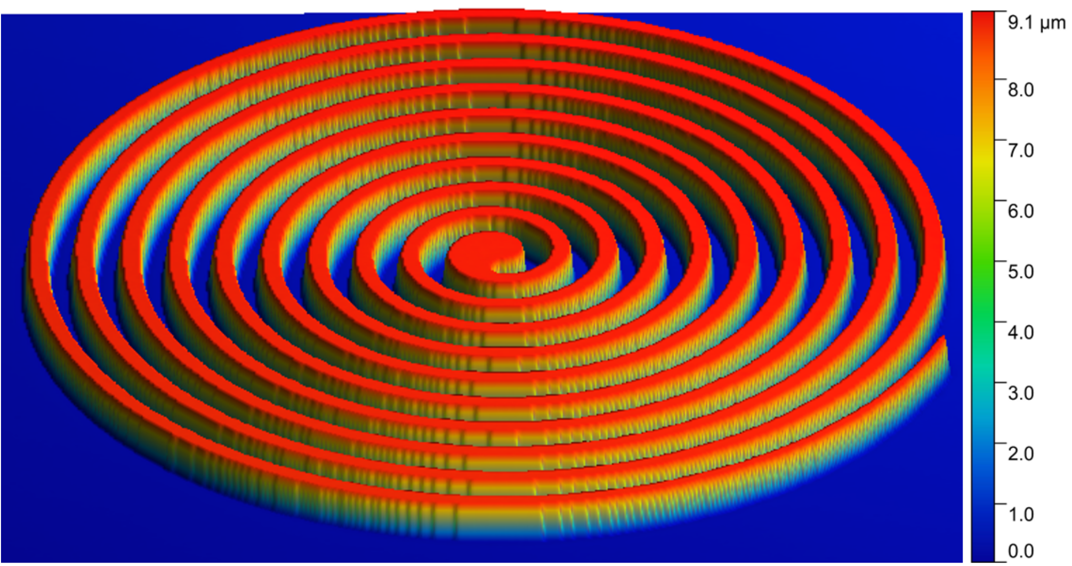

Figure G.4: 3D height profile of the photoresist spiral structure depicted above (Fig.G.3). A uniform thickness of 9.1 µm is achieved.

G.3. Nanodiamond seeding

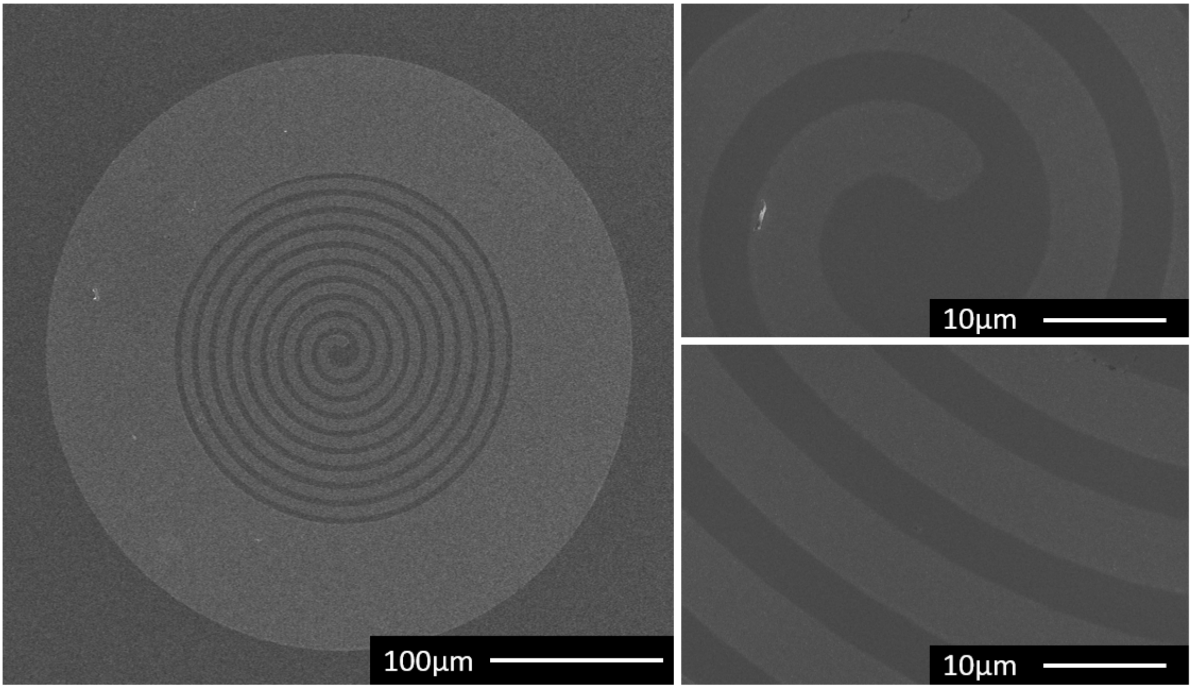

Figure G.5: High resolution SEM images depicting the high selectivity of nanodiamond seeding. The areas of brighter contrast are seeded.

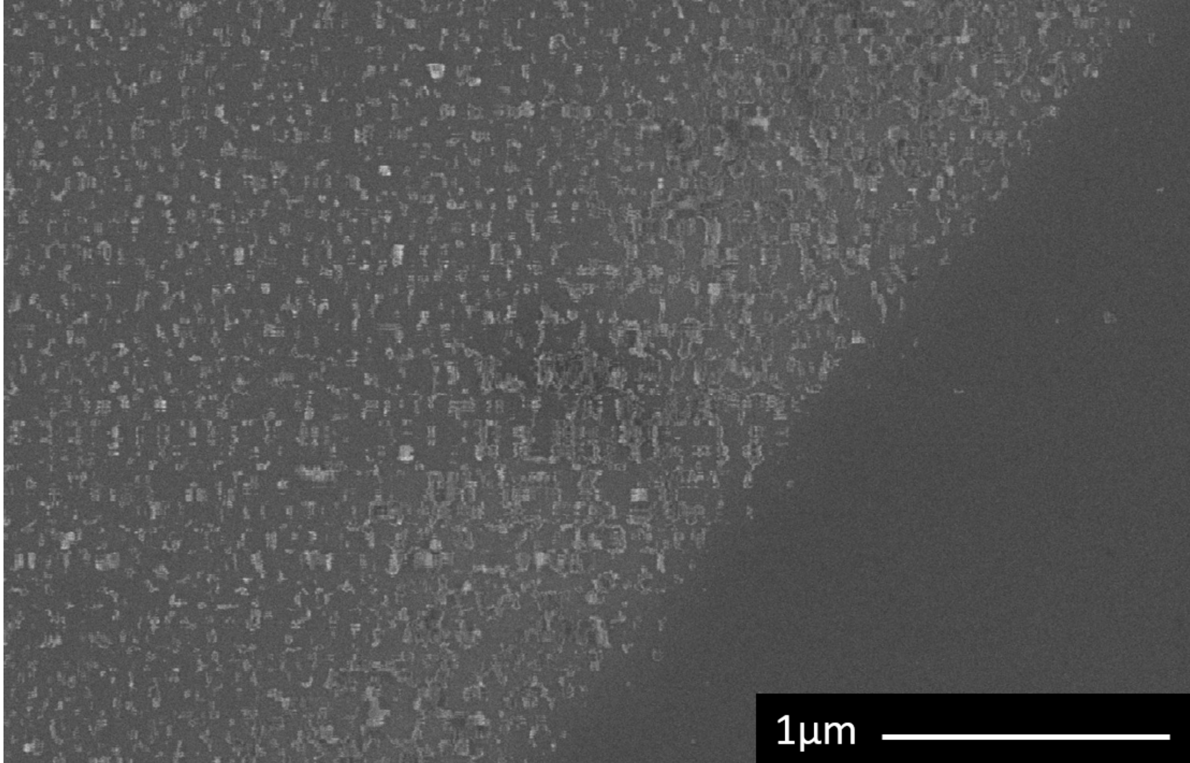

Figure G.6: A high resolution SEM image depicting the high selectivity of nanodiamond seeding. Individual seed clusters can be distinguished. (The distortion is an artefact of the HR-SEM tool itself. Due to vibrations, no clear images could be taken at this high magnification.)

G.4. CVD grown NCD patterns

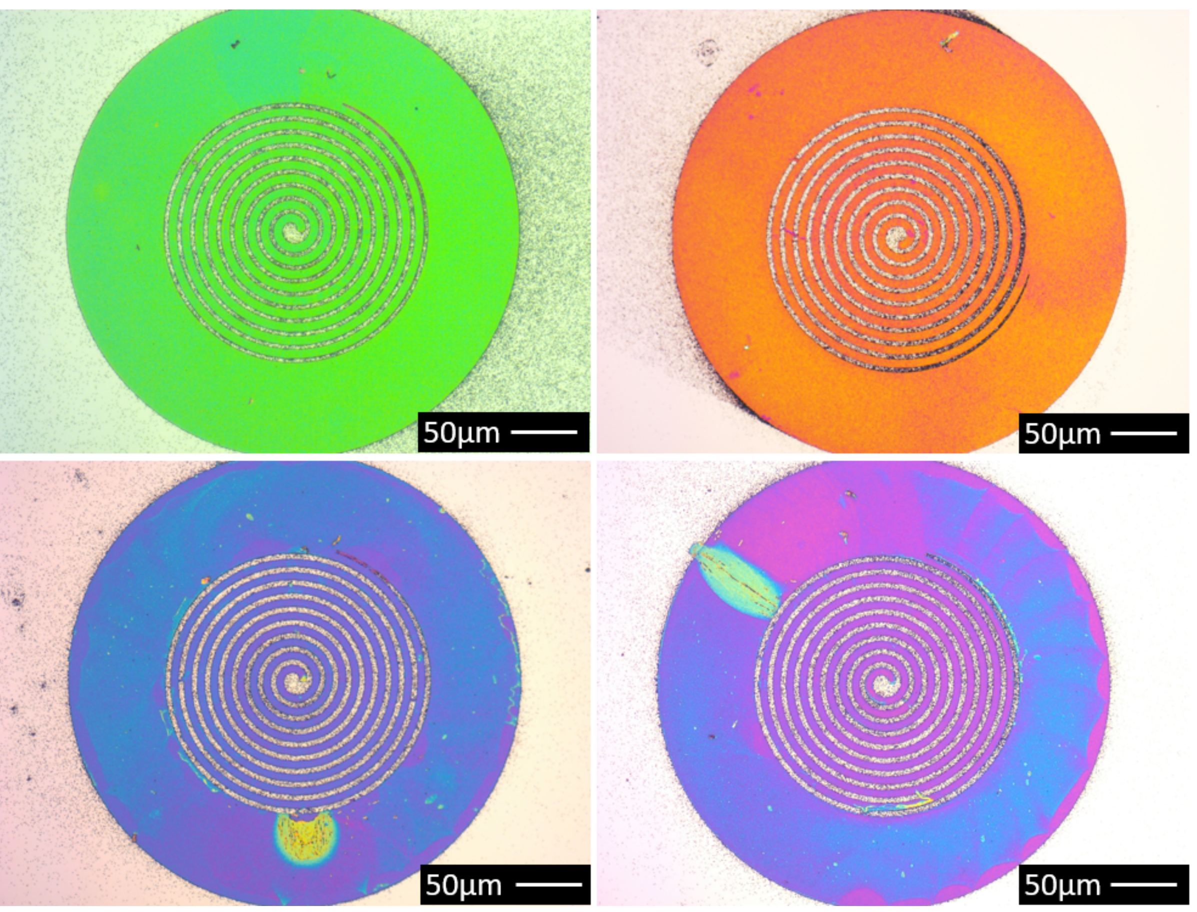

Figure G.7: Optical microscope images of 4 spiral shaped diamond structures, each grown for ~ 15 minutes under standard CVD conditions. The different colors are the result of thin film interference.

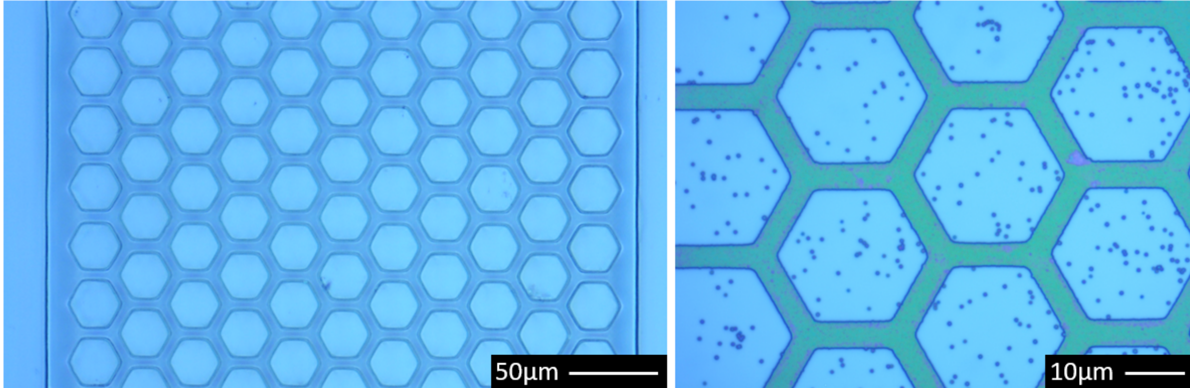

Figure G.8: Optical microscope images of a the graphene-shaped photoresist stencil (left) and a the resulting diamond structure (right) after ~ 15 minutes of CVD growth

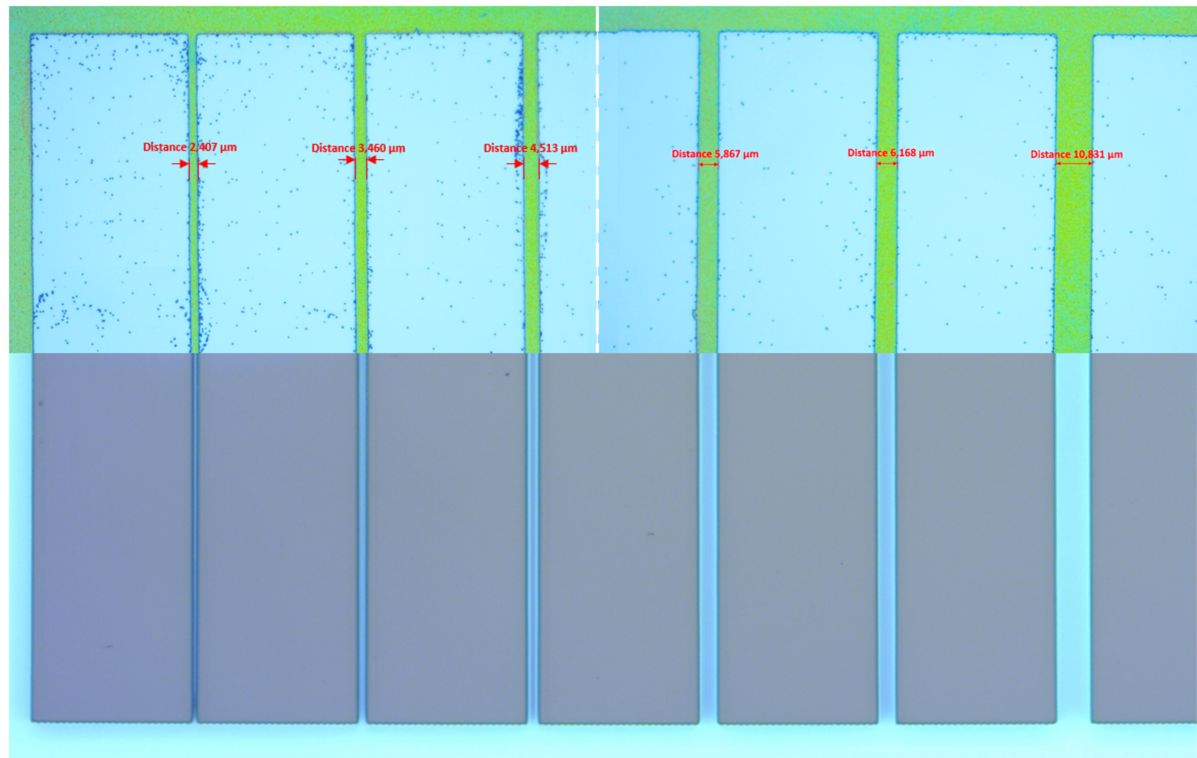

Figure G.9: Stitched optical microscope image of the thin diamond beams (green) used to evaluate the limitations of the method. The corresponding stencil is placed at the bottom for comparison. Diamond beam widths from left to right: 2.407 µm, 3.460 µm, 4.513 µm, 5.867 µm, 6.168 µm, 10.831 µm.

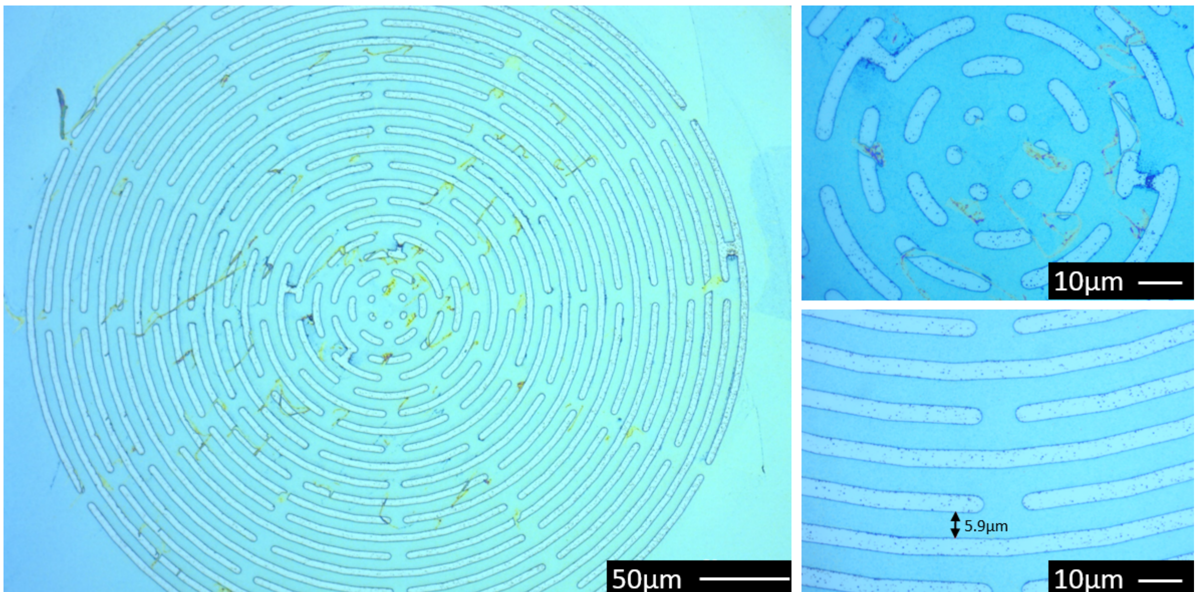

Figure G.10: Optical images of a diamond (light blue) flower-shaped structure. The yellow artifacts are presumably photoresist leftovers that turned into nucleation sites during CVD growth. Aside from few discontinuities this structure neatly matches the stencil with very little stray particles in between the diamond tracks.

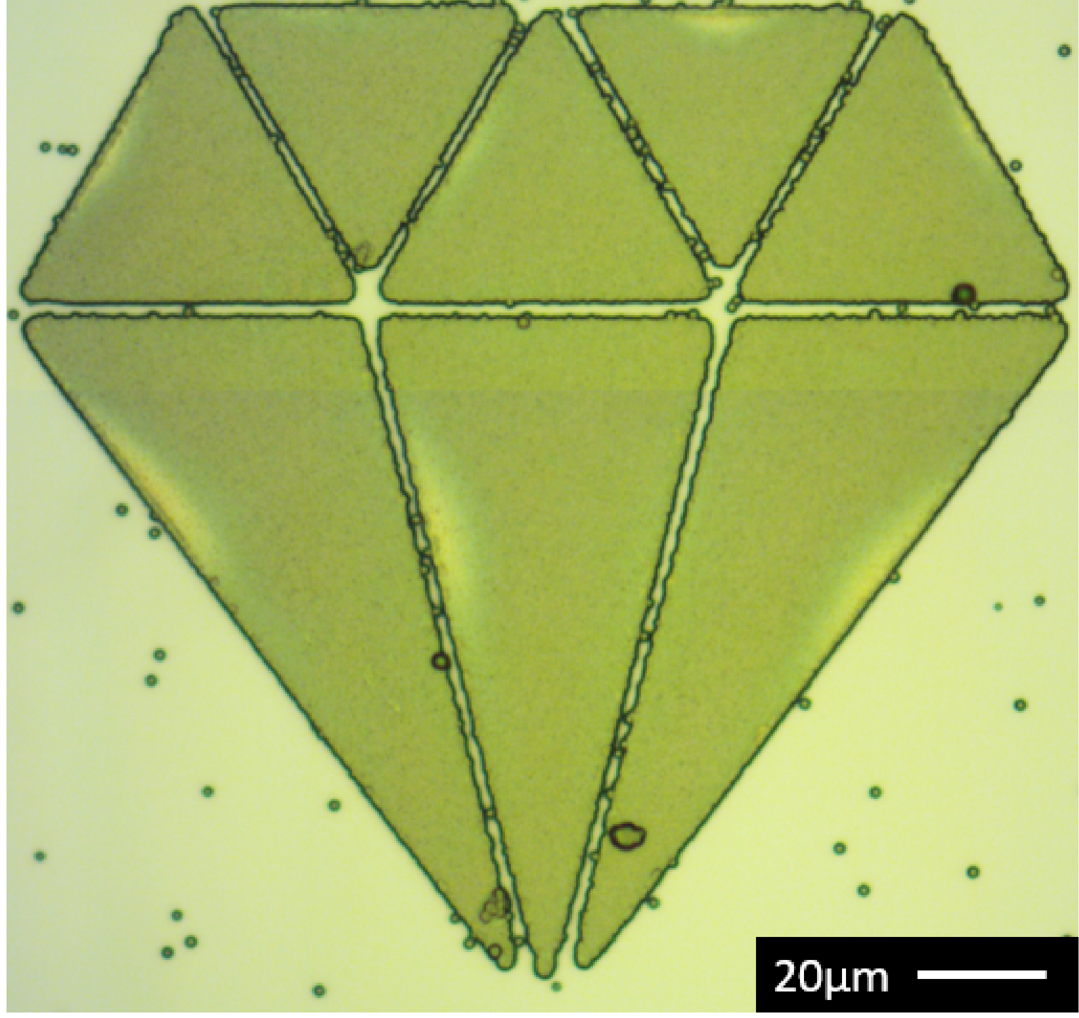

Figure G.11: Stitched optical image of a diamond-shaped diamond structure. The extended growth duration of this samples caused unseeded areas to get overgrown by lateral growth.

G.5. Suspended diamond structures

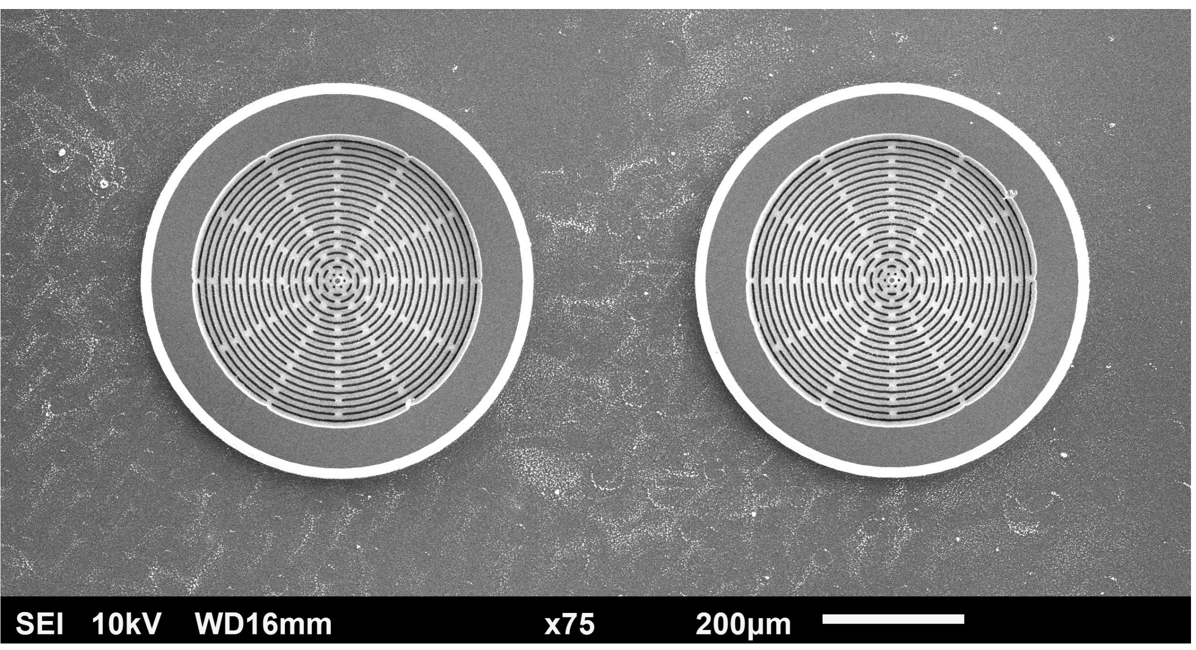

Figure G.12: Two suspended flower structures. The dark ring indicates fixation to the susbtrate.

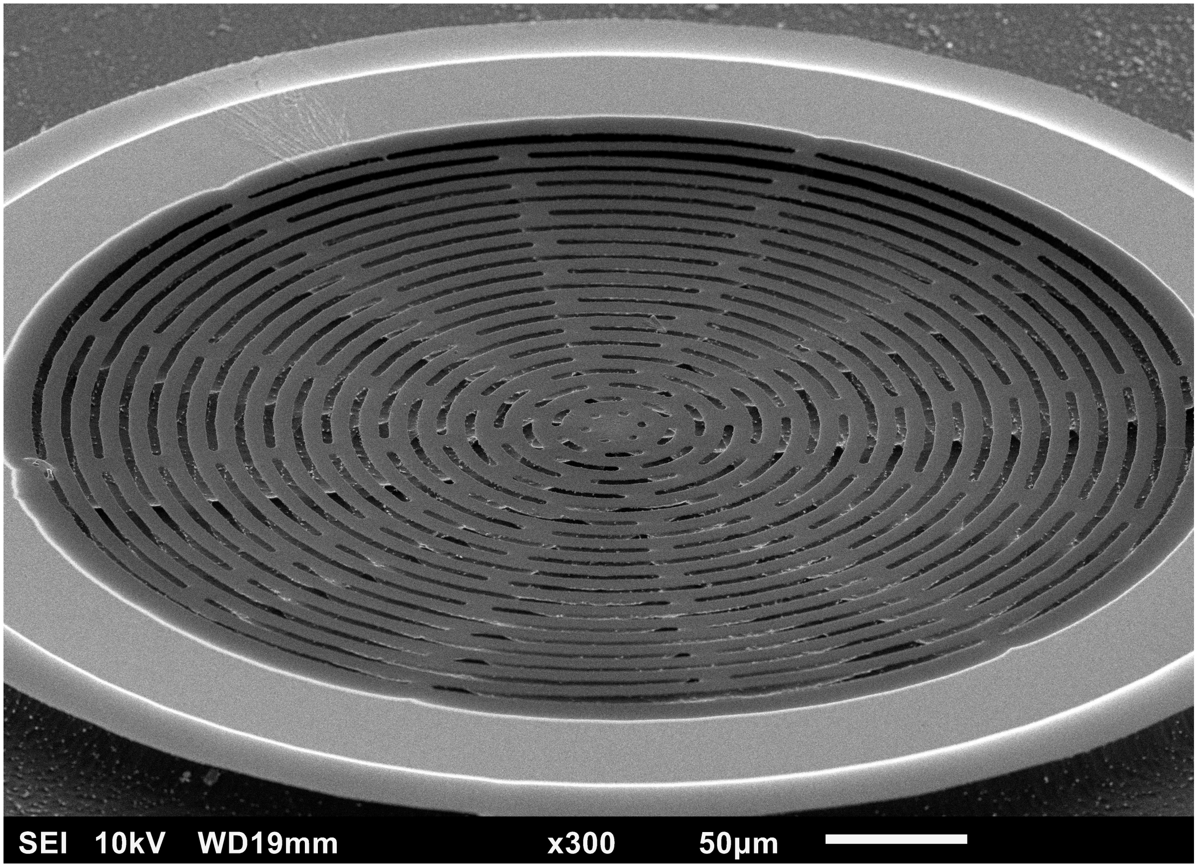

Figure G.13: SEM side view of an underetched flower structure.

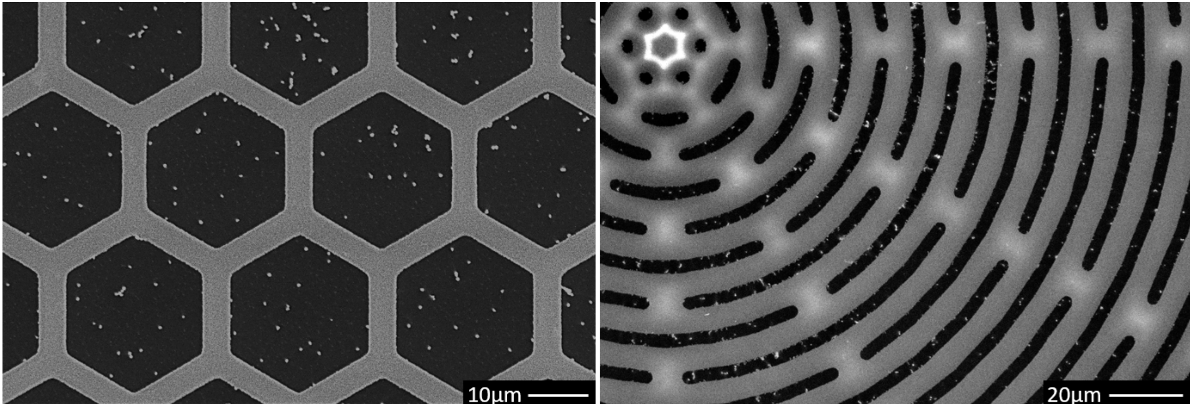

Figure G.14: SEM image showing the high definition patterns of a graphene shaped pattern and a flower pattern. The bright 'star' in top left corner, indicates is the region that is still connected to the silicon substrate.

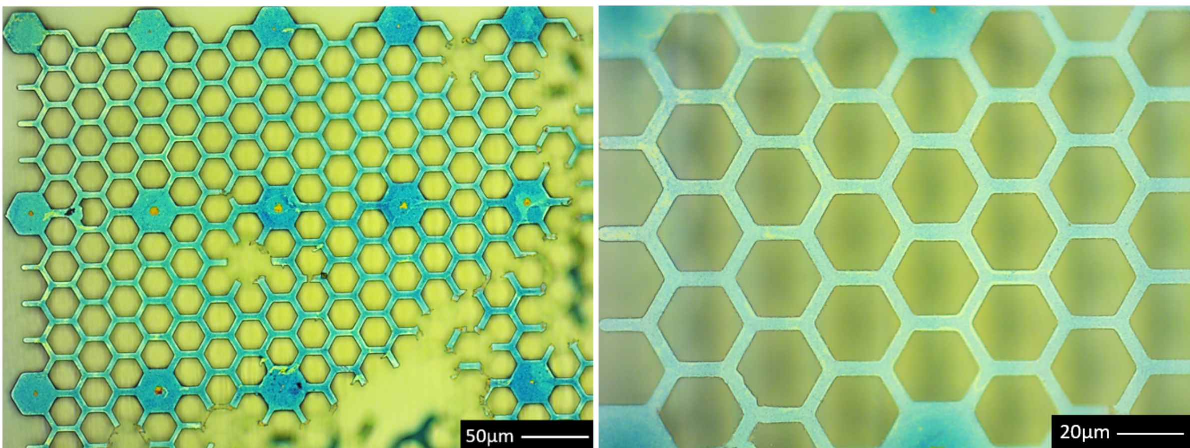

Figure G.15: Optical images of the underetched graphene shaped membrane.

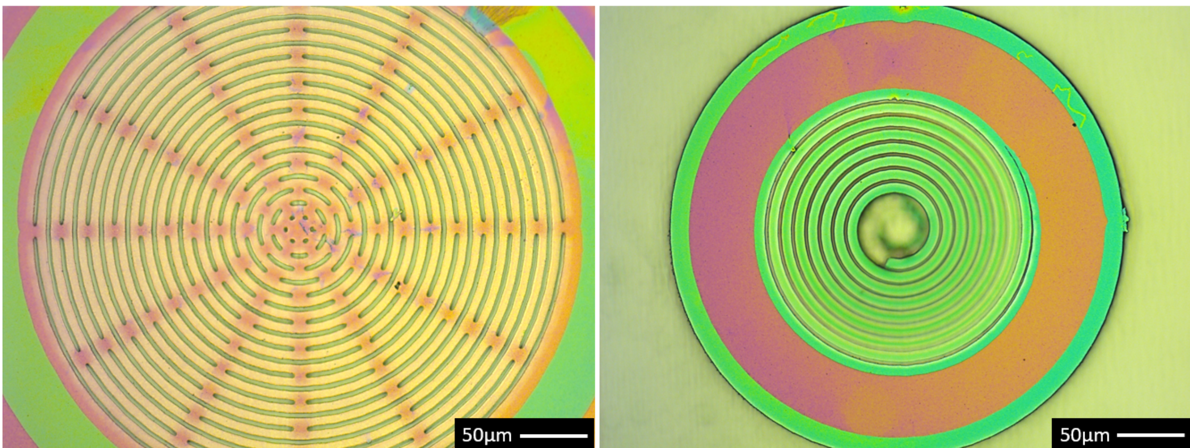

Figure G.16: Optical images of a underetched flower pattern and and underetched spiral pattern.

Bending of diamond patterns

Upward bending was observed in singly clamped micro cantilevers created in another in-house project. A hollow AFM cantilever was used to locally dispense nanodiamond dispersion on a silicon wafer prior to CVD diamond growth. These cantilevers were grown and suspended with identical methods of diamond growth and reactive ion etching. As a result of residual stresses in the film (1 µm thick), the structures bent upward as shown in Figures D.4 and D.5. Based on these results singly clamped spirals were created with the intention of creating helical structures like Figure H.1. Unfortunately, the spiral-shaped structures bend down and laid flat on the silicon substrate. In one case though, a second CVD cycle after reactive ion etching erected one of the spiral structures in a non reproducible way, see Figure H.2.

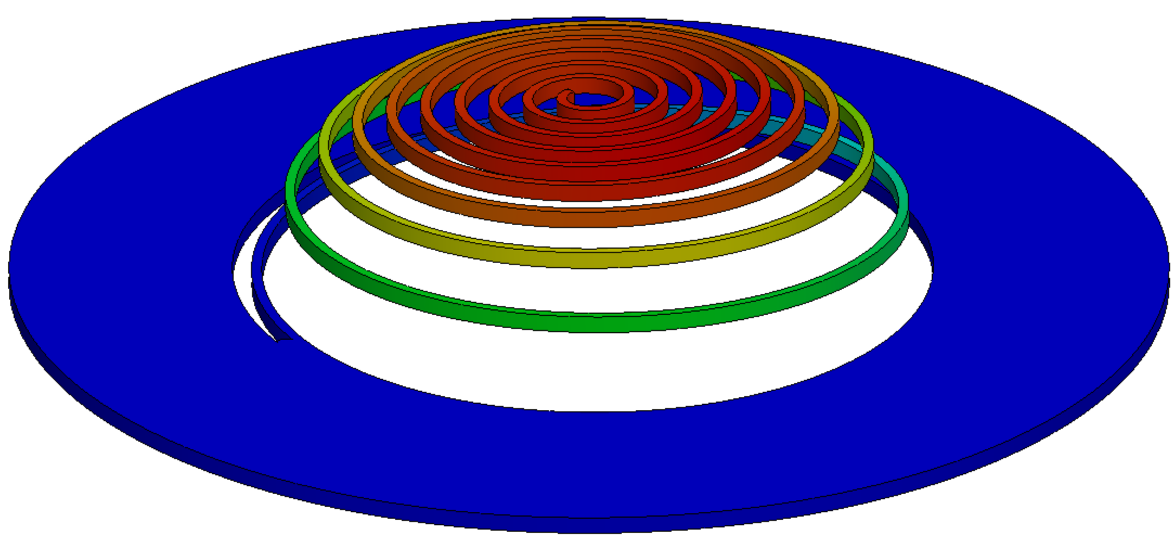

Figure H.1: SolidWorks model showing the expected shape of spirals bending upward.

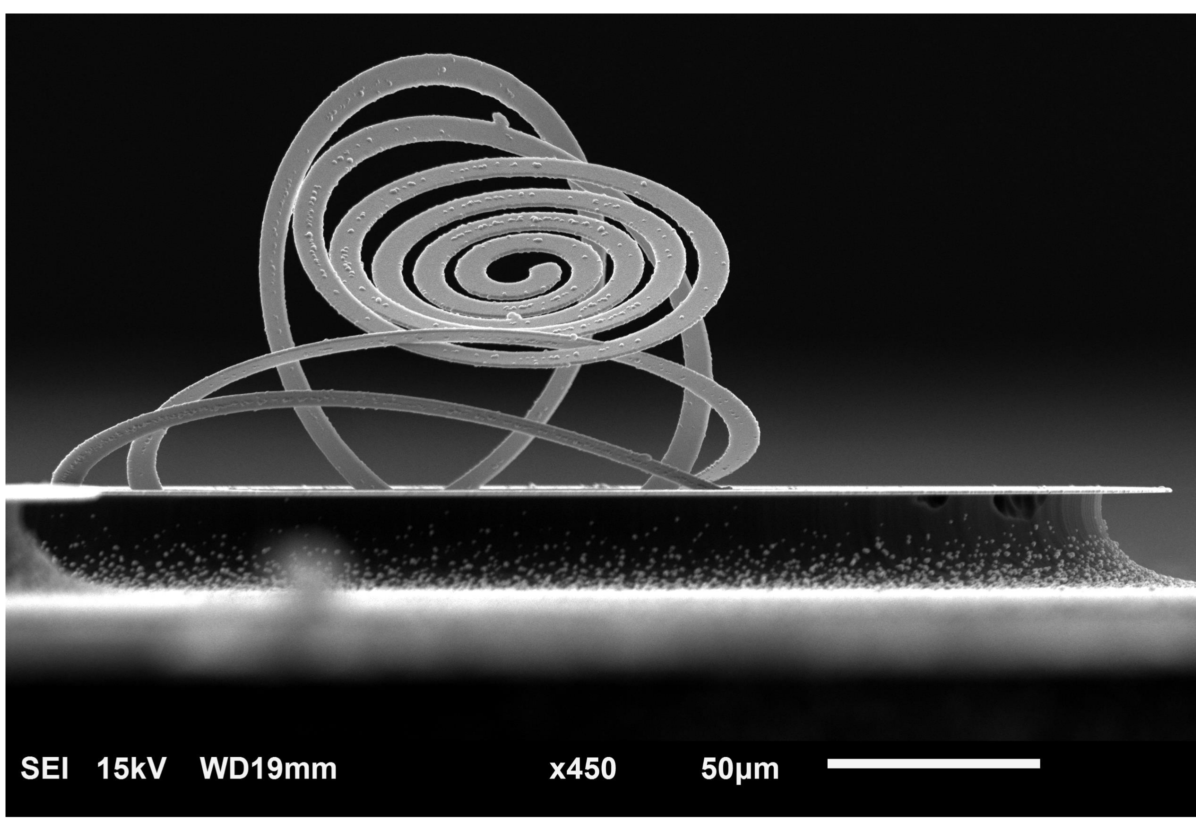

Figure H.2: SEM image showing a diamond spiral curling up after a second CVD cycle. Prior to this step the structure laid flat on the substrate.

Buckling of diamond patterns

The structures used for limit evaluation, i.e. the thin parallel beams of decreasing width, are found to buckle after reactive ion etching. From Figure I.1 it can be observed that no preference exist for up or downward buckling. Height profiles of beam 2 (up) and 3 (down) are depicted in the graphs of Figure I.2 with buckling amplitudes are 3.7 μm and 3.4 μm, respectively.

A model of the expected 3D architecture is depicted in Figure I.3 and a exaggerated 3D height profile of the actual suspended structure is shown in Figure I.4.

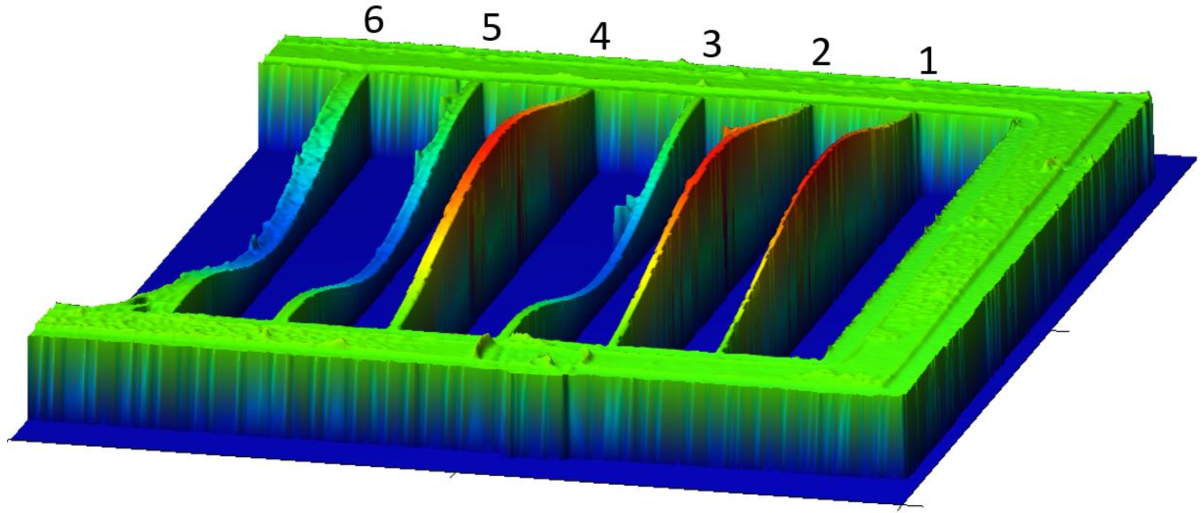

Figure I.1: 3D height profile of suspended the thin beams used for limit evaluation. The beams buckle up or down randomly.

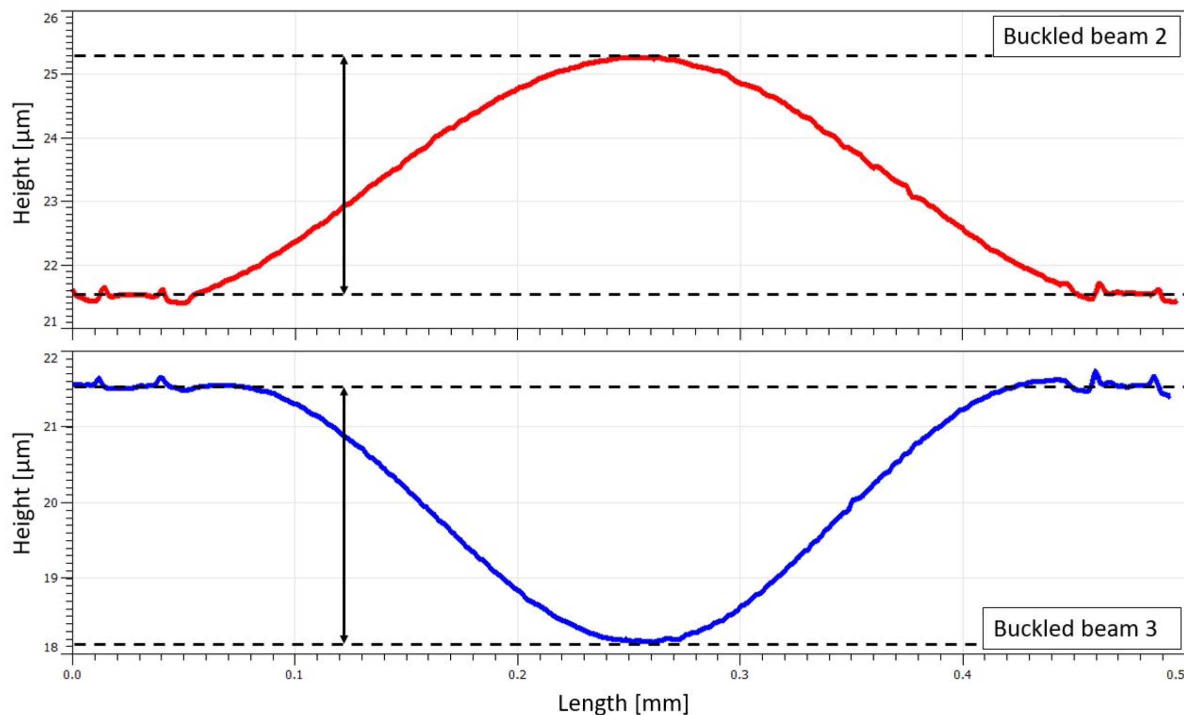

Figure I.2: Height profiles of beam 2 (red) and 3 (blue) with buckling amplitudes 3.7 µm and 3.4 µm respectively.

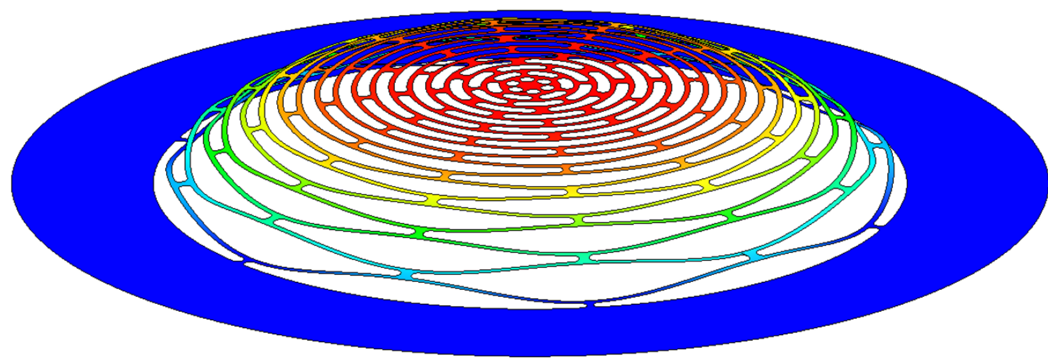

Figure I.3: A SolidWorks simulation depicting the expected 3D dome shaped structure.

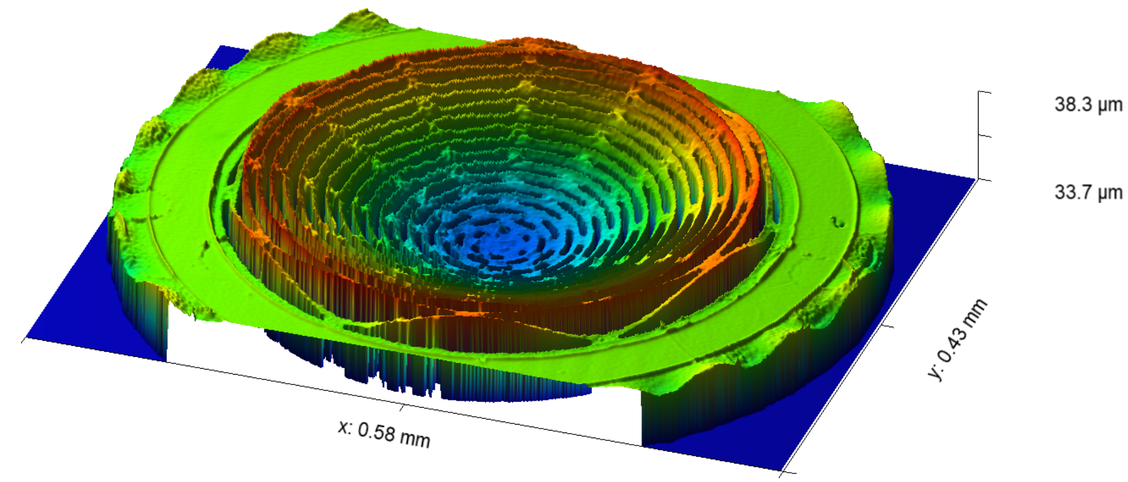

Figure I.4: Exaggerated 3D model of the actual underetched flower pattern. Buckling is observed in the beams closest to the fixed ring.

Protocol for maskless patterning of nanocrystalline diamond

Si samples Cleave silicon wafers into precise pieces of 2.4x2.4 cm. This is necessary to fit them in the Nanoscribe sample holder (2.5x2.5 cm). Clean with acetone, IPA and DI-water if dirty.

Photoresist The photoresist used is the positive tone AZ4562. Half an hour before you booked NanoScribe, get the bottle from the fridge and let it come to roomtemperature. While you are there turn on the hotplate, as it takes some time to reach its setpoint (110°C).

Spin coat Pack the inside of the spincoater with aluminum foil to prevent the tool from getting dirty. Make sure no foil is touching the rotating parts. Turn on the apparatus and apply vacuum (pump underneath fumehood + blue valve) to fix the sample. Apply photoresist to the sample using the pipettes stored in the cabinet. Select program B for a uniform layer of 10 µm, and press run. Once finished, cut the vacuum, inspect the result and place sample on top of the silicon wafer (somewhere near the hotplate) on the hotplate for 5 minutes. After 5 minutes get it out and let it rest for 5 minutes. During this time the photoresist rehydrates with water molecules from the air. This is important for adequate writing.
Once finished with the spin coater, clean inside with tissues and acetone.

Nanoscribe writing First follow Daniels training for knowledge on Describe software and the NanoScribe tool itself. Important software parameters are the slicing distance: 6 µm, the hatching distance: 1 µm, LaserPower: 80 and the ScanSpeed: 2000.
In this project the 2DML x20 objective was used. It is placed in slot 3. Use the automatic interface finder and start process. Often the tool finds an interface around pixel 400 (left form the usual 600th pixel in the centre). To fix this add 120 to the Z-offset in your code. For questions about the interface finder ask supervisor Daniel Fan. Otherwise look at previous printjobs present in userdata map.

Development While the system is writing prepare the developer solution. Fill the glass cup (equipped with white spacer, stir magnet and metallic sample holder) with 20 mL DI-water and add to that 5 mL of AZ400K. Mix thoroughly first, then reduce the rotation speed of the magnetic stirrer to the lowest setting as you put in the metallic sample holder + sample. This 4:1 ratio has proven to be optimal and erodes about 1 micron in 30 sec, thus 5 minutes are required for the 10 µm film. Depending on ambient conditions (temperature and humidity) the required time may vary a bit. Rinse with DI-water afterwards.

Seeding Create the seeding fluid by diluting the 50 mg/mL stock nanodiamond dispersion to a concentration of 2 mg/mL. Submerge the sample in the solution and knock on it with tweezers to remove air bubbles. Let it rest for 1 hour.

Flush and Lift-off After seeding, flush the sample thoroughly with DI water. Use one entire water squeeze bottle. (Applying droplets of developer solution onto the patterns helps to remove particles that possibly adhered to the photoresist.)
Place the rinsed sample on spincoater (Chemlab) and cover the inside of the spincoater with paper (as the standard plastic inset-parts will react with acetone). Find the diamond program and run. Start spray on water in the primary slow rotation stage. In the fast stage spray on acetone, IPA and DI water (in that order). A clean sample without photoresist should be the result. Spin dry or blow dry the sample and store it in a petridish. Seeded patterns will not be visible by the naked eye.

CVD growth Place the clean seeded samples in the HFCVD reactor and follow the standard CVD procedure explained during training. Make sure to keep the power ($P=V \cdot I$) around ~400 Watt. Start with standard 18.2 A current and adjust if required.

Bibliography

[1] M. Panizza and G. Cerisola, *Application of diamond electrodes to electrochemical processes,* Electrochimica Acta **51**, 191 (2005).

[2] I. Aharonovich, A. D. Greentree, and S. Prawer, *Diamond photonics,* Nature Photonics **5**, 397 (2011).

[3] C. J. Wort and R. S. Balmer, *Diamond as an electronic material,* Materials Today **11**, 22 (2008).

[4] C. E. Nebel, B. Rezek, D. Shin, H. Uetsuka, and N. Yang, *Diamond for bio-sensor applications,* Journal of Physics D: Applied Physics **40**, 6443 (2007).

[5] X. Chen and W. Zhang, *Diamond nanostructures for drug delivery, bioimaging, and biosensing,* Chemical Society Reviews **46**, 734 (2017).

[6] P. Rath, S. Ummethala, C. Nebel, and W. H. Pernice, *Diamond as a material for monolithically integrated optical and optomechanical devices,* Physica status solidi (a) **212**, 2385 (2015).

[7] Y. Tao, J. M. Boss, B. Moores, and C. L. Degen, *Single-crystal diamond nanomechanical resonators with quality factors exceeding one million,* Nature communications **5**, 3638 (2014).

[8] J. Luo, Y. Q. Fu, H. Le, J. A. Williams, S. Spearing, and W. Milne, *Diamond and diamond-like carbon mems,* Journal of Micromechanics and Microengineering **17**, S147 (2007).

[9] O. A. Williams, *Nanocrystalline diamond,* Diamond and Related Materials **20**, 621 (2011).

[10] A. Stanishevsky, *Patterning of diamond and amorphous carbon films using focused ion beams,* Thin Solid Films **398**, 560 (2001).

[11] M. P. Hiscocks, C. J. Kaalund, F. Ladouceur, S. T. Huntington, B. C. Gibson, S. Trpkovski, D. Simpson, E. Ampem-Lassen, S. Prawer, and J. E. Butler, *Reactive ion etching of waveguide structures in diamond,* Diamond and related materials **17**, 1831 (2008).

[12] H. Gamo, K. Shimada, M. Nishitani-Gamo, and T. Ando, *Ultrafine patterning of nanocrystalline diamond films grown by microwave plasma-assisted chemical vapor deposition,* Japanese Journal of Applied Physics **46**, 6267 (2007).

[13] A. F. Sartori, P. Belardinelli, R. J. Dolleman, P. G. Steeneken, M. K. Ghatkesar, and J. G. Buijnsters, *Inkjet-printed high-q nanocrystalline diamond resonators,* Small **15**, 1803774 (2019).

[14] Y.-C. Chen, Y. Tzeng, A.-J. Cheng, R. Dean, M. Park, and B. M. Wilamowski, *Inkjet printing of nanodiamond suspensions in ethylene glycol for cvd growth of patterned diamond structures and practical applications,* Diamond and Related Materials **18**, 146 (2009).

[15] H. Zhuang, B. Song, T. Staedler, and X. Jiang, *Microcontact printing of monodiamond nanoparticles: an effective route to patterned diamond structure fabrication,* Langmuir **27**, 11981 (2011).

[16] O. Loh, R. Lam, M. Chen, N. Moldovan, H. Huang, D. Ho, and H. D. Espinosa, *Nanofountain-probe-based high-resolution patterning and single-cell injection of functionalized nanodiamonds,* Small **5**, 1667 (2009).

[17] A. C. Taylor, R. Edgington, and R. B. Jackman, *Patterning of nanodiamond tracks and nanocrystalline diamond films using a micropipette for additive direct-write processing,* ACS applied materials & interfaces **7**, 6490 (2015).

[18] S.-K. Lee, J.-H. Kim, M.-G. Jeong, M.-J. Song, and D.-S. Lim, *Direct deposition of patterned nanocrystalline cvd diamond using an electrostatic self-assembly method with nanodiamond particles,* Nanotechnology **21**, 505302 (2010).

[19] V. V. Okhotnikov, S. A. Linnik, A. Gaidaichuk, D. Shashev, G. Y. Nazarova, and V. Yurchenko, *Selective deposition of polycrystalline diamond films using photolithography with addition of nanodiamonds as nucleation centers,* IOP Conference Series: Materials Science and Engineering **116**, 012001 (2016).

[20] O. Shimoni, J. Cervenka, T. J. Karle, K. Fox, B. C. Gibson, S. Tomljenovic-Hanic, A. D. Greentree, and S. Prawer, *Development of a templated approach to fabricate diamond patterns on various substrates,* ACS applied materials & interfaces **6**, 8894 (2014).

[21] F. Versluis, *2d and 3d bottom-up manufacturing of diamond micro components and devices,* Literature survey (2019).

[22] A. Gaidarzhy, M. Imboden, P. Mohanty, J. Rankin, and B. W. Sheldon, *High quality factor gigahertz frequencies in nanomechanical diamond resonators,* Applied Physics Letters **91**, 203503 (2007).

[23] J. W. Baldwin, M. K. Zalalutdinov, T. Feygelson, B. B. Pate, J. E. Butler, and B. H. Houston, *Nanocrystalline diamond resonator array for rf signal processing,* Diamond and related materials **15**, 2061 (2006).

[24] L. Sekaric, J. Parpia, H. Craighead, T. Feygelson, B. Houston, and J. Butler, *Nanomechanical resonant structures in nanocrystalline diamond,* Applied Physics Letters **81**, 4455 (2002).

[25] F. H. Guillén, K. Janischowsky, J. Kusterer, W. Ebert, and E. Kohn, *Mechanical characterization and stress engineering of nanocrystalline diamonds films for mems applications,* Diamond and Related Materials **14**, 411 (2005).

[26] G. Huang and Y. Mei, *Assembly and self-assembly of nanomembrane materials—from 2d to 3d,* Small **14**, 1703665 (2018).

[27] Z. Yan, M. Han, Y. Yang, K. Nan, H. Luan, Y. Luo, Y. Zhang, Y. Huang, and J. A. Rogers, *Deterministic assembly of 3d mesostructures in advanced materials via compressive buckling: A short review of recent progress,* Extreme Mechanics Letters **11**, 96 (2017).

[28] J. Rogers, Y. Huang, O. G. Schmidt, and D. H. Gracias, *Origami mems and nems,* Mrs Bulletin **41**, 123 (2016).

[29] S. Xu, Z. Yan, K.-I. Jang, W. Huang, H. Fu, J. Kim, Z. Wei, M. Flavin, J. McCracken, R. Wang, *et al.*, *Assembly of micro/nanomaterials into complex, three-dimensional architectures by compressive buckling,* Science **347**, 154 (2015).

[30] Z. Tian, L. Zhang, Y. Fang, B. Xu, S. Tang, N. Hu, Z. An, Z. Chen, and Y. Mei, *Deterministic self-rolling of ultrathin nanocrystalline diamond nanomembranes for 3d tubular/helical architecture,* Advanced Materials **29**, 1604572 (2017).

[31] R. van Oorschot, H. H. P. Garza, R. J. Derks, U. Staufer, and M. K. Ghatkesar, *A microfluidic afm cantilever based dispensing and aspiration platform,* EPJ Techniques and Instrumentation **2**, 4 (2015).

[32] M. K. Ghatkesar, H. H. P. Garza, F. Heuck, and U. Staufer, *Scanning probe microscope-based fluid dispensing,* Micromachines **5**, 954 (2014).

[33] S. Stehlik, M. Varga, P. Stenclova, L. Ondic, M. Ledinsky, J. Pangrac, O. Vanek, J. Lipov, A. Kromka, and B. Rezek, *Ultrathin nanocrystalline diamond films with silicon vacancy color centers via seeding by 2 nm detonation nanodiamonds,* ACS applied materials & interfaces **9**, 38842 (2017).

[34] N. G. Tsierkezos and I. E. Molinou, *Thermodynamic properties of water+ ethylene glycol at 283.15, 293.15, 303.15, and 313.15 k,* Journal of Chemical & Engineering Data **43**, 989 (1998).

[35] L. Gao and T. J. McCarthy, *Contact angle hysteresis explained,* Langmuir **22**, 6234 (2006).

[36] J. G. Buijnsters, J.-P. Celis, R. W. Hendrikx, and L. Vázquez, *Metallic seed nanolayers for enhanced nucleation of nanocrystalline diamond thin films,* The Journal of Physical Chemistry C **117**, 23322 (2013).

[37] A. Ferrari and J. Robertson, *Origin of the 1150-cm-1 raman mode in nanocrystalline diamond,* Physical Review B **63**, 121405 (2001).

[38] K. B. Gavan, E. Van der Drift, W. Venstra, M. Zuiddam, and H. Van der Zant, *Effect of undercut on the resonant behaviour of silicon nitride cantilevers,* Journal of Micromechanics and Microengineering **19**, 035003 (2009).

[39] C. Koch and T. J. Rinke, *Photolithographie - Basics of Microstructuring* (MicroChemicals GmbH, 2017).

[40] O. A. Williams, J. Hees, C. Dieker, W. Jäger, L. Kirste, and C. E. Nebel, *Size-dependent reactivity of diamond nanoparticles,* ACS nano **4**, 4824 (2010).

[41] J. Hees, A. Kriele, and O. A. Williams, *Electrostatic self-assembly of diamond nanoparticles,* Chemical Physics Letters **509**, 12 (2011).

[42] T. Yoshikawa, V. Zuerbig, F. Gao, R. Hoffmann, C. E. Nebel, O. Ambacher, and V. Lebedev, *Appropriate salt concentration of nanodiamond colloids for electrostatic self-assembly seeding of monosized individual diamond nanoparticles on silicon dioxide surfaces,* Langmuir **31**, 5319 (2015).

[43] M. Tsigkourakos, T. Hantschel, S. D. Janssens, K. Haenen, and W. Vandervorst, *Spin-seeding approach for diamond growth on large area silicon-wafer substrates,* Physica status solidi (a) **209**, 1659 (2012).

[44] L.-S. Fan, R. S. Muller, W. Yun, R. T. Howe, and J. Huang, *Spiral microstructures for the measurement of average strain gradients in thin films,* in *IEEE Proceedings on Micro Electro Mechanical Systems, An Investigation of Micro Structures, Sensors, Actuators, Machines and Robots.* (IEEE, 1990) pp. 177–181.

[45] J. Singh, S. Chandra, and A. Chand, *Strain studies in lpcvd polysilicon for surface micromachined devices,* Sensors and Actuators A: Physical **77**, 133 (1999).

[46] Z. Liu, H. Du, J. Li, L. Lu, Z.-Y. Li, and N. X. Fang, *Nano-kirigami with giant optical chirality,* Science advances **4**, eaat4436 (2018).

[47] W. Nix and B. Clemens, *Crystallite coalescence: A mechanism for intrinsic tensile stresses in thin films,* Journal of Materials Research **14**, 3467 (1999).

[48] Y. Pauleau, *Determination and Generation Mechanisms of Residual Stresses in Thin Films Produced by Physical Vapor Deposition Techniques,* in *Materials Surface Processing by Directed Energy Techniques* (Elsevier, 2006) pp. 501–535.

[49] N. Woehrl, T. Hirte, O. Posth, and V. Buck, *Investigation of the coefficient of thermal expansion in nanocrystalline diamond films,* Diamond and Related Materials **18**, 224 (2009).

[50] N. D. Masters, M. P. de Boer, B. D. Jensen, M. S. Baker, and D. Koester, *Side-by-side comparison of passive mems strain test structures under residual compression,* in *Mechanical Properties of Structural Films* (ASTM International, 2001) pp. 168–200.

[51] J. Bauer, A. Schroer, R. Schwaiger, and O. Kraft, *Approaching theoretical strength in glassy carbon nanolattices,* Nature materials **15**, 438 (2016).

[52] G. Seniutinas, A. Weber, C. Padeste, I. Sakellari, M. Farsari, and C. David, *Beyond 100 nm resolution in 3d laser lithography—post processing solutions,* Microelectronic Engineering **191**, 25 (2018).